InAlGaAs/InP Light Emitting Transistors and Transistor Lasers Operating Near 1.55 µm

A Dissertation
Presented to
The Academic Faculty

by

Yong Huang

In Partial Fulfillment
of the Requirements for the Degree
Doctor of Philosophy in the
School of Electrical and Computer Engineering

Georgia Institute of Technology
December 2010

InAlGaAs/InP Light Emitting Transistors and Transistor Lasers Operating Near 1.55 µm

Approved by:

Dr. Russell D. Dupuis, Advisor
School of Electrical and Computer Engineering
Georgia Institute of Technology

Dr. Jeffrey A. Davis
School of Electrical and Computer Engineering
Georgia Institute of Technology

Dr. Shyh-Chiang Shen
School of Electrical and Computer Engineering
Georgia Institute of Technology

Dr. Zhong Lin Wang
School of Materials Science and Engineering
Georgia Institute of Technology

Dr. Oliver Brand
School of Electrical and Computer Engineering
Georgia Institute of Technology

Date Approved: October 29, 2010

To my parents, Changfang Zhou and Tonghua Huang; and
my supportive and beloved wife, Naiyu Wang

ACKNOWLEDGEMENTS

I would like to express my sincere gratitude to those who have helped make this work and dissertation possible. First, I would like to thank my advisor, Professor Russell D. Dupuis, for his guidance and for giving me the opportunity to participate in various optoelectronics research areas that are very stimulating and challenging. His devotion for work and deep and broad knowledge on semiconductors and MOCVD inspired me very much.

I would also like to thank Professors Shyh-Chiang Shen, Oliver Brand, Jeffrey A. Davis, and Zhong Lin Wang for serving on my committee. It is an honor to have such esteemed professors on my committee.

I would like to extend my heartfelt thanks to my colleagues in the AMDG group: Dr. Jianping Liu, Dr. Hee Jin Kim, Dr. Xuebing Zhang, Dr. Dongwon Yoo, Dr. Jae Limb, Dr. Seong Soo Kim, Suk Choi, Zac Lochner, Jeomoh Kim, and Mi Hee Ji for their support, their friendship, and for all the informative discussions we had together. I would especially like to thank Dr. Jae-Hyun Ryou for always providing insightful guidance and unselfish help.

I am very indebted to our collaborators Dr. Forest Dixon, Dr. Milton Feng, and Dr. Nick Holonyak at University of Illinois at Urbana-Champaign for device fabrication and technical support.

Finally, I would like thank my parents for their endless love and unconditional support. I also consider myself extremely fortunate to have a wonderful wife, Naiyu Wang, who makes my life full of love and happiness.

TABLE OF CONTENTS

LIST OF TABLES

Page

LIST OF FIGURES

Page

SUMMARY

Light emitting transistors (LETs) and transistor lasers (TLs) are newly-emerging optoelectronic devices capable of emitting spontaneous or stimulated light while performing transistor actions. In the form of a heterojunction bipolar transistor (HBT) with quantum wells (QWs) incorporated in the base region, LETs and TLs opens up many immediate and potential applications in optoelectronic integrated circuits and high-speed photonics. This dissertation describes the design, growth, and performances of long wavelength LETs and TLs based on InAlGaAs/InP material system.

First, the doping behaviors of zinc (Zn) and carbon (C) in InAlGaAs bulk layers for *p*-type doping were investigated and clarified. Zn is found to be very diffusive in semiconductor matrix and can by contained in the base region only when the doping is lower than 4×10^{18} cm^{-3} and growth engineering is employed. On the other hand, C doping shows a low diffusivity and high doping levels but the material quality of C-doped InAlGaAs layers is poor. Using both dopants, the *N*-InP/*p*-$In_{0.52}(Al_xGa_{1-x})_{0.48}As$/*N*-$In_{0.52}Al_{0.48}As$ LETs with InGaAs QWs demonstrate both light emission and current gain (β). The Zn-doped LET shows a β of 45, making it more like an HBT while the C-doped LET shows stronger light output at 1.65 μm, making it more like a light emitting diode (LED). A charge control analysis was proposed to explain the different device performances in Zn- and C-doped LETs.

A TL based on a C-doped double heterostructure (DH-TL) was designed and fabricated. The device lases at liquid nitrogen temperature with a threshold current density (J_{th}) of 2.25 kA/cm^2, emission wavelength (λ) at ~1.55 μm, and β of 0.02. The strong intervalence band absorption (IVBA) is considered as the main intrinsic optical

loss that limits the optical output and prohibits the device from lasing at room temperature. The threshold condition in long wavelength InAlGaAs/InP TLs was then theoretically and numerically investigated. It is found that room-temperature lasing of a DH-TL is achieved only when the base thickness and doping level are within a specific narrow range. However, the selectable range is significantly expanded by mean of facet coating, structure engineering, and QW design. By using a more compressively-strained or thicker QW as the active region in a separate confinement heterostructure TL (SCH-TL), it is possible to obtain a J_{th} as low as sub-100 A/cm^2.

CHAPTER 1

Introduction to Light Emitting Transistors and Transistor Lasers

1.1 Emergence of Light Emitting Transistors

In the field of semiconductor devices, compound semiconductor materials are uniquely suited for the production of fast transistors, light emitters, and detectors. The higher mobility of electrons in compound semiconductors, which are able to travel at more than twice the speed of that in silicon (Si), makes their devices such as heterojunction bipolar transistors (HBTs) and field effect transistors (FETs) capable of higher operating frequencies and improved performances. At the same time, the major binary materials, including gallium arsenide (GaAs), indium phosphide (InP), and gallium nitride (GaN), possess the direct bandgap required for high radiative recombination efficiency and high absorption coefficient. This inherent property, combined with a great flexibility of material selection that enables various desired heterostructures, makes them the ideal materials for light emitting diodes (LEDs), laser diodes (LDs), photo detectors (PDs), and solar cells (SCs). With a total market value of over $10 billion each year [1], compound semiconductors are the dominant material technology in applications such as broadband lightwave network, wireless communication, radar systems, high-speed electronics, infrared imaging, and solid state lighting.

As the compound semiconductor devices are mainly divided into these two categories, i.e., electronic devices that control the flow of electrons and optoelectronic devices that involve the interaction between electrons and photons, one question may naturally arise: is it possible to make such a device that is capable of generating both electrical and optical signals simultaneously, since the active components are made of the same materials? Only in 2004 did

the answer become positive when the research team at University of Illinois at Urbana-Champaign directly observed light emission from an InGaP/GaAs HBT and gave birth to a new type of three-port compact light source, light emitting transistors (LETs) [2]. Their patent reads: "The LET extends the capabilities of LEDs and could make this transistor the fundamental element in electronics and optoelectronics." It was almost 60 years after the invention of transistors [3] and more than 40 years after the invention of LEDs [4]. The development of LETs, which bridge the functionality gap of LEDs and HBTs, seems to be a natural evolvement within the 50-years of compound semiconductor research and exploitation.

1.2 Basic Operation Theory

Optoelectronic devices generally deal with two types of carries, negatively charged electrons and positively charged holes. In a two-terminal *pin* LED structure with forward bias, electrons are injected from the *n*-side (cathode) and holes are injected from the *p*-side (anode) into the *i*-region whereby these excess carriers undergo radiative recombination, as illustrated in Figure 1.1 (a). When quantum wells (QWs) are inserted in the active region, most carriers will be trapped by the QWs due to the quantum confinement of the heterostructures, thus giving rise to improved luminescence efficiency [5].

The operation of a three-terminal bipolar junction transistor (BJT) also involves both electrons and holes with the assist of an additional junction. In the case of an *npn* transistor in the forward active mode, electrons are injected from the emitter, swept across the base, and collected at the base-collector (BC) depletion region due to the reverse biased electrical field. During this process, some electrons recombine rapidly with holes, supported by the base current that is essential for transistor operation. Traditionally, researchers try to minimize the base

recombination current in Si-based BJTs and compound-based HBTs because it's considered as a waste current that generates unwanted heat [6]. LETs, on the contrary, utilize the radiative recombination by intentionally incorporating QW(s) in the base region of III-V based HBTs, thanks to the high radiative recombination efficiency in direct bandgap materials. As a result, we have a unique device that produces both electrical and optical signals. The operation principles for the HBT and LET are schematically illustrated in Figure 1.1 (b) and (c), respectively. The major structural difference between these two devices is the presence of QW(s) in the LET.

In the HBT, the base current normally consists of [6]:

1. Bulk recombination current;
2. Base-emitter (BE) space-charge recombination current;
3. Hole backward injection, surface recombination and base contact interface recombination current.

The bulk component can be made up of radiative recombination, Shockley-Read-Hall recombination, and Auger recombination. In the LET depicted in Figure 1.1 (c), the radiative recombination is effectively enhanced by the carrier capture and confinement of the undoped QW. Light emission is supported by the hole resupply of base current, therefore it can be modulated in phase with base current. With the HBT capable of operating at speed over 700 GHz [7], the LET owns a switching speed impossible to attain with an LED. The base QW can be regarded as an optical collector in addition to the conventional electrical collector (the BC junction) [8], both of which consume electrons in a competitive way. The enhanced radiative recombination current is a major component of the LET base current, and as a result the current gain of the transistor is reduced compared to that in the HBT [2].

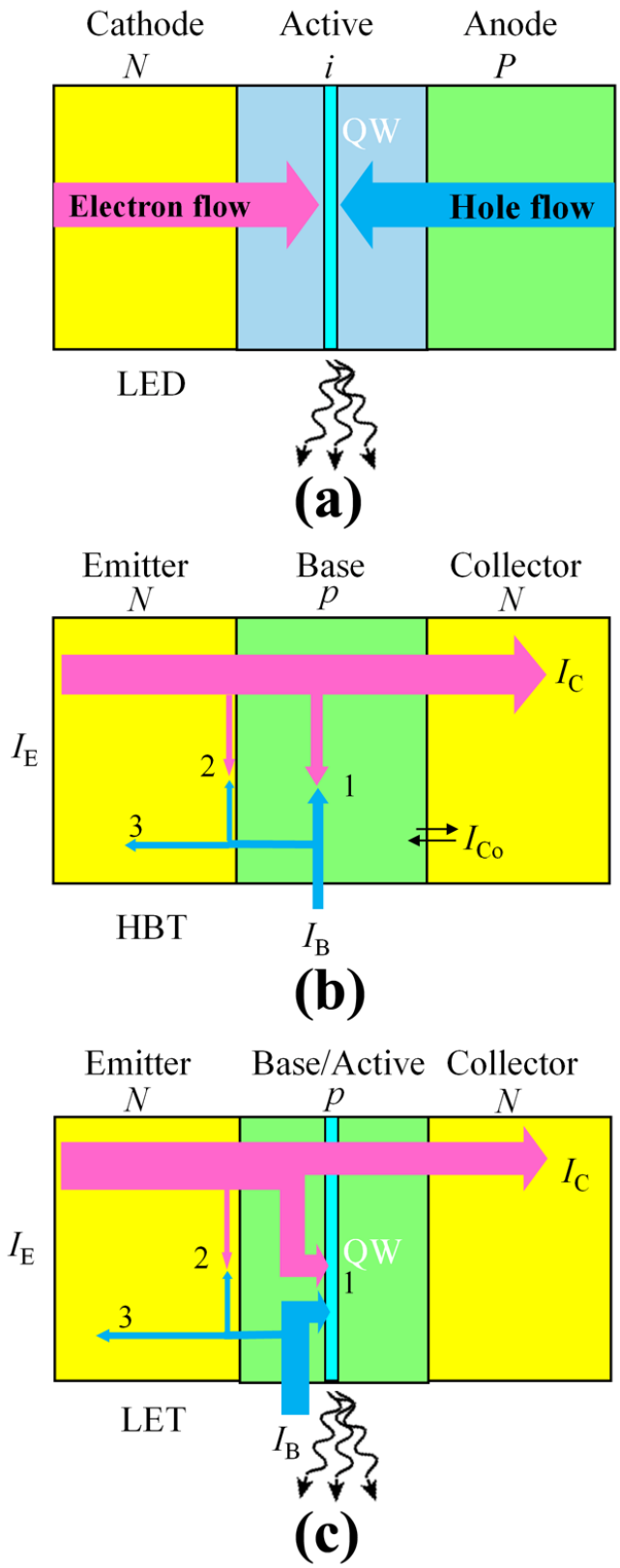

Figure 1.1: Electron and hole flows in (a) an LED, (b) an HBT and (c) an LET in active mode.

It's interesting to compare LETs with heterojunction phototransistors (HPTs), another kind of HBT-based optoelectronic device. In HPTs, current is created by light absorption in the base and collector region and amplified by the transistor action [5], while in LETs light is generated at the cost of reduced current gain of the transistor, which is opposite to HPTs' operation. With complimentary functions and a similar material structure, these two types of devices would be potentially important in optoelectronic integrated circuits (OEIC).

1.3 History and Development

The concept of making transistors emit light is not new. In 1992, Belgian researchers successfully built a resonant tunneling light emitting transistor using GaAs material system [9]. In the following year, a three-terminal light emitting heterojunction field effect transistor (HFET) was demonstrated based on real-space transfer [10]. HBT-like light emitting structures were proposed and realized as well [11,12], but the active region was in the collector area, taking advantage of the hot electron injection. There are also a number of reports addressing light emitting FETs based on organic materials [13-15]. However, none of these devices has gained as much focus and success as the LET does.

Ever since the proof-of-concept demonstration in 2004 [2], tremendous progress has been made to push up the LET performances. The first LET was a plain InGaP/GaAs HBT with light emission at 885 nm determined by the base composition. After that, InGaAs QWs were inserted into the base region and light emission was significantly enhanced [16]. The real breakthrough came later in the same year when laser operation of a GaAs-based HBT was demonstrated [17], making the LET into a transistor laser (TL). TLs were realized by providing cladding layers for optical confinement and creating optical cavity for feedback. As analogous to the LDs related to

LEDs, TLs are considered to be more fundamentally and practically important than LETs. TLs first worked at ~200 K in pulsed mode, and then at ~213 K in continuous wave (CW) mode [18], and eventually at room temperature in CW mode in 2005 [19]. Distributed feedback (DFB) TL was also demonstrated recently [20]. Now TLs have achieved a 3dB bandwidth of 13.5 GHz with direct modulation [21] and 22 GHz with an auxiliary base signal [22], and extensive related studies are still underway.

Besides the LETs and TLs based on InGaAs/GaAs system with operating wavelength at ~980 nm, researchers have demonstrated LETs in the visible spectrum region corresponding to red (λ~650 nm) and violet (λ~385 nm) colors employing InAlGaP/InGaP/GaAs and InGaN/GaN heterostructures, respectively [23,24]. Here at Georgia Institute of Technology, we develop the long wavelength (λ~1550 nm) LETs and TLs based on InAlGaAs/InP material system [25], which is main subject of this thesis.

1.4 Characteristics and Applications of LETs and TLs

LETs and TLs are unique devices to study the carrier and phonon dynamics. The most conspicuous feature is the compression of the collector current-voltage (*I-V*) characteristics or decrease in current gain during the transition from spontaneous to stimulated recombination [19]. This is quite understandable since the optical gain and current gain are strongly correlated in a TL [26]. Simply introducing scattering on the cleaved mirror surfaces of a TL will spoil the lasing condition and convert it back to an LET [27]. The collector breakdown of a TL is caused by photo-assisted tunneling, which in turn quenches the laser operation due to high optical loss [28,29]. This effect is more significant in the TL with a tunnel junction collector and enables it to be directly modulated by the BC voltage [30,31]. Another interesting characteristic of a TL is

that laser operation occurs on the ground state of the QW(s) at low bias current and switches to first excited state at high bias current, which is not commonly observed in diode lasers [21,27]. The higher density of states and optical gain at higher quantized energy are thought to account for the change of working states with increasing losses [32].

Perhaps the most important property of LETs and TLs is the reduced carrier recombination lifetime in the base region [8]. Unlike the operation of LEDs, which relies on the simultaneous injection of both electrons and holes to the active region, light emission from LETs and TLs utilizes the minority carrier recombination with the majority carrier level staying almost constant as the QW is always full of holes. Due to the tilted charge distribution, the quantum capture and radiative recombination in the QW are competing against the fast carrier transport in the base, so the effective carrier lifetime is greatly reduced [33,34]. In other words, in contrast to the charge pile-up in LEDs, carriers that are too slow to recombine within the transistor transit time are removed from the base by the BC junction reverse field, allowing for only fast recombination. The reduced carrier lifetime makes possible a record spontaneous optical bandwidth of 4.3 GHz in the LET [35,36], while the highest speed ever achieved by a traditional *p*-*i*-*n* LED has been 1.7 GHz with the active layer doped to 7×10^{19} cm^{-3} [37]. Moreover, in the case of TLs both experiments and calculation have shown a wide-band optical modulation along with the suppression of relaxation oscillation peak in the frequency response and a reduced turn-on delay [8,22,33,34,38, 39].

Equipped with these unique characteristics, LETs and TLs promise many immediate and potential applications in optoelectronic area. As a transistor, LET or TL provides an additional light signal in phase with base current, which can be used in optical integration, such as in optical transceivers, inter-chip communication, and displays. Figure 1.2 is a schematic

implementation of an optical transceiver system using LET and HPT, where light signal is generated by LET and detected by HPT.

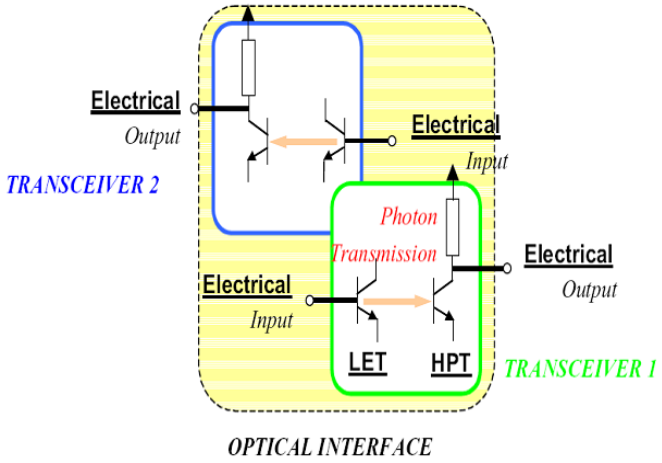

Figure 1.2: Schematic diagram of an optical transceiver system using LET and HPT.

As a light source, LETs and TLs possess a fast modulation speed and an excellent current handling capability, which could potentially replace the two terminal LEDs and LDs. The collector current density can be as high as 2 MA/cm^2 in high performance HBTs [7], whereas in the LDs this value is only around 10 kA/cm^2. The voltage control as well as the usual current control enables the TL to become a signal mixer [31,40]. In addition, thanks to the dual functionality of TL as a conventional HBT and a laser source [27], the complexity associated with monolithic integration of an HBT and a TL is significantly reduced compared to the integration of an HBT with an LD in term of structure design, material growth, and device fabrication. Figure 1.3 (a) illustrates the conventional way of integration, where both LD and HBT structures are grown in the vertical direction and the LD is made after etching the HBT material away [41]. In contrast, the integration of an HBT and a TL is much simpler in that they share the same materials, as shown in Figure 1.3 (b). As still in the material and device level of

the research, LETs and TLs require more focus from systems engineers and circuit designers to exploit their novel functionalities and integrate them into current systems.

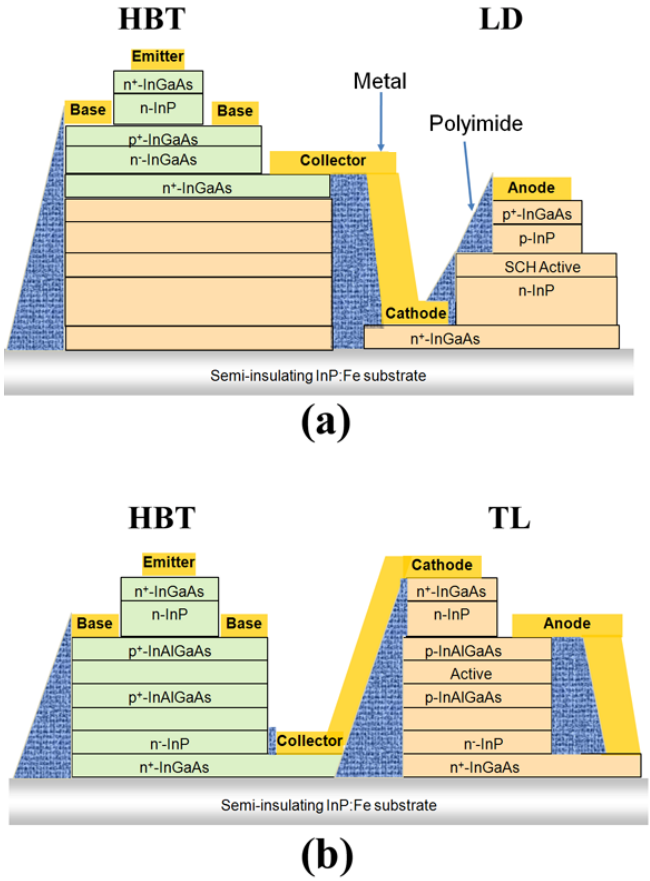

Figure 1.3: Monolithical integration of (a) HBT and LD and (b) HBT and TL.

1.5 Motivation and Challenges of Long Wavelength LETs and TLs

The TLs demonstrated to date have primarily been based on AlGaAs/GaAs with strained InGaAs QW structures, and the emission wavelength of this material system is therefore limited to the near-infrared region (λ~980 nm). For fiber optical communication applications, the TL operating wavelength should be extended to either ~1.3 μm or ~1.55 μm and high-speed direct modulation of TLs can be a critical benefit at those wavelengths. InP material system has been the dominant material technology in producing LDs at these wavelengths as well as in making

high-performance HBTs and thus becomes the best candidate for long wavelength TLs. It also takes advantage of potential optoelectronic integration with InP/InGaAs HBTs or InGaAs/InAlGaAs/InP detectors and modulators for high-speed applications. However, successful transfer of the TL technology from GaAs to InP is nontrivial. First, compared to the GaAs based structures, the material gain and model gain are relatively low in InP material system. The calculated optical gain for the strained InGaAs on GaAs is almost twice as large as that for InGaAs on InP [5]. The material selection is also limited for InP family. $Al_xGa_{1-x}As$ ternary is nearly lattice-matched to GaAs throughout the entire composition range and lattice-matched $In_{0.51}(Al_xGa_{1-x})_{0.49}P$/GaAs heterostructure also plays an important role, whereas $In_{0.52}(Al_xGa_{1-x})_{0.48}As$ seems to be the only viable option for InP. In addition, the presence of strong intervalence band absorption (IVBA) in *p*-type base at long wavelengths brings about significant loss to the system and may prohibit the device from lasing [42,43]. Finally, *p*-type doping in the base poses unique challenges. The commonly-used *p*-type dopant, zinc (Zn), is very diffusive in the semiconductor matrix and can't be easily controlled [44]; on the other hand, another widely-used dopant, carbon (C), has proved to be less efficient and C doping suffers from inferior material qualities and poor growth reproducibility [45]. To tackle these issues, knowledge on InP-based HBTs and LDs should be brought together with respect to the device design, growth schemes, doping conditions, and device fabrication.

Compared to another lattice-matched InGaAsP material system, InAlGaAs materials offer large conduction band offset (ΔE_c) and easy material growth and have been widely employed in the uncooled DFB LDs for fiber communication [5]. The bandgaps of the lattice-matched $(In_{0.53}Ga_{0.47}As)_{1-x}(In_{0.52}Al_{0.47}As)_x$ or $In_{\sim 0.52}(Al_xGa_{1-x})_{\sim 0.48}As$ quaternary spans from 0.75 eV for

$In_{0.53}Ga_{0.47}As$ to 1.5 eV for $In_{0.52}Al_{0.47}As$. The bandgap energy (E_g) on the relative Al composition x can be expressed as [46]:

$$E_g = 0.75(1-x) + 1.5x - 0.1x(1-x). \quad (1.1)$$

The conduction band and valence band offsets of $In_{0.53}Ga_{0.47}As$ and $In_{0.52}Al_{0.47}As$ with respect to InP are illustrated in Figure 1.4. With the increase of Al composition, the band alignment changes from straddling lineup in InGaAs/InP to staggered lineup in InAlAs/InP, which can be exploited in bandgap engineering in novel devices. The dependence of ΔE_c on x is given by [47]:

$$\Delta E_c = 0.245 - 0.566x + 0.069x^2. \quad (1.2)$$

The electron effective mass (m*) on x is described by [48]:

$$\frac{m^*}{m_0} = 0.043 + 0.046x - 0.017x^2, \quad (1.3)$$

where m_0 is the electron rest mass. The refractive index at 1.55 μm in InAlGaAs is given as [49]:

$$n = 3.6 - 0.51x + 0.12x^2. \quad (1.4)$$

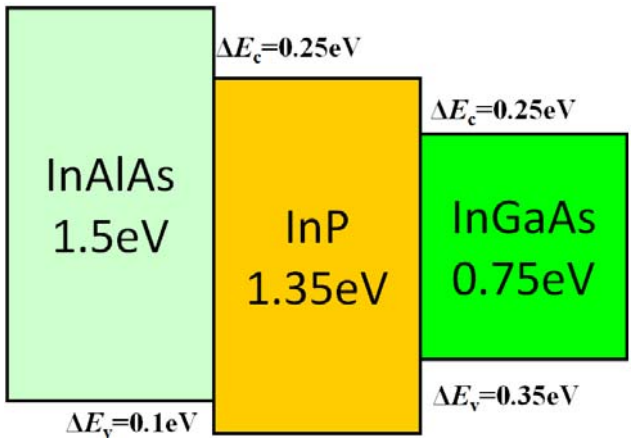

Figure 1.4: Band alignment of InGaAs/InP and InAlAs/InP.

1.6 Scope of this Dissertation

This work describes the design, growth, and characterization of long-wavelength InAlGaAs/InP LETs and TLs. The device structures have been grown by metalorganic chemical vapor deposition (MOCVD), which is the preferred growth technique in manufacturing in terms of productivity, over-all cost, uniformity, and throughput. Of primary interest is the correlation between material properties and device performances via the exploration and understanding the device physics. The research background of LETs and TLs, operation principles of relevant devices, motivations for long-wavelength LETs and TLs, and material properties of InAlGaAs alloys have been addressed in this chapter. In Chapter 2, MOCVD growth technique and material characterization methods will be examined in detail. Chapter 3 covers the investigation of LETs and TLs with Zn-doped base layers. Chapter 4 presents the growth and performances of LETs and TLs with C-doped base layers. In Chapter 5, attempts to achieve *p*-type materials with novel methods such as atomic layer epitaxy and strained superlattices will be discussed. Chapter 6 is devoted to the theoretical investigation and numerical evaluation of TL structures, which gives the guideline for designing a long wavelength TL. Finally, Chapter 7 summarizes the results of this work and contemplates future directions of these studies.

CHAPTER 2

Material Growth and Characterization Techniques

2.1 Metalorganic Chemical Vapor Deposition

Metalorganic chemical vapor deposition (MOCVD) is an epitaxial growth method for semiconductor crystals, especially for compound semiconductors. It is a non-equilibrium vapor-phase process where the metal precursors used are metalorganics such as trimethylindium (TMIn) or trimethylgallium (TMGa). The capability of MOCVD of growing device-quality material was first demonstrated by Manasevit in 1968 [50] and developed by Dupuis in 1977 [51]. Due to its versatility, MOCVD is the most popular method employed in industry for the growth of III-V materials worldwide.

2.1.1 MOCVD Reactor

In MOCVD, two or more sources in a gaseous form are introduced into a reaction chamber where they chemically react with one another to form a solid material on a heated substrate. Figure 2.1 shows the schematic representation of a MOCVD system. The MO sources (including group III and some dopant precursors) exist in either liquid or solid form and are stored in an all welded stainless steel containers, commonly referred to as "bubblers". A carrier gas (usually hydrogen, H_2) passes through the containers and transports the MO precursor molecules into the growth chamber. The group V precursors, on the other hand, are generally hydrides such arsine (AsH_3) and phosphine (PH_3) and are kept in high-pressure gas cylinders. The gas handling and switching system consists of computer-controlled mass flow controllers

(MFCs), pressure controllers (PCs), and pneumatic valves. The delivery of hydride and MO sources are separated to avoid pre-reactions.

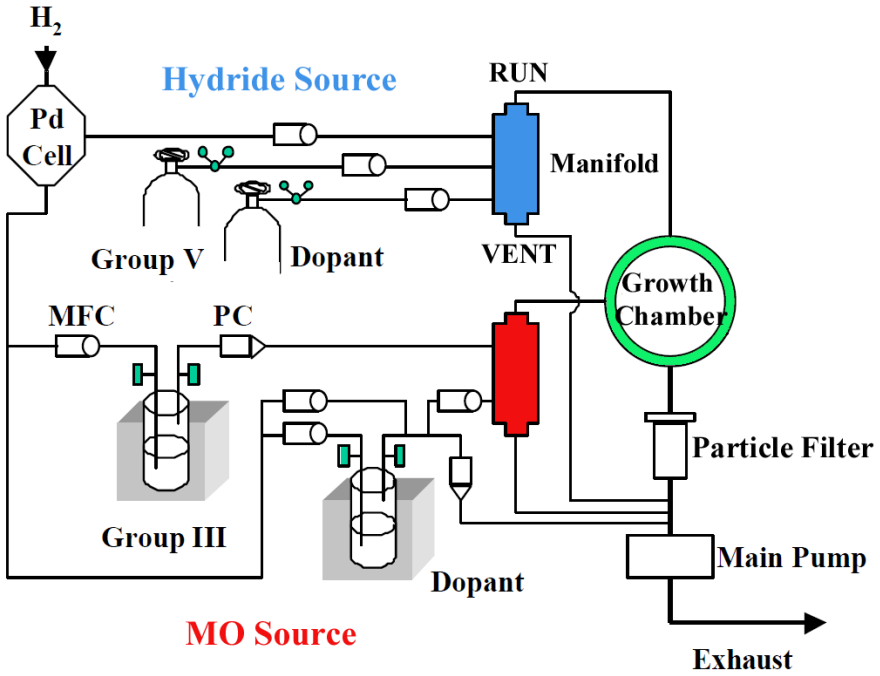

Figure 2.1: Schematic diagram of a MOCVD system.

All the gases are directed into the stainless steel reactor chamber from its top flange. Inside the chamber, there is a flow showerhead through which the MO and hydride sources are introduced, a high-speed rotating susceptor for achieving a uniform boundary layer above the substrate, a heater system which gives thermal energy to the substrate and sources for pyrolysis reaction, and a thermocouple for temperature control.

The unreacted precursors and reaction by-products are delivered to the scrubber for waste treatment through the exhaust system. The main function of the exhaust system is to maintain a specific pressure of the reactor chamber using a vacuum pump. Precise control of the growth pressure is one of the key factors to obtain reproducible high-quality and uniform epitaxial layers in MOCVD.

2.1.2 MOCVD Growth Process

The MOCVD growth process can be divided into four processes, i.e., gas input, pyrolysis, diffusion, and surface reaction. Figure 2.2 shows the schematic illustration of GaAs epitaxial growth using TMGa and AsH_3 [52]. The basic chemical reaction that occurs on the heated GaAs substrate can be described by the following:

$$(CH_3)_3Ga + AsH_3 \rightarrow GaAs + 3CH_4$$

This reaction deposits solid GaAs on the substrate and the volatile by-product CH_4 along with carrier gases is swept away by the pump. The quality of the epitaxial layers strongly depends on the choice of growth temperature, growth rate, V/III ratio, and reactor pressure.

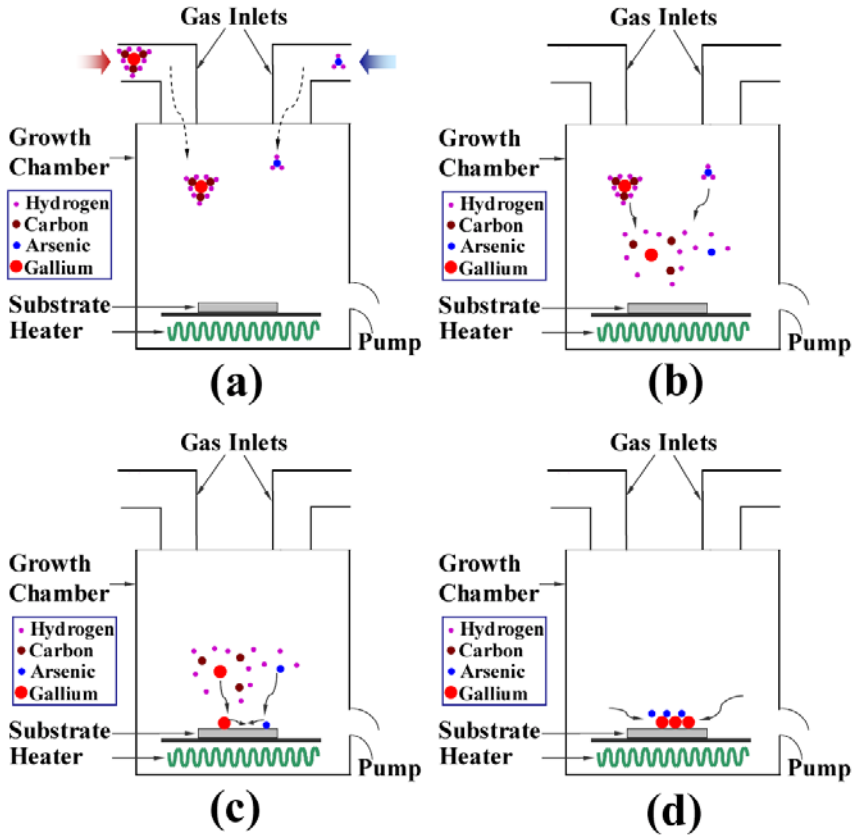

Figure 2.2: Schematic illustration of MOCVD epitaxial growth process: (a) gas input (b) pyrolysis (c) diffusion (d) surface reaction.

2.2 Material Characterization Techniques

The study on semiconductor materials requires various kinds of characterization techniques for proper understanding of the material properties and their relations to device performances. Thus, the application of a desired structural, optical and electrical characterization to each necessary step is critical. The primary characterization tools employed in this work will be described.

2.2.1 X-ray Diffraction

X-ray diffraction (XRD) is a powerful, fundamental and nondestructive characterization technique for semiconductor materials, from which lattice constant, residual strain, alloy composition, film thickness, etc. can be determined. As semiconductor devices typically consist of multiple layers with various thickness and strain state, XRD is a routine characterization method in semiconductor growth.

Diffraction is a phenomenon that occurs when electromagnetic wave interacts with a periodic structure whose repeat distance is about the same as the wavelength of the wave. In-phase waves cause constructive interference and out-of-phase waves are cancelled out each other in their superimposed wave. Since the semiconductor crystal has a periodic atomic arrangement, when X-ray with a wavelength that is comparable to the periodic spacing of the crystal planes is applied, the crystal structure can be revealed from the diffraction pattern that is obtained by detecting the scattered X-ray from the sample.

The condition of constructive interference by different crystallographic planes in a crystal is given by Bragg's law:

$$2d_{hkl}\sin\theta_{\mathrm{B}} = n\lambda \tag{2.1}$$

where d_{hkl} is the spacing between adjacent crystallographic planes, θ_B is Bragg's angle between the lattice plane and incident X-ray, n is the order of the diffraction, and λ is the wavelength of X-ray, typically 1.5405Å from Cu $K_{\alpha 1}$. The principle in Bragg' law is schematically illustrated in Figure 2.3.

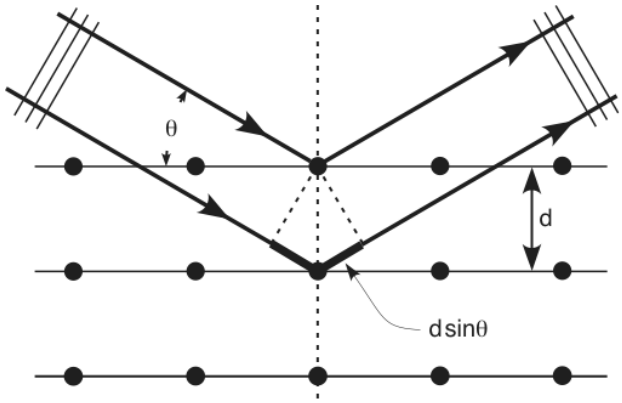

Figure 2.3: Schematic illustration of Bragg's diffraction condition.

For a cubic crystal, the spacing d_{hkl} is given by:

$$d_{hkl} = \frac{a}{\sqrt{h^2+k^2+l^2}}, \tag{2.2}$$

where a is the lattice constant of interested layer and (h k l) is the Miller indices of the crystallographic plane. The usual way to determine θ_B in XRD is ω-2θ scan. In this diffraction configuration, the detector (2θ) moves at twice the angular rotation rate of the sample (ω) so that the measured diffraction angle remains equal to the incident beam angle. From the measured θ_B, we can determine the lattice constant form Equation 2.1 and 2.2 and subsequently derive the information on composition and strain state of the interested layer. When the epitaxial layer has abrupt interfaces, it shows interference patterns known as Pendellösung fringe [53], which is a good indicator of material quality and layer thickness. For complicated multi-layer structures, the composition and thickness of each layer can be modeled using an X-ray simulation program.

The diffraction pattern from XRD is basically a measurement of the reciprocal lattice point (RLP) of crystallographic planes. Furthermore, a two-dimensional mapping of the reciprocal space (RSM) can be generated through a set of ω-2θ scans at different ω angles, where all the interested RLPs can be scanned in this map. RSM is particularly useful in determining the strain condition in epitaxial heterostructures from the relative position of the RLPs [54]. All the XRD data presented in this dissertation are taken using Philips X'Pert® MRD (Material Research Diffractometer) high-resolution (0.0001°) X-ray diffractometer.

2.2.2 Atomic Force Microscopy

Atomic force microscopy (AFM) makes use of a microscopic metal or semiconductor tip to probe the surface features of a thin film. Its ability of providing a high-resolution image of the surface morphology both laterally and vertically makes it useful for looking at small features and defects that other characterization tools may miss.

The principle of operation is based on the measurement of the deflection of the tip and cantilever using reflected laser light and a photodetector. There are three distinct modes that can be used to study the sample surface, which are contact mode, non-contact mode, and tapping mode. In contact mode, the tip is simply dragged across the surface, but this could damage both the tip and the sample. In non-contact mode, the tip is kept a constant distance from the surface and the force required to keep it is thereby mapped. However, this results in poor resolution due to small forces. Lastly, so-called tapping mode was proposed, which combines the two previous techniques and vibrates the cantilever at its resonant frequency. By doing this, an increase in sensitivity by several orders of magnitude is obtained because the local gradient van der Waals forces induce a change in the frequency, phase, and amplitude, which is fed back into the system.

Tapping mode is the most-frequently used operation method in AFM. Basically, the surface morphology is generated by plotting the force to track the surface features with equal distance between the probe tip and the layer surface. As illustrated in Figure 2.4, the tip is mounted at the end of a cantilever, bending in response to the force between the tip and the sample. As the cantilever flexes, the light from a laser is deflected onto the photodetector. A voltage is applied to the piezoelectric crystal that is attached to the cantilever to adjust the distance between cantilever and sample surface and maintain constant deflected laser intensity. In this manner, the mapping of the voltages gives direct information on the surface morphology. Surface features of ~5 nm in lateral direction and ~1 nm in vertical direction can be resolved. AFM is particularly useful for measuring the surface roughness of epitaxial layers and to understand the nature of defects in the layers. The AFM tool used in this study is a Veeco Dimension 3100, operating in tapping mode.

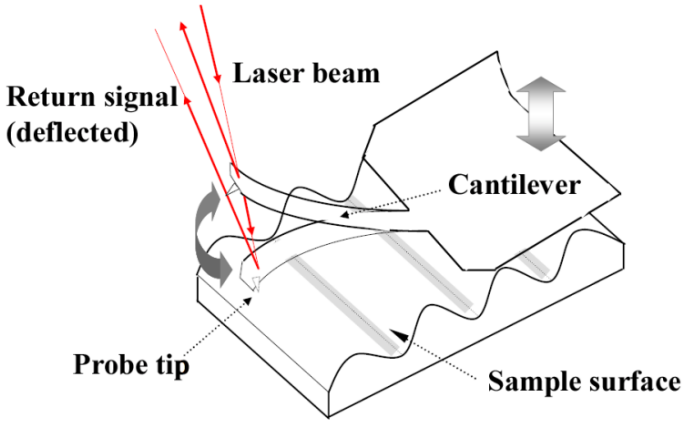

Figure 2.4: Schematic illustration for tapping mode operation of AFM.

2.2.3 Photoluminescence

Photoluminescence (PL) is the optical radiation emitted by a material resulting from its nonequilibrium state caused by an external light excitation. The photon energy of the incident light source (typically laser) must be high enough to generate electron-hole pairs across the

bandgap of the material being characterized. Upon excitation, the nonequilibrium and inhomogeneous excess carriers will diffuse around while undergoing radiative or nonradiative process that can be utilized to determine the fundamental recombination process, band gap energy, defect levels, and optical quality of a semiconductor material.

There are generally two ways to characterize PL. One is the spectral PL that is measured in steady states. Another is the time-resolved PL (TRPL) which investigates the dynamical process of excess carriers. A typical spectral PL setup consists of an excitation laser source, a high-resolution scanning spectrometer, and a detector. By measuring the scattered spontaneous emission from the sample as a function of wavelength, the PL spectrum is obtained, which contains the information regarding the bandgap and defect levels of a semiconductor. In the TRPL measurement, excitation is provided by a very short (~1 ps) light pulse from a tunable dye laser or Ti:sapphire laser and PL kinetics are measured using a fast photomultiplier tube (PMT) or streak camera. In this case, the emission intensity at a certain wavelength is recorded as a function of time, which gives the information on the recombination lifetime of excess carriers in the semiconductor.

We use an Accent RPM-2000 PL system equipped with a 785 nm diode laser and an InGaAs detector to perform the spectral PL measurement. The TRPL kinetics are obtained using an excitation wavelength of 680 nm with ~200 fs laser pulses and a near-infrared PMT detector.

2.2.4 Secondary Ion Mass Spectroscopy

Secondary ion mass spectroscopy (SIMS) is an analytical characterization technique used to trace the constituent elements, dopants, and impurities in solid materials, especially in semiconductors and thin films. Among the ion beam techniques, SIMS is the most sensitive

technique with detection limits for certain elements in the range of 10^{14} to 10^{15} cm^{-3}. It works by sputtering the sample surface with a focused ion beam (usually Cs^{+}), producing the physical damage to the materials. The ejected secondary ions are extracted and analyzed using a mass spectroscopy system. The number of ions ejected per incident ion is called the secondary ion yield. It can be plotted against the sputtering time; however, this can be more meaningful when the secondary ion yield is scaled to a unit of atomic concentration in comparison with previous calibration runs using ion-implanted samples and the sputtering time is scaled to a unit of depth by scaling with the depth of the hole formed when the sputtering is completed. In this way, the element profile as a function of depth is generated. One of the limitations often observed during SIMS is a high concentration of any elements abundant in atmosphere, such as carbon, nitrogen, or oxygen at the surface, showing gradual decrease of concentration into the material. SIMS data presented in this dissertation are gathered by Evans Analytical Group.

2.2.5 Hall Effect

The Hall effect measurement is a very simple technique for characterizing semiconductor material resistivity, carrier concentration, carrier type, and carrier mobility. The Hall effect occurs when an electromagnetic field is applied across a biased conductor, which produces a potential difference in the plane orthogonal to the magnetic field. The ratio of the measured voltage to the product of the current and magnetic field is defined as the Hall-coefficient (R_H), which is inversely proportional to the charge carrier density as:

$$n = \frac{1}{-qR_H} \text{ or } p = \frac{1}{qR_H}. \tag{2.3}$$

This technique was further developed by L. J. van der Pauw, and was applied on an arbitrarily shaped flat sample with four points on the circumference of the shape. According to van der Pauw's theorem, the resistivity ρ is given by:

$$\rho = 1.1331\left(\frac{t}{I}\right)\left(\frac{f_1\Delta V_1 + f_2\Delta V_2}{2}\right), \tag{2.4}$$

where t is the thickness of the film, I is the applied current, ΔV_i the voltage drop across the sample in various configurations, and f_1 and f_2 are the geometrical factors (that are unity for perfect squares).

Similarly, the mobility μ is related to the magnetic field B through the expression of:

$$\mu = 2.5 \times 10^7 \times \left(\frac{t}{I \cdot B \cdot \rho}\right)\left(\frac{\Delta V_3 + \Delta V_4}{2}\right) \tag{2.5}$$

and the bulk carrier concentration as a function of mobility μ and resistivity ρ is given by:

$$n \text{ or } p = \frac{1}{\rho \cdot q \cdot \mu} \tag{2.6}$$

In this dissertation, the Hall effect is measured by an Accent HL5500 system at room temperature.

2.2.6 Electrochemical Capacitance-Voltage Profiling

The capacitance-voltage (C-V) technique is very useful to characterize semiconductor structure that exists in the form of a capacitor. This technique exploits the fact that the width of the reverse-biased space-charge region or depletion region of the semiconductor junction devices such as *p-n* diodes and Shottky barrier devices depends on the applied voltage. The underlying principle of the electrochemical capacitance-voltage (ECV) is the same with the typical C-V

technique except that the piece of semiconductor material is immersed in an electrolyte. In ECV, the function of the electrolyte is to form the Shottky contact to the semiconductor surface as well as to selectively etch the semiconductor material in a defined opening when applying current. The charge carrier density N at the edge of the depletion layer is given by:

$$N = \frac{1}{q \cdot \varepsilon_0 \cdot \varepsilon_r \cdot A^2} \cdot \frac{C^3}{dC/dV}, \tag{2.7}$$

and the etched depth W_r is given by Faraday's law of electrolysis as follows:

$$W_r = \frac{M}{z \cdot F \cdot \rho \cdot A} \int I dt. \tag{2.8}$$

In Equation 2.7 and 2.8, q is the electron charge, ε_0 is permittivity of free space, ε_r is relative permittivity of semiconductor, A is the area of the opening, M is the molecular weight, z is the valence number of the semiconductor, ρ is the mass density, and I is the etching current. Alternative repetition of C-V measurements and etchings of contact area gives the profile of free carrier concentrations up to any depth. A drawback of ECV is its destructive nature.

In this study the ECV profiling is performed in an Accent PN4300 semiconductor profiler. This system uses a mixture of 0.2 M EDTA solution (ethylenediaminetetraacetic acid) and 10% ethylene diamine as the electrolyte.

CHAPTER 3

Growth and Performance of LETs and TLs with Zn-Doped Base

3.1 Growth and Doping of InAlGaAs/InP Materials

In(Al_xGa_{1-x})As/InP is the basic heterojunction that makes up of the complicated HBT and LET structures. The growth condition and doping behaviors of both InP and InAlGaAs alloys have been investigated. The materials are grown by MOCVD in a Thomas Swan 7×2" close-coupled showerhead (CCS) reactor system. Epipure^{TM} trimethylindium (TMIn), trimethylgallium (TMGa), trimethylaluminum (TMAl), and triethylgallium (TEGa) are used as column III precursors [55] and high-purity arsine (AsH_3) and phosphine (PH_3) are used as column V precursors. The dopant precursors include disilane (Si_2H_6) for *n*-type Si doping and diethylzinc (DEZn) for *p*-type Zn doping. The substrate is (001) InP with different small-angle misorientations from 0.02° to 0.25° towards $(01\bar{1})$. Epitaxial growth is carried out between 580 °C and 700 °C at a reactor chamber pressure of 100 Torr.

Figure 3.1 shows the surface morphology of undoped InGaAs and InP grown at 700 °C on InP substrates with different off-cut angles with respect to (001) plane. The thickness is 2 μm for InGaAs and 4 μm for InP. As evident from (a), (b), and (c), the InGaAs growth undergoes step-flow mode regardless of the substrate misorientation. Consequently, the actual off-cut angles can be estimated from the AFM images by measuring the average terrace width. However, the InP morphology has different features depending on the substrate misorientation. At a low off-cut angle of 0.02° in (d), the surface is very rough characterized by high-density of hillocks; and at a relatively large off-cut angle of 0.25° in (f), step-bunched surface is observed. Only at an off-cut angle of 0.06° does the InP growth develop a step-flow mode as indicated in (e). Since

hillocks appear when the surface step density is too low while step-bunching occurs when the step density is too high, there should be an optimal off-cut angle for establishing a stable step-flow growth mode. In the case of InP, the optimal angle is found to be between 0.05° and 0.1°. Although hillocks or step-bunching can be mitigated to some degree by changing the growth conditions such as growth rate and temperature [56,57], the most convenient and effective approach to it apparently is to use the substrates with optimized misorientation. Similar trend has been found in evaluating the optical quality of InGaAs/InAlAs QWs on InP substrates [58].

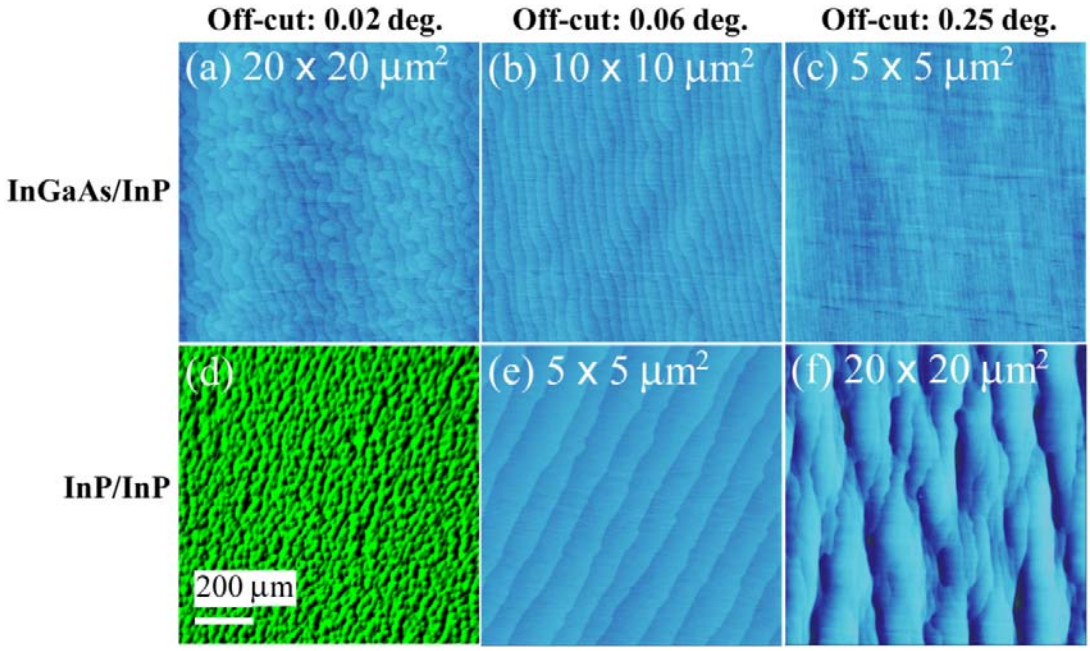

Figure 3.1: Surface morphology of InGaAs (first row) and InP (second row) on InP substrates with different off-cut angles. (d) is Nomarski micrograph and others are AFM images. For the AFM, the height scale bar for (f) is 20 nm and others are 5 nm.

Using the InP substrates with optimized off-cut angle, we are able to obtain $In(Al_xGa_{1-x})As$ and InP layers with excellent structural and optical quality at the growth temperature of 650 °C. Figure 3.2 shows the AFM images for Zn-doped InGaAs (InGaAs:Zn), $In(Al_{0.4}Ga_{0.6})As$:Zn, undoped InAlAs, and InP:Si layers in ~400 nm. Clear steps are observed for either doped or undoped materials, indicating superior surface morphology. Figure 3.3 shows the PL spectra for

the undoped InGaAs, $In(Al_{0.25}Ga_{0.75})As$, $In(Al_{0.4}Ga_{0.6})As$, and $In(Al_{0.6}Ga_{0.4})As$ alloys. The near band edge (NBE) emissions at 1643, 1340, 1210, and 1069 nm are very close to the theoretical values of 1646, 1340, 1215, and 1048 nm for x_{Al} =0, 0.25, 0.4, and 0.6, respectively, indicating the bandgap tunability. The low energy shoulder at high x_{Al} is attributed to the Al-related defect emission such as donor-acceptor pairs and becomes dominant with increasing x_{Al}.

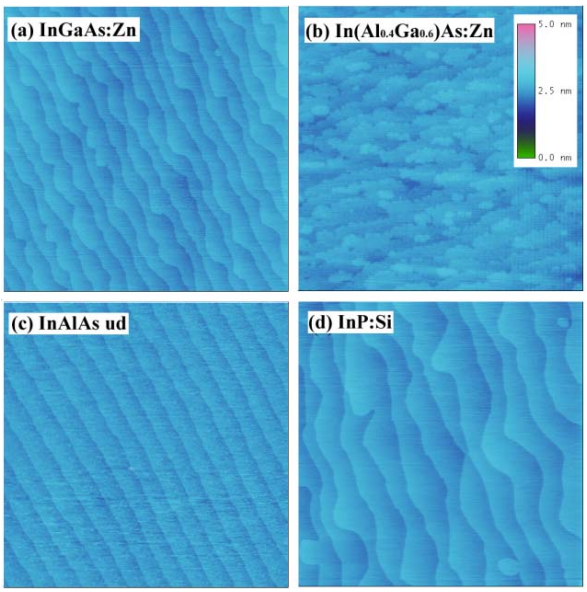

Figure 3.2: 5×5 μm^2 AFM images for (a) InGaAs:Zn, (b) $In(Al_{0.4}Ga_{0.6})As$:Zn, (c) undoped InAlAs, and (d) InP:Si.

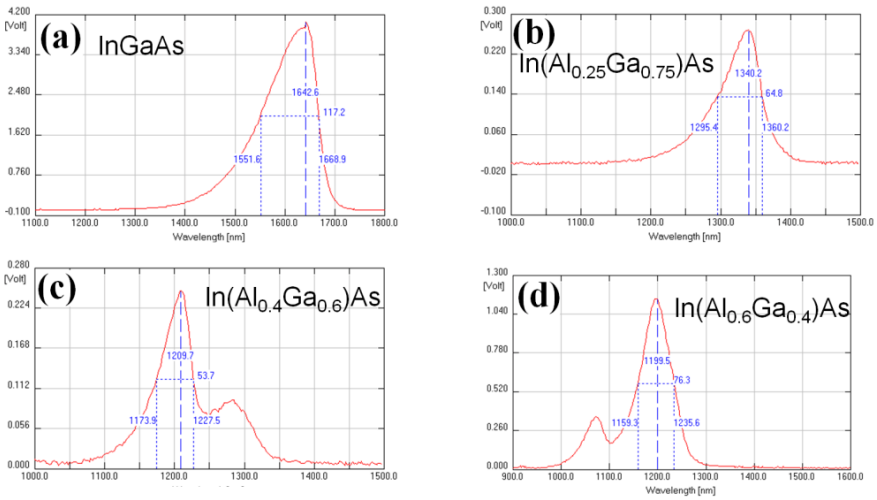

Figure 3.3: PL spectra for (a) InGaAs, (b) $In(Al_{0.25}Ga_{0.75})As$, (c) $In(Al_{0.4}Ga_{0.6})As$, and (d) $In(Al_{0.6}Ga_{0.4})As$.

The lattice matching and strain states of InAlGaAs layers are analyzed by XRD. Figure 3.4 (a) shows the XRD ω-2θ scans for InGaAs, InAlAs, and In($Al_{0.4}Ga_{0.6}$)As layers. Nearly lattice-matched condition and clear interference fringes are visible. RSM measurement around (105) reflection were performed to examine the strain status of InGaAs and InAlAs on InP, with the results displayed in Figure 3.4 (b). It is clear that the InAlAs and InGaAs (105) RLPs are on the perpendicular lines that pass through InP RLPs, suggesting both InAlAs and InGaAs layers are fully strained on the InP substrates. In particular, InAlAs is compressive strained while InGaAs is tensile strained in these samples. The strained layer preserves high structural quality without generating defects within the layer as opposed to the strain relaxation process.

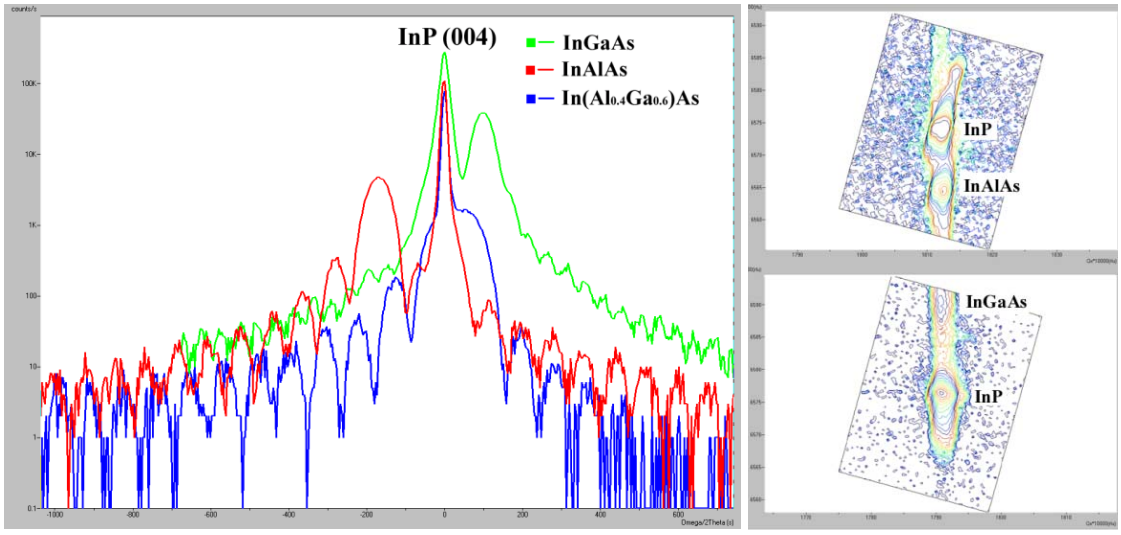

Figure 3.4: (a) XRD ω-2θ scans for InGaAs, InAlAs, and In($Al_{0.4}Ga_{0.6}$)As layers; (b) RSM measurements around (105) reflection for InAlAs/InP (upper panel) and InGaAs/InP (lower panel).

For a *p*-*n* junction-based device, successful doping for *n*- and *p*-type conductivity is critical for device operation. Si is a commonly-used high-efficient *n*-type dopant in most of the III-V semiconductors. Figure 3.5 (a) demonstrates the free electron concentration in In($Al_{0.25}Ga_{0.75}$)As layers as a function of disilane flow at different temperature. The carrier concentration was

measured by Hall effect at room temperature. As indicated in this graph, the free electron concentration is strongly dependent on the growth temperature. A higher temperature allows for a higher doping level, which is attributed to the improved cracking efficiency of disilane. For Si doping in InP, a doping level as high as 2×10^{19} cm^{-3} is attainable. On the other hand, the *p*-type doping seems to more tricky. Zn was initially employed as the *p*-type dopant since Zn is commonly used in InAlGaAs and InGaAsP materials due to its high activation efficiency and wide linear range of hole level attainable. Figure 3.5 (b) shows the free hole concentration in $In(Al_{0.25}Ga_{0.75})As$ layers as a function of DEZn flow at 650 and 600 ^{o}C. The hole concentration initially increases with DEZn flow and then saturates at a certain point. A lower temperature leads to higher doping level, as opposed to that in Si doping. It is critical to keep the Zn-doping away from the saturation point to suppress Zn diffusion, which is the major issue of Zn-doping. The details of Zn diffusion will be covered later in this chapter. In case of InP, the highest hole level that can be obtained is ~ 2×10^{18} cm^{-3} limited by the solid solubility of Zn in InP.

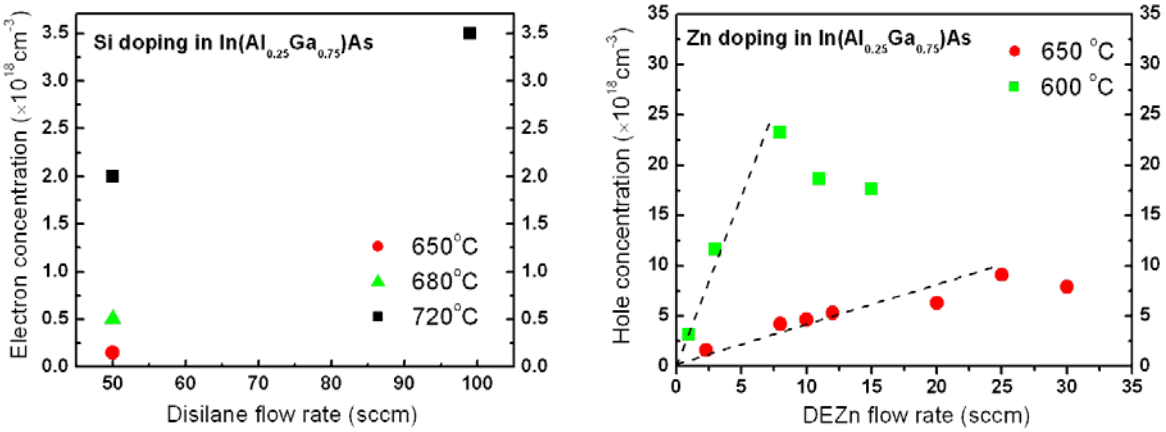

Figure 3.5: (a) Dependence of electron concentration in $In(Al_{0.25}Ga_{0.75})As$ layers on disilane flow at 650, 680, and 720 ^{o}C; (b) Dependence of hole concentration in $In(Al_{0.25}Ga_{0.75})As$ layers on DEZn flow at 650 and 600 ^{o}C.

3.2 Performances Zn-doped HBTs and LETs

InP/InAlGaAs HBT and LET were grown after the growth rate, composition and doping calibration of each layer. A typical *NpN* LET structure (here, capital letter *N* denotes wider bandgap *n*-type materials) consists of a Si-doped InP (InP:Si) subcollector (150 nm, n=1×10^{19} cm^{-3}), an undoped $In_{0.52}Al_{0.48}As$ (InAlAs:ud) collector (450 nm), an undoped $In_{0.53}(Al_xGa_{1-x})_{0.47}As$ ($In(Al_xGa_{1-x})As$:ud) grading layer (60 nm) with x_{Al} from 1 to 0.25, a base/active region (100 nm), a *p*-type $In_{0.53}(Al_{0.25}Ga_{0.75})_{0.47}As$ base contact layer (50 nm, p=8×10^{18} cm^{-3}), an lightly doped InP:Si emitter spacer (75 nm, n=2×10^{17} cm^{-3}), an InP:Si emitter (150 nm, n=5×10^{18} cm^{-3}), and an InP:Si^{+} emitter contact cap (50 nm, n=1×10^{19} cm^{-3}). The base/active region consists of undoped compressively-strained $In_{0.58}Ga_{0.42}As$ QWs embedded in the *p*-type (p=2×10^{18} cm^{-3}) $In_{0.53}(Al_{0.25}Ga_{0.75})_{0.47}As$ confining layers doped with Zn.

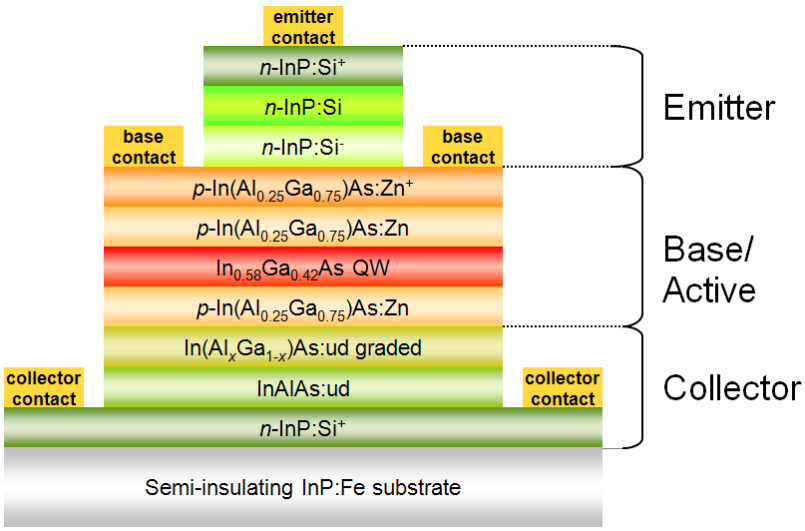

Figure 3.6: Schematic epitaxial and device structure of an InP/InAlGaAs LET with a single InGaAs quantum well embedded in the base/active region.

The devices were fabricated using standard optical lithography and wet chemical etching to form an emitter and base mesa structure. The first step employs a H_3PO_4 and HCl mixture (3:1) as a selective etchant between the emitter and base layers to create the emitter mesa, and then a

second selective etching process was applied using a diluted H_2SO_4 and H_2O_2 mixture (H_2SO_4:H_2O_2:H_2O=1:8:80) to form a base/collector mesa. E-beam evaporation was used to deposit a AuGe/Ni/Au metal stack for the emitter and collector ohmic contacts while Au/Zn/Au was used for the base ohmic contacts. Figure 3.6 shows a schematic epitaxial and device structure of an InP/InAlGaAs LET with an InGaAs single QW (SQW) embedded in the base/active region.

For electrical measurements, current and bias voltages (common emitter operation) are provided using a HP-4142 DC power source. Electroluminescence (EL) spectra of the LET are obtained by measuring the light output of the device through the substrate of the sample with a Horiba-Jobin-Yvon Triax 320 spectrometer, while the optical output power of the devices is measured using a UDT Ge photodetectors and S370 optometer.

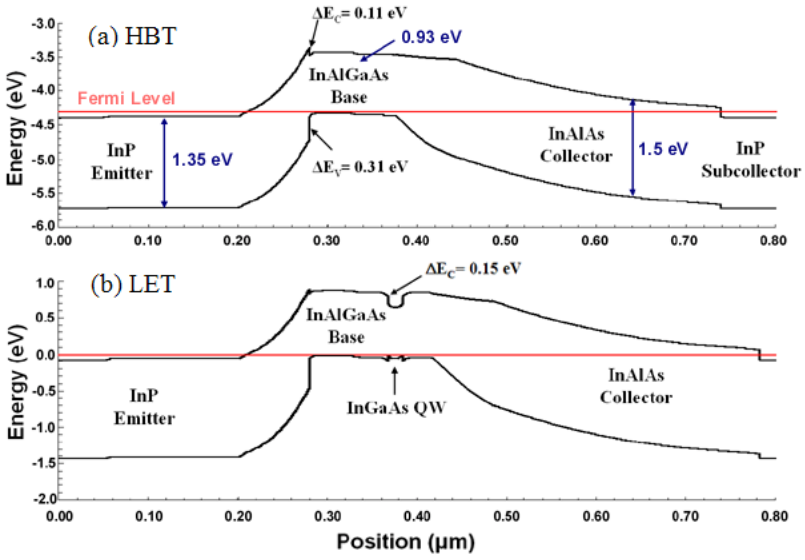

Figure 3.7: Calculated band diagrams for (a) HBT and (b) LET.

In order to compare the DC performances, a standard HBT structure was also grown as the baseline. The HBT epitaxial structure is identical to the LET structure except for the insertion of the SQW in the base region. The LET structure has a 12 nm InGaAs QW in the middle of the

base/active region, while the HBT structure contains a single *p*-In($Al_{0.25}Ga_{0.75}$)As:Zn base layer. The total thickness of the base (or base/active) layer in both structures is 100 nm. The calculated band diagrams for the both devices are displayed in Figure 3.7.

The LET and HBT were grown after calibration of each layer. The samples were mirror-like after growth. AFM, XRD, PL and ECV characterization for the LET wafer are summarized in Figure 3.8 (a), (b), (c) and (d), respectively. Atomic steps in AFM and clear fringes in XRD were observed, indicating good surface and interface quality. Strong emission at 1644 nm was obtained in PL spectrum, corresponding to the radiative recombination process in the QW. ECV clearly shows the carrier concentration and polarity profile in the device.

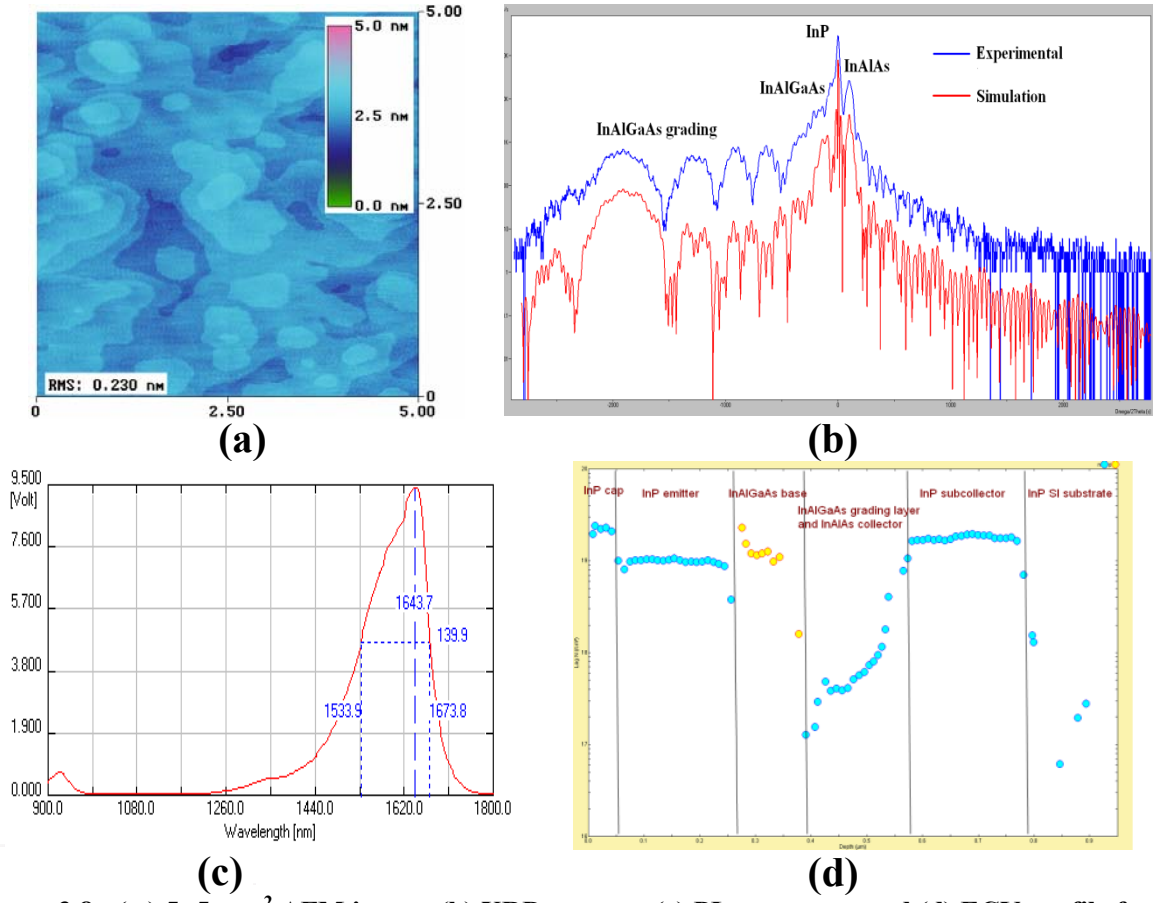

Figure 3.8: (a) 5×5 μm^2 AFM image, (b) XRD pattern, (c) PL spectrum, and (d) ECV profile for the LET.

Transmission line method (TLM) was employed to evaluate the contact resistance (R_c) and sheet resistance (R_s) of the devices. In TLM, a serial of identical metal pads are deposited in a row on the semiconductor surface with different spacing. By plotting the resistance between two pads against the distance of their spacing, a line is drawn and R_c and R_s can be estimated from its intercept and slope, respectively. Table 3.1 is the calculated results for the LET wafer from the TLM measurement. The base contact resistance is about 573 $\Omega\cdot\mu m^2$, which is similar to those in high-performance HBTs. The emitter and collector resistance is very low.

Table 3.1: Contact resistance and sheet resistance for the emitter, base and collector.

	R_c ($\Omega\cdot\mu m^2$)	R_s ($\Omega/\square$)
Emitter	66	55
Base	573	1063
Collector	47	23

The emitter area is 120×120 μm^2 for both devices. Figure 3.9 (a) shows the common-emitter output characteristics of the InAlGaAs/InP HBT and LET with the collector-to-emitter voltage (V_{CE}) swept from 0 to 8 V, and the base current (I_B) varied in increments from 0 to 0.1 mA in 10 μA steps. The DC current gain ($\beta=\Delta I_C/\Delta I_B$) is ~220 for the HBT and ~45 for the LET. Figure 3.9 (b) is a plot of I_C and I_B against V_{BE} with V_{BC}=0 V, known as the Gummel plot, for both devices. The base current ideal factor (n) is 1.27 and 1.32 for the LET and HBT, respectively, indicating that the base recombination current is the dominant base current component [6]. The collector current ideal factor for both devices is close to unity, suggesting a diffusion-limited current. Note that the collector currents are almost the same for both devices, whereas the base current in the LET is much larger than in the HBT for a same biased voltage. When electrons are injected from the emitter and swept across the base, a fraction of them recombine radiatively in the QW and produce a recombination current supplied by the base current. This current is negligible compared to collector current but much larger than other base

current components. As a result, the LET owns a similar collector current and a reduced transistor gain for a given bias.

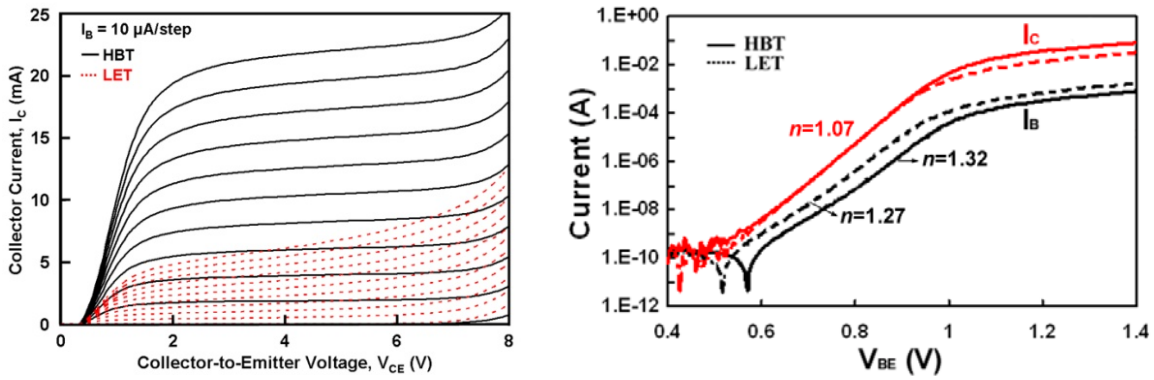

(a) (b)

Figure 3.9: (a) The common-emitter output characteristics of the InP/InAlGaAs HBT (solid lines) and LET (dashed lines); (b) Gummel plot for HBT (solid lines) and LET (dashed lines).

Figure 3.10 (a) shows the light emission spectra taken from the LET at different base currents and different collector-to-emitter voltages. The emission wavelength of the LET is centered near 1650 nm, which matches well with the PL spectrum. There is no wavelength shift with base current injection level up to 4 mA. As indicated in Figure 3.10 (b), the light output increases almost linearly with I_B and is independent of V_{CE}, which is consistent with the optical output characteristics of GaAs-based LETs [2,16].

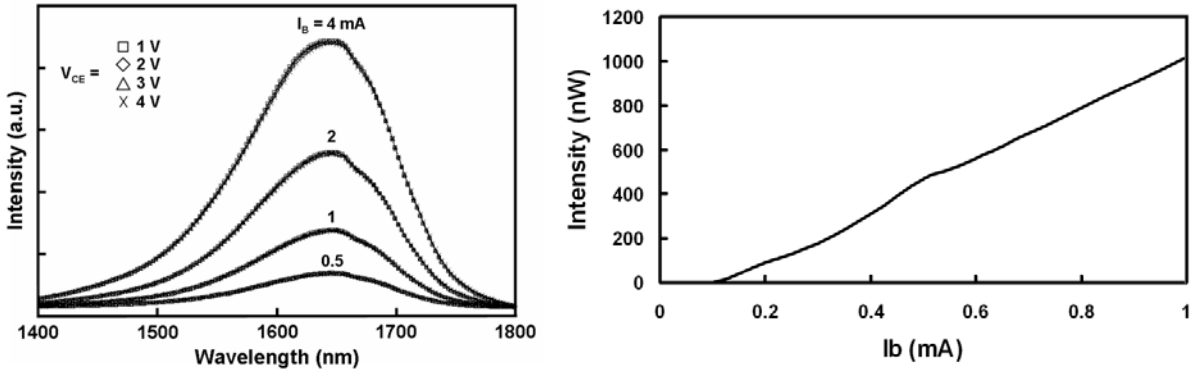

(a) (b)

Figure 3.10: (a) EL spectra for the LET measured at different I_B and different V_{CE}; (b) Light intensity as a function of I_B.

To get an insight into the effects of the design of the active region on the current gain and the optical output power of the device, three LET structures with different number of QWs - a SQW, double QWs (DQW), and three-period multiple QWs (MQW) - were grown and fabricated. All the structures are similar to that shown in Figure 3.6 except for the number of QWs in base/active region. The QW thickness varies in going from 20 nm for SQW, 10 nm for DQW to 8 nm for MQW. The total base thickness is 200 nm in the MQW LET. Shown in Figure 3.11 are the EL spectra for the three devices measured with I_B=4 mA and V_{CE}=4 V. Stronger light output is observed from the LETs with MQWs in the base/active region, indicating that additional QWs can capture more electrons and effectively increase the radiative recombination in the LET. A blue shift in the emission wavelength with increasing number of QWs is due to the reduced thickness of QW. Improved collection of minority carriers in the QWs also reduces the current gain of the transistor as the QW number in the base/active region increases. Design of the base/active region of the LET requires a trade-off between the current gain of the transistor and the resulting light output.

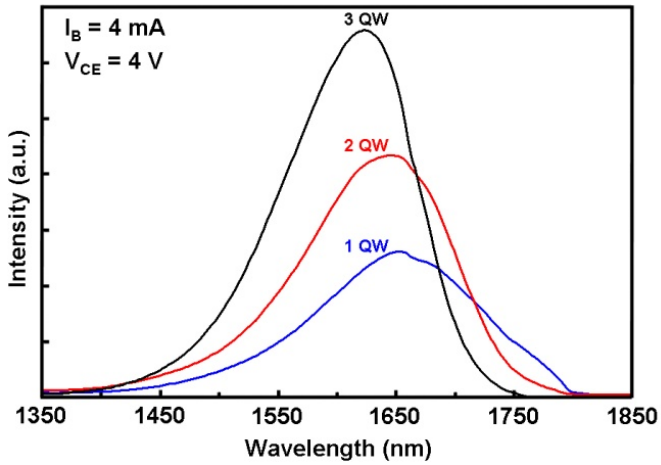

Figure 3.11: EL spectra for the LETs with a SQW, two and three QWs in the base/active region.

3.3 Design and Performance of a LD

Before getting to the TLs, the conventional LDs have been studied to examine the design criteria of a laser structure and verify the optical quality of the active region. Semiconductor LDs differ from LEDs structurally in that LDs must have waveguides and cladding layers to confine optical modes. When photons in the confined mode travel in the waveguide layer, optical gain is produced in the active media by generating "stimulated" photons with the same frequency, polarization and direction. By providing the feedback cavity, photons will be reflected several times from each facet before they are emitted. Apart from the light amplification by stimulated emission, photons are also lost due to absorption and incomplete reflection from the facets. When the amplification or gain eventually surpasses the total loss, the LD begins to "lase". All the excess carriers beyond threshold are converted to photons.

Layer	Comment	Material	Thickness (nm)	Type	Dopant	Level (cm^{-3})
14	P-Contact	$In_{0.53}Ga_{0.53}As$	20	P+	Zn	1.20E+19
13	Cladding	InP	1400	P	Zn	2.00E+18
12	EBL	$In_{0.52}Al_{0.48}As$	30	UD		
11	Waveguide	$In_{0.53}(Al_xGa_{1-x})_{0.47}As$	150	UD		x = 0.4 to 0.6
10	Barrier	$In_{0.53}(Al_{0.4}Ga_{0.6})_{0.47}As$	15	UD		
9	QW	$In_{0.58}Ga_{0.42}As$	6	UD		
8	Barrier	$In_{0.53}(Al_{0.4}Ga_{0.6})_{0.47}As$	15	UD		
7	QW	$In_{0.58}Ga_{0.42}As$	6	UD		
6	Barrier	$In_{0.53}(Al_{0.4}Ga_{0.6})_{0.47}As$	15	UD		
5	QW	$In_{0.58}Ga_{0.42}As$	6	UD		
4	Barrier	$In_{0.53}(Al_{0.4}Ga_{0.6})_{0.47}As$	15	UD		
3	Waveguide	$In_{0.53}(Al_xGa_{1-x})_{0.47}As$	150	UD		x = 0.4 to 0.6
2	Cladding	InP	1000	N	Si	1.50E+18
1	Contact	InP	200	N+	Si	1.00E+19
0	Substrate	InP		N+	Si	

(a)

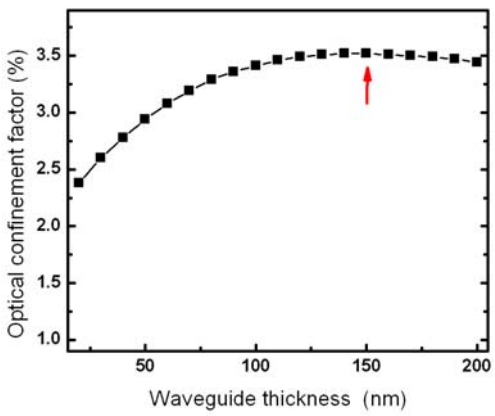

(b)

Figure 3.12: (a) Epitaxial structure of the *p-i-n* MQW LD; (b) Optical confinement factor of the MQW as a function of waveguide thickness; arrow indicates the thickness selected.

A *p-i-n* InP/InAlGaAs LD structure was designed, grown, and fabricated. Figure 3.12 (a) shows the epitaxial structure of the LD. The structure consists of three-pair undoped $In_{0.58}Ga_{0.42}As/In(Al_{0.4}Ga_{0.6})As$ (6/15 nm) compressive-strained MQW active region, sandwiched by $In(Al_xGa_{1-x})As$ grading waveguide layers with x_{Al} from 0.4 to 0.6 and thick InP cladding

layers. The thickness of the waveguide layers was optimized by calculating the transverse (1D) optical confinement factor (Γ) in the MQWs [59], with the result displayed in Figure 3.12 (b). With the increase of waveguide thickness, Γ increases and then reaches the maximum value of 3.5% at the thickness of 150 nm, which was adopted in the actual device as indicated by arrow. The band diagram of the LD is illustrated in Figure 3.13 (a) [60]. The grading layers eliminate any potential barriers and facilitate the injection of holes and electrons and the 30 nm InAlAs between the waveguide and *p*-cladding layer serves as a good electron blocking layer (EBL) to suppress electron overflow due to its high conduction band offset. Figure 3.13 (b) shows the calculated near field optical intensity distribution in the transverse direction. A single fundamental mode is evident.

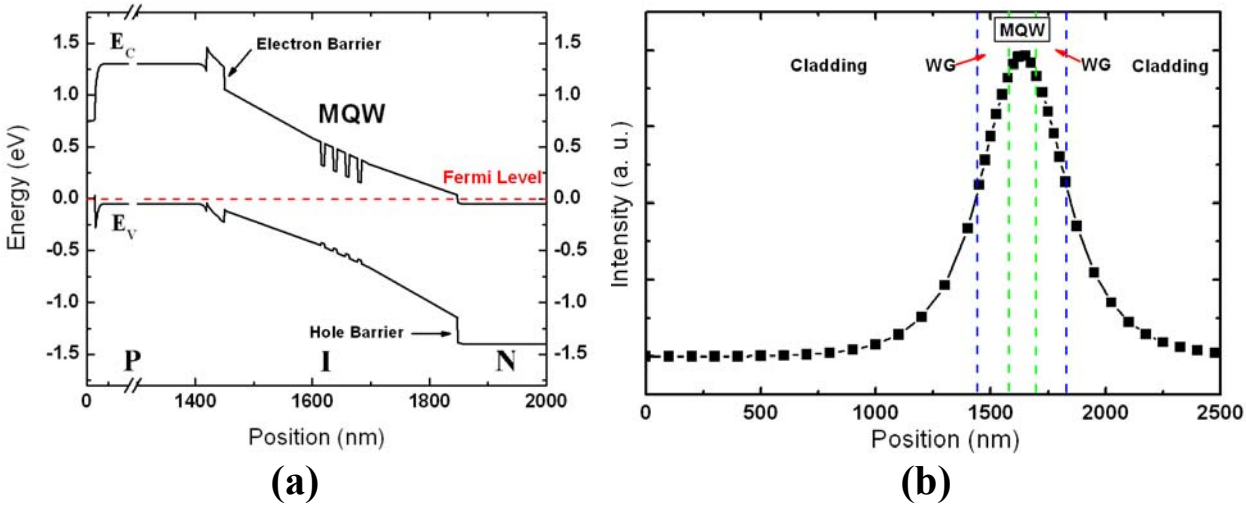

Figure 3.13: (a) Calculated band diagram of the *p-i-n* LD; (b) Near field optical intensity distribution.

The material growth was done after calibration of the composition, thickness, and doping level of each layer. The wafer was specular after growth. The PL and XRD results of the epitaxial wafer are summarized in Figure 3.14 (a) and (b), respectively. Strong emission at 1536 nm was observed and XRD result matches with designed structure in simulation, indicating good structural and optical qualities of the wafer.

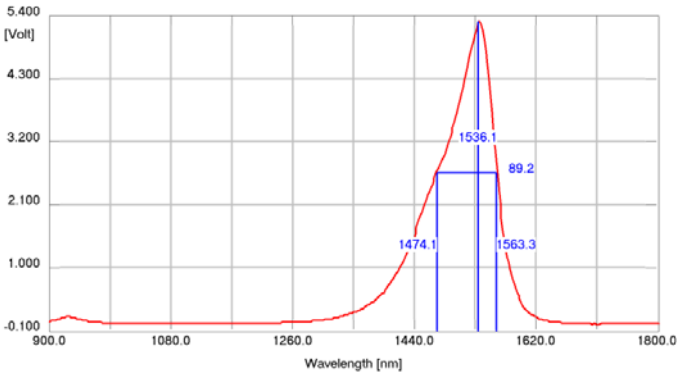

(a)

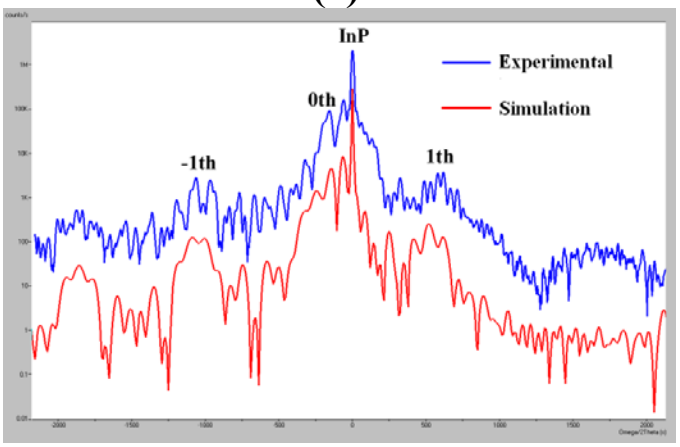

(b)

Figure 3.14: (a) PL spectrum and (b) XRD ω-2θ scan for the *p-i-n* LD.

The wafer was processed into gain-guided lasers. First, a 9-μm-wide *p*-metal stack consisting of Au/Zn/Au was deposited on the top *p*-side of the wafer. Then the wafer was lapped to a thickness of ~100 μm from the substrate side and AuGe/Ni/Au was deposited to form the *n*-contact. After annealing of the contacts, the wafer was cleaved normal to the *p*-metal stripes to form Fabry-Pérot (FP) facets of 400 μm long.

The 9×400 μm^2 laser demonstrates CW operation at room temperature. From the output-current (*L-I*) curve shown in Figure 3.15 (a), a change from spontaneous emission to stimulated emission at threshold current (I_{th}) of 65 mA is evident at 23 ^{o}C, corresponding to a threshold current density (J_{th}) of 1.8 kA/cm^2. At liquid nitrogen (LN) temperature of -180 ^{o}C, J_{th} is

reduced to 69 A/cm^2 due to the suppression of nonradiative recombination. From Figure 3.15 (b) the emission wavelength at room temperature is 1545 nm, very close to 1536 nm in PL measurement. A multi-longitude mode is observed at high current injection levels. These results indicate superior optical quality of the active region, which can be adopted in the TL design.

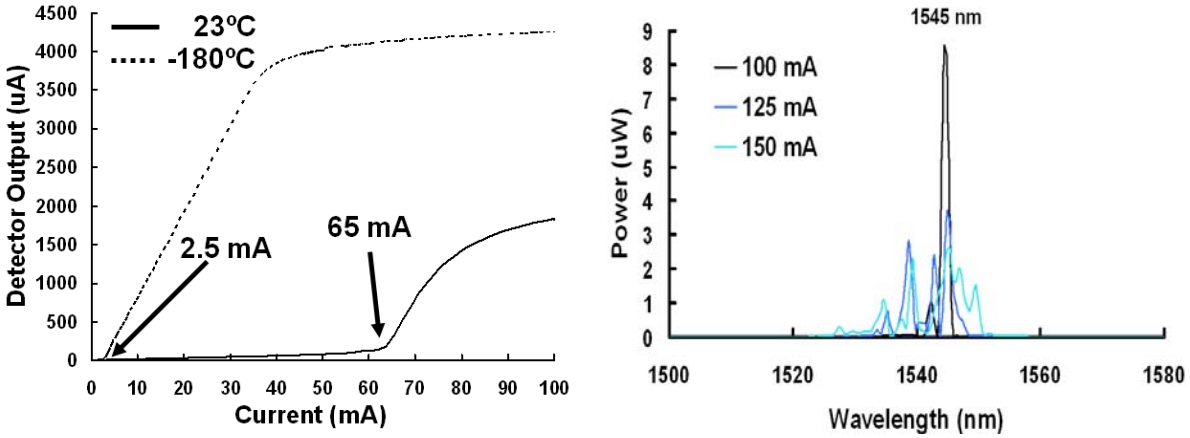

Figure 3.15: (a) *L-I* curves at 23 °C and -180 °C; (b) Spectra taken at different injection level at 23 °C after lasing.

3.4 Demonstration of a Zn-doped TL

As compared to LETs, TLs are fundamentally more important in providing high-speed, high-power, collimated, and monochromatic light sources and are more technically challenging as well. A TL was designed based on the MQW LET and the MQW LD structures. In the structure, the emitter and collector serve as the cladding layers and the base as the waveguide and active region. First, the total emitter thickness is increased to 1430 nm to provide optical confinement, which is similar to the cladding layer thickness used in the LD. Then an active region with three-pair $In_{0.58}Ga_{0.42}As/In(Al_{0.25}Ga_{0.75})As$ MQW separated by $In(Al_{0.25}Ga_{0.75})As$:Zn barriers is employed. The collector is the same grading InAlGaAs and InAlAs as in LETs. The full epitaxial structure is shown in Figure 3.16.

Layer	Comment	Material	Thickness (nm)	Type	Dopant	Level (cm^{-3})
21	Emitter Contact	InP	55	N+	Si	1.00E+19
20	Emitter/Cladding	InP	1300	N	Si	5.00E+18
19	Emitter Spacer	InP	75	N	Si	2.50E+18
18	Base Contact	$In_{0.53}(Al_{0.25}Ga_{0.75})_{0.47}As$	50	P+	Zn	1.00E+19
17	Base/Waveguide	$In_{0.53}(Al_{0.25}Ga_{0.75})_{0.47}As$	38.5	P	Zn	5.30E+18
16	Spacer	$In_{0.53}(Al_{0.25}Ga_{0.75})_{0.47}As$	6	UD		
15	QW	$In_{0.58}Ga_{0.42}As$	8	UD		
14	Spacer	$In_{0.53}(Al_{0.25}Ga_{0.75})_{0.47}As$	6	UD		
13	Base	$In_{0.53}(Al_{0.25}Ga_{0.75})_{0.47}As$	6	P	Zn	5.30E+18
12	Spacer	$In_{0.53}(Al_{0.25}Ga_{0.75})_{0.47}As$	6	UD		
11	QW	$In_{0.58}Ga_{0.42}As$	8	UD		
10	Spacer	$In_{0.53}(Al_{0.25}Ga_{0.75})_{0.47}As$	6	UD		
9	Base	$In_{0.53}(Al_{0.25}Ga_{0.75})_{0.47}As$	6	P	Zn	5.30E+18
8	Spacer	$In_{0.53}(Al_{0.25}Ga_{0.75})_{0.47}As$	6	UD		
7	QW	$In_{0.58}Ga_{0.42}As$	8	UD		
6	Spacer	$In_{0.53}(Al_{0.25}Ga_{0.75})_{0.47}As$	6	UD		
5	Base/Waveguide	$In_{0.53}(Al_{0.25}Ga_{0.75})_{0.47}As$	39.5	P+	Zn	1.00E+19
4	Spacer/Waveguide	$In_{0.53}(Al_{0.25}Ga_{0.75})_{0.47}As$	15	UD		
3	Collector Grading	$In_{0.53}(Al_xGa_{1-x})_{0.47}As$	60	UD		x = 0.25 to 1
2	Collector/Cladding	$In_{0.52}Al_{0.48}As$	300	UD		
1	Collector Contact	InP	200	N+	Si	1.00E+19
0	Substrate	InP		Semi-Insulating		

Figure 3.16: Epitaxial structure of the *NpN* MQW TL.

The waveguide/base thickness was optimized by calculating Γ for the MQW. Shown in Figure 3.17 (a) is the dependence of Γ on the waveguide thickness (layer 5 and 17 in Figure 3.16). A maximum value of 5.5% can be obtained at the thickness of 70 nm; however, this is too large for a practical HBT. Instead, a thickness of ~40 nm was employed as indicated by arrow and the total base thickness was kept as 200 nm, corresponding to a Γ of 5.36%. Figure 3.17 (b) displays the calculated band diagram of the MQW *NpN* TL.

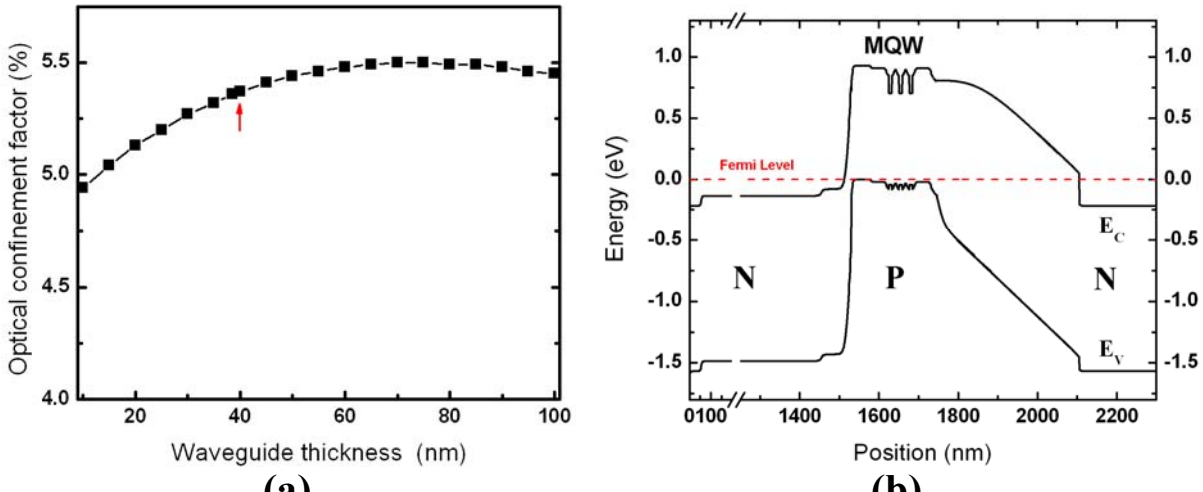

Figure 3.17: (a) Γ of the MQW as a function of waveguide thickness; arrow indicates the thickness selected; (b) Calculated band diagram of the *NpN* TL.

Device was fabricated utilizing six masks and three wet etching steps. After forming the emitter and base mesa and depositing the contact metals, the device was isolated by etching down into the SI substrate to a depth of 0.75 μm. After that the sample was lapped to a thickness of ~ 125 μm. Then it was cleaved normal to the emitter stripes to form FP facets, and the substrate side was alloyed onto Cu heat sinks. The heat sunk wafer was then mounted onto a Cu block for testing. To test at low temperature, the Cu block was kept partially submerged in liquid nitrogen where a temperature sensor placed on the surface of the block. The device has a ridge waveguide structure and the emitter size is 8×450 μm^2.

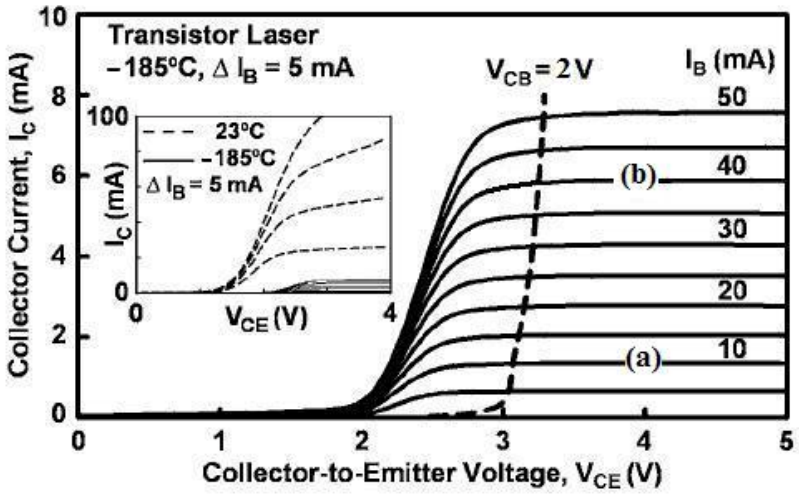

Figure 3.18: *I-V* curves of the TL operated at -185 °C. The dotted line indicates the V_{CE} bias at which V_{CB} =2 V. The inset shows the family curves at 23 °C (dashed lines) and -185 °C (solid lines).

The common-emitter output characteristics of the TL measured at LN temperature are shown in Figure 3.18. I_B is increased in 5 mA intervals from 0 to 50 mA with V_{CE} swept from 0 to 5 V. An important feature to note is that the device is not turned on until the BC junction is reverse biased by about 2 V as indicated by the dashed line. Once the transistor is biased above the knee voltage, the collector current reaches its maximum value and the current gain becomes β=0.14 and remains nearly constant with bias current. The inset shows a comparison of these

results with the same device that has β=5.5 when operated at room temperature. When the ambient temperature is lowered, significant compression of the *I-V* curves is observed due to the enhanced radiative recombination.

The light intensity-base current (L-I_B) characteristics of the device were measured with a UDT Ge photodetector aligned to a single output facet of the device. Figure 3.19 (a) shows the L-I_B curves at -185 °C and 23 °C with CW operation of the device. The device behaves like an LET and fails to lase at room temperature. However, light emission is significantly enhanced at -185 °C and a "kink" in the L-I_B curve is observed. These data clearly show the change from spontaneous to stimulated emission and give the I_{th} as 12 mA and J_{th} as 330 A/cm^2. This is the first demonstration of a TL working around 1.55 μm [61]. For V_{CE}=4 V, the output intensity reduces slightly compared to V_{CE}=3 V because of device heating.

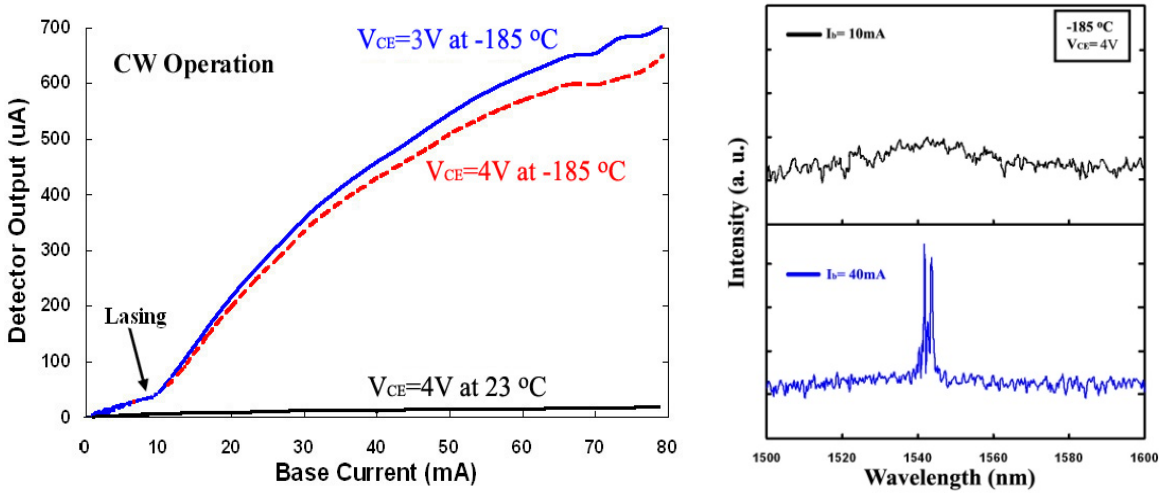

Figure 3.19: (a) L-I_B at 23 °C and -185 °C; (b) EL spectra taken at I_B of 10 mA and 40 mA at -185 °C.

To detect the output spectrum of the TL, the light emission from the front facet is coupled into a multimode fiber probe with a core diameter of 25 μm, which captures only a small fraction of the laser output. The other end of the fiber is fed into an optical spectrum analyzer for

measurement. Figure 3.19 (b) shows the output spectra at an injection level of 10 mA and 40 mA with V_{CE}=4 V. Direct manifestation of laser action at 1.54 μm is observed at 40 mA. Noisy feature in the spectra comes from the poor coupling efficiency between the fiber and TL.

Despite the poor performances of the TL, these data clearly establish the feasibility of the CW laser operation of InP/InAlGaAs TLs. There is still much room for improvement because of the relatively poor material quality and simple transistor geometry. As far as the material is concerned, the high turn-on voltage and low-temperature operation could be attributed to Zn diffusion in the device, which will be elaborated in the next section.

3.5 Zn Diffusion and Its Effect on Device Performances

Zn is well documented to diffuse easily in the semiconductor matrix and it is difficult to contain them in the layer that is intended to be Zn-doped only during the epitaxial growth. In the case of two-terminal *p*-*n* junction devices such as LEDs and LDs, the doping profile of Zn can be engineered to mitigate the problem of Zn diffusion [62]; however, Zn diffusion cannot be easily engineered in three-terminal *NpN* LET and HBT structures [44]. To study the Zn distribution profile, SIMS was performed on one of the SQW LETs. The depth and concentration profile of Zn and Si with P, As, and Al marker in the InP/InAlGaAs/InAlAs LET is displayed in Figure 3.20. It is evident that during the 250 nm emitter growth, Zn diffuses into the emitter region, pushing the Zn profile towards the growth direction by about 50 nm, as well as into the undoped collector region about 60 nm. It also inevitably diffuses into the QW region, smearing the QW profile. Note that the doping level in the base region is around 3×10^{18} cm^{-3}. In order to achieve population inversion and thus realize laser operation of the device, this doping level should be at least one order of magnitude larger [16], which would make the diffusion even more severe.

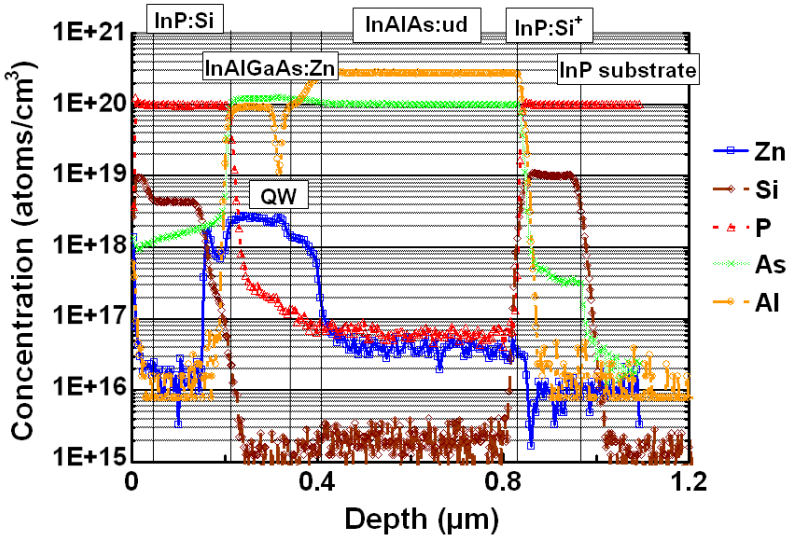

Figure 3.20: SIMS profile of a SQW LET with Zn-doped base.

The diffusion of Zn in semiconductors has been widely studied. It has been generally accepted that Zn diffusion occurs via an interstitial-substitutional mechanism involving intrinsic point defects. An interstitial Zn atom diffuses quickly until it is trapped by a group III vacancy and thus incorporated as a substitutional Zn atom, which is much less mobile. The high diffusivity of Zn interstitials has been confirmed by the observation of double diffusion front in InP [63], and they were considered to be the major diffusion source [64]. If the creation of Zn interstitials can be suppressed, an abrupt doping profile with minimized Zn diffusion is expected.

One consideration for the generation of Zn interstitials is from the kick-out mechanism. During the growth of n^+-subcollector layer for an HBT structure, the Fermi level at the growing surface is pinned close to midgap resulting in band bending near the growing front, which leads to excess nonequilibrium group III interstitials during the subsequent growth [65]. These interstitials flow into the base region, kick out the substitutional Zn atoms and thereby form the Zn interstitials. Another origin of Zn interstitials can reside in doping of the Zn-doped layer itself. When performing in-situ Zn doping, Zn atoms tend to be incorporated into the

substitutional sites when the doping level is low; while up to a certain point, they start to occupy interstitial sites as well [62], where they compensate the active hole level since the interstitial Zn is assumed to behave like a donor. A calculation based on a point-defect equilibrium model in InP shows the increasing of Zn interstitial level with the dopant partial pressure during the growth, which eventually goes higher than the substitutional Zn level [66]. On the other hand, besides being trapped by a vacancy, a diffusive Zn interstitial could in turn replace with a substitutional group III atom [67] and thereby create a group III interstitial, which makes the situation even more complicated.

To identify the Zn diffusion mechanisms, we have studied the Zn distribution profiles in the LETs and HBTs with different growth conditions and doping levels and proposed the growth scheme to control the Zn diffusion in HBT-like structures.

It is evident that in the LET in Figure 3.20 Zn from the base region diffuses into both the emitter and the adjacent graded collector. However, Zn diffusion stops at the interface of InP:Si emitter layer (not at the interface of InP:Si^- emitter spacer layer), and Zn pile-up is formed at the InP:Si^-/InP:Si interface, which was also observed by other group [68]. The pile-up phenomenon is attributed to the presence of a strong electric filed within the InP:Si/InP:Si^-/InAlGaAs:Zn junction, which retards the motion of the positively charge Zn interstitials just like a *p*-*n* junction retards majority carriers' motion to other sides with opposite polarity [69,70].

Now we can divide a combined phenomenon of Zn diffusion in the HBT-like structure with three mechanisms that are associated with the growth and doping of the (1) subcollector, (2) base, and (3) emitter (or emitter spacer). The first Zn diffusion mechanism is related to the growth treatment and doping level of the InP:Si^+ subcollector. As discussed above, the generation of group III interstitials will invoke Zn diffusion by the kick-out mechanism. A growth interruption

(GI) after subcollector growth was introduced for the out-diffusion of the excess interstitials and was found to be effective in suppressing the abnormal Zn diffusion [68,71,72]. Also, a relatively low collector doping level (mid-10^{18} cm^{-3}) was proved to be favorable in suppressing the generation of excess group III interstitials [68]. Here we designate these two conditions as a C+ condition, which represents the *favorable* condition for the *suppression* of Zn diffusion induced by the collector and subcollector growth. On the contrary, a heavily-doped ($\geq 1\times10^{19}$ cm^{-3}) subcollector without GI is referred to as a C− condition, which represents *unfavorable* condition for the *suppression* of Zn diffusion during the growth of collector and subcollector layers. The second mechanism is relevant to the Zn doping in the InAlGaAs base region. Following the point-defect equilibrium theory, we believe that at a hole concentration that is close to or beyond its saturation point, the InAlGaAs layer will contain a significant amount of Zn interstitials. A doping level lower than its saturation point should have less Zn interstitials. By the same token, therefore, a doping condition that has a hole concentration lower than its saturation point is referred to as a B+ condition (favorable condition for the suppression of Zn diffusion during the growth of a base layer) and as B− condition in the opposite case, that is, a hole concentration close to or beyond its saturation point. The third is related to the adjacent InP:Si^- emitter spacer. It is clear to see from Figure 3.20 that a lightly doped InP layer (n~2×10^{17} cm^{-3}) is not able to block Zn diffusion. Naturally, we expect some Zn "blocking effect" from a highly or intermediately doped InP emitter spacer, which is designated as an E+ condition. In the same manner, an E− condition is used to describe a lightly-doped InP emitter spacer.

Combination of these mechanisms complicates the analysis of Zn diffusion profiles in many cases. In the following, we present the data showing how these mechanisms determine the direction of Zn diffusion. The growth conditions corresponding to several cases with

combinations of each favorable or unfavorable condition employed in this study are summarized in Table 3.2.

Table 3.2: Growth conditions of the structures for several combinations of cases favorable and unfavorable to suppress the diffusion of Zn.

	Subcollector	Base and base contact	Emitter or emitter spacer
C+/B−/E−	Heavily-doped subcollector grown at 650 ^{o}C (N_D~1×10^{19} cm^{-3}) with 10 min growth interruption (GI)	Heavily-doped base contact grown at 650 ^{o}C with concentration beyond the saturation level	Lightly-doped (N_D~2×10^{17} cm^{-3}) emitter spacer grown at 650 ^{o}C
C−/B+/E−	Heavily-doped subcollector grown at 650 ^{o}C (N_D~2×10^{19} cm^{-3}) without GI	Heavily-dope base and base contact grown at 600 ^{o}C with concentration lower than the saturation level	Lightly-doped (N_D~2×10^{17} cm^{-3}) emitter spacer grown at 650 ^{o}C
C+/B−/E+	Heavily-doped subcollector grown at 650 ^{o}C (N_D~1.5×10^{19} cm^{-3}) with 20 min GI	Heavily-doped base and base contact grown at 650 ^{o}C beyond the saturation level	Highly-doped (N_D~5×10^{18} cm^{-3}) emitter grown at 650 ^{o}C
C+/B+/E+	Intermediately-doped subcollector grown at 650 ^{o}C (N_D~7×10^{18} cm^{-3}) with 10 min GI	Intermediate doped base grown at 600 ^{o}C with concentration lower than saturation level	Intermediately-doped (N_D~1×10^{18} cm^{-3}) emitter spacer grown at 650 ^{o}C

3.5.1 Zn diffusion in both directions

In Figure 3.20, the growth conditions for the LET of interest are close to the case of C+/B−/E−. The InP:Si^{+} subcollector was doped with donor concentration of N_D~1×10^{19} cm^{-3} (which is close to electron concentration, n) and was annealed for 10 min before the subsequent growth, which is a C+ condition. The nominal hole concentrations for the base and base contact are estimated to be p~2×10^{18} cm^{-3} and p~6×10^{18} cm^{-3}, respectively. Based on the results in the

doping and Hall-effect measurement calibration test for a thick $In(Al_{0.25}Ga_{0.75})As$:Zn layer grown under nominally same growth conditions, the molar flow rate of the precursor DEZn used for the base contact was above the saturation point, which leads to a B− condition. The DEZn dopant precursor flow rate vs. hole concentration in the growth of $In(Al_{0.25}Ga_{0.75})As$:Zn depending on growth temperature will be discussed later in detail. The doping level for the adjacent InP:Si^- emitter spacer is as low as N_D~2×10^{17} cm^{-3}, which is an E− condition. For the combined C+/B−/E− case, there will be a large amount of Zn interstitials generated in the base contact layer. As evidenced in Figure 3.20, Zn distribution shows a smeared concentration profile for base and base contact and also shows substantial presence of Zn in the unintentionally doped QW. In addition to diffusion of Zn in base/active region, Zn atoms diffuse out in both directions into the emitter and collector. In particular, Zn diffuses into the InP:Si^- emitter spacer layer and accumulates at the InP:Si/InP:Si^- interface where it possibly encounters a large electric field.

3.5.2 Zn diffusion forward into the emitter

Another HBT structure was grown to examine the effect of group III interstitials from the subcollector on the Zn movement in the base. In this structure, the InP:Si^+ subcollector was doped with N_D~2×10^{19} cm^{-3}. The InAlAs collector, InAlGaAs grading layer and base were grown right after the growth of subcollector without growth interruption; hence, it is a C− condition. The hole concentrations for the base and base contact are estimated to be p~2.5×10^{18} cm^{-3} and p~8×10^{18} cm^{-3}, respectively, similar to those used in the device epitaxial structure shown in Figure 3.20. However, the doping condition was carefully chosen so as to make DEZn flow as small as possible in order to minimize the formation of interstitial Zn during the growth, and hence, it can be considered as a B+ condition. The adjacent emitter spacer is also lightly

doped, which is an E− condition. The SIMS profile for the HBT grown under the combined C−/B+/E− condition is shown in Figure 3.21. Zn diffuses only into the emitter region and piles up at the InP:Si/InP:Si⁻ interface, which results in the shift of Zn profile toward the emitter – note that Zn profile drops "in" the InAlGaAs base layer on the collector side and it goes "beyond" the InAlGaAs base layer toward the emitter side. The unidirectional diffusion in this case is considered to be related to the directionality of the flux of group III interstitials from the subcollector. Since the interstitials flows towards the growth direction, there is a higher chance for a kicked-out Zn atom in the base to move forward rather than backward. The significant amount of interstitials causes the Zn-contained region to completely move towards the emitter.

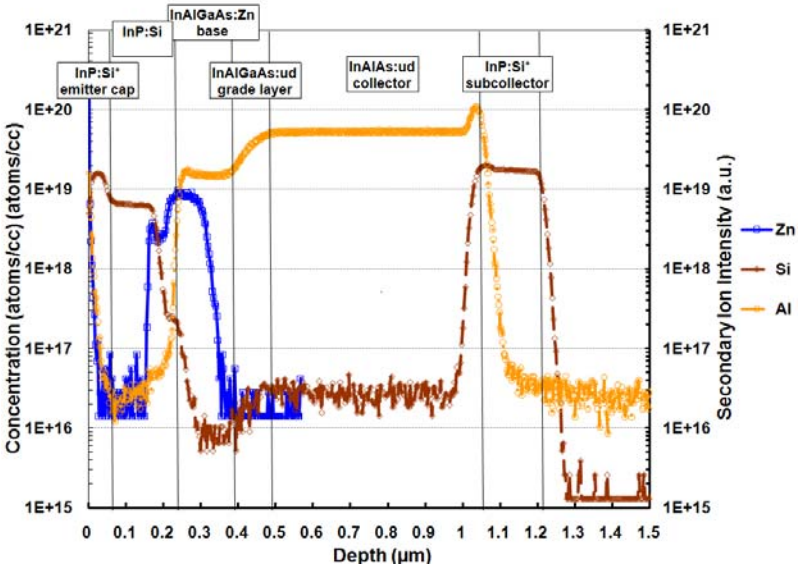

Figure 3.21: SIMS profile of an HBT structure grown under a C−/B+/E− condition.

3.5.3 Zn diffusion backward into the collector

As implied in the results shown in Figure 3.20 and 3.21, a high doping level in the emitter has an effect in blocking the Zn diffusion to a certain degree. The InP:Si⁻ emitter spacer layer in the structure shown in Figure 3.6 is removed in a new HBT structure to examine the high doping effect of adjacent emitter. In the structure, the InP emitter adjacent to the InAlGaAs base is

doped with N_D~5×10^{18} cm^{-3}, which is an E+ condition. A 20 min GI was introduced after the InP:Si^+ subcollector growth. To create the diffusion source, the whole base layer was Zn-doped to p~8×10^{18} cm^{-3}, and the DEZn flow was intentionally chosen to be above the saturation point. The growth conditions make the HBT a C+/B−/E+ case. The SIMS result is displayed in Figure 3.22. Clearly Zn diffusion is blocked by the highly-doped emitter layer, and it only diffuses into the graded In(Al_xGa_{1-x})As layer and InAlAs:ud collector layer. Note that Zn diffusion tail extends farther in the InAlAs collector layer than shown in Figure 3.20. The result confirms that the positively-charged Zn interstitials are subjected to junction blocking effect. However, the highly-doped InP layer is not enough to stop the Zn diffusion when the Zn interstitial concentration is extremely high. A test HBT was grown under a C−/B−/E+ condition, where Zn interstitials were generated by both mechanisms. As revealed by SIMS (not shown here), Zn still penetrates into the emitter layer about 20 nm, and brings about a Zn pile-up in the concentration profile. So the emitter blocking effect is only a preventive measure, with the first and second mechanisms associated with Zn interstitials being determinative.

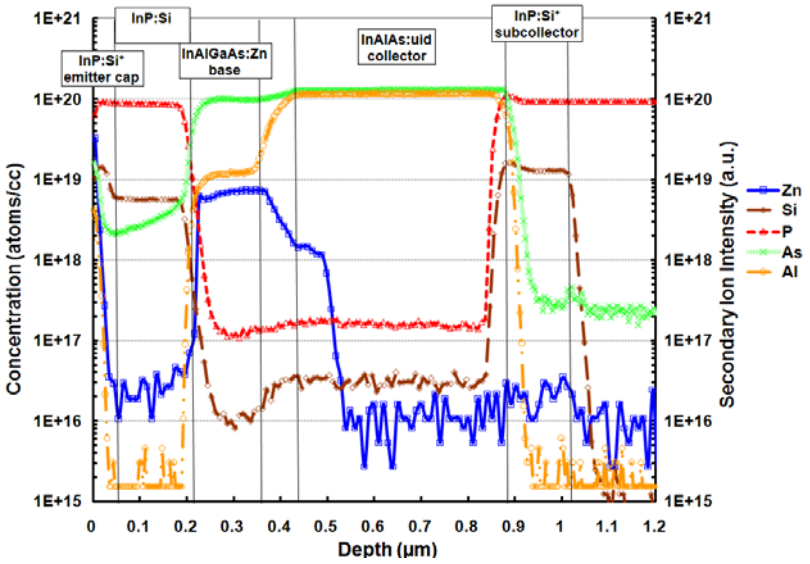

Figure 3.22: SIMS profile of an HBT structure grown under a C+/B-/E+ condition.

3.5.4 Suppression of Zn diffusion from the base

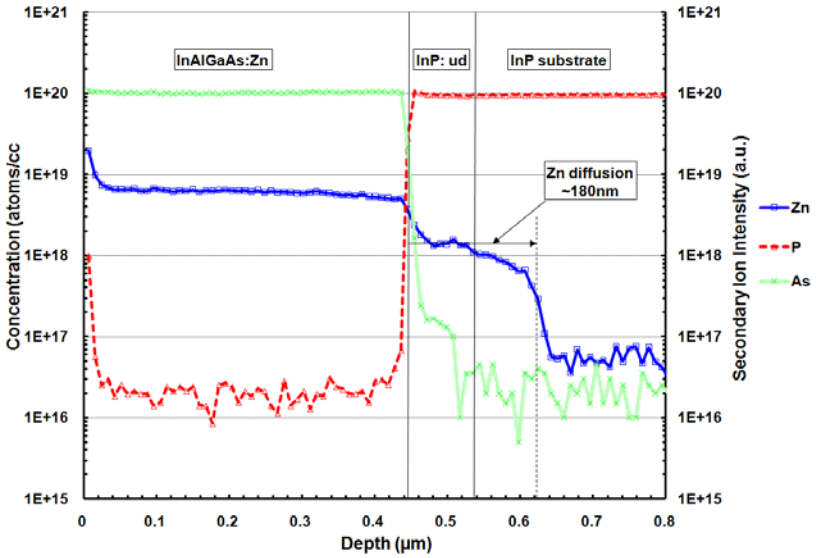

Figure 3.23: SIMS profile of a 450 nm In($Al_{0.25}Ga_{0.75}$)As layer doped with Zn at 650 ^{o}C with DEZn flow rate of 30 sccm.

The Zn interstitials generated during base doping could be a major source of Zn diffusion. Figure 3.23 shows the SIMS profile of a calibration In($Al_{0.25}Ga_{0.75}$)As layer doped with Zn at 650 ^{o}C with DEZn flow rate of 30 sccm. Zn back-diffusion into the undoped InP buffer and substrate is evident, suggesting the doping is saturated. The doping conditions should be carefully selected to keep away from the saturation point. A doping test in In($Al_{0.25}Ga_{0.75}$)As layers was carried out on semi-insulating InP substrates at 600 ^{o}C and 650 ^{o}C. All layers are ~400 nm thick. The result indicates a higher Zn doping efficiency at lower temperature, as shown in Figure 3.5 (b). The hole concentration level saturates at a DEZn flow of 8 sccm at 600 ^{o}C and 25 sccm at 650 ^{o}C. In addition, the saturated (maximum) hole concentration of InAlGaAs:Zn grown at 600 ^{o}C is significantly higher (~1.4×10^{19} cm^{-3}) than at 650 ^{o}C (~8×10^{18} cm^{-3}). This could be due to the difference in the incorporation of Zn ad-atoms induced by different sticking coefficient of Zn depending on growth temperatures. Since the maximum hole concentration is much higher at a lower temperature of 600 ^{o}C, in order to achieve a same hole

concentration, the DEZn flow used at 600 °C is more likely to stay away from its saturation point than the flow at 650 °C. Therefore, it is believed that more Zn atoms tend to reside in the substitutional sites as an active acceptor dopant in the case of Zn doping of InAlGaAs at 600 °C whereas more Zn atoms tend to occupy the interstitial sites, which will be prone to diffusion, in the case of Zn doping of InAlGaAs at 650 °C. In addition, lower growth temperature of InAlGaAs:Zn may be beneficial in suppressing Zn diffusion during the growth due to its reduced diffusivity at low temperatures.

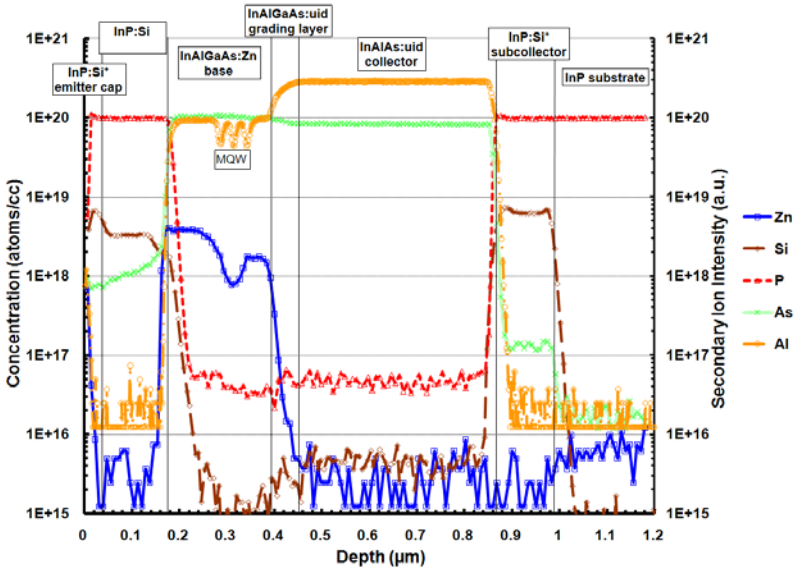

Figure 3.24: SIMS profile of an LET structure grown under a C+/B+/E+ condition.

An LET with multi quantum wells (MQWs) was grown by considering all these effects. The InP:Si^{+} subcollector was doped with N_D~7×10^{18} cm^{-3} at 650 °C and was annealed for 10 min before the subsequent growth of layers. The growth temperature was then lowered to 600 °C to perform the base growth. The nominal hole concentration levels for the base and base contact are p~2×10^{18} cm^{-3} and p~4×10^{18} cm^{-3}, respectively, which ensure the DEZn flows used in the study are far away from the saturation point, as implied from Figure 3.5 (b). The adjacent InP

emitter spacer was doped with N_D~1×10^{18} cm^{-3}. The growth conditions and structure design make the LET a C+/B+/E+ case. The corresponding SIMS profile is shown in Figure 3.24. Zn atoms do not diffuse substantially into the emitter or into the collector and abrupt junctions are achieved in this LET structure. In addition, the dip of Zn profile in the undoped InGaAs/InAlGaAs MQW region is also observed.

To summarize this part, a model was developed to explain the Zn diffusion behaviors in InAlGaAs/InP HBT and LET structures. Three mechanisms that are related to the growth conditions and doping levels of the subcollector, base, and emitter are identified. Growth interruption after InP subcollector growth or a relatively low Si doping level during the growth of subcollector (C+), a low growth temperature for the Zn doping of the InAlGaAs base region (B+), and a relatively high Si-doping in the InP emitter layer (E+) are regarded as the favorable conditions (C+/B+/E+) for the suppression of Zn diffusion. On the contrary, a high doping in subcollector without thermal annealing (C−), a DEZn flow used in the base doping that is close to or above the saturation point (B−), and a low Si-doping level in the emitter or emitter spacer (E−) are considered as the conditions (C−/B−/E−) to induce Zn diffusion. Specifically, a C+/B−/E− condition results in Zn diffusion into both sides; a C−/B+E− condition results in Zn diffusion only into the emitter side; and a C+/B−/E+ condition results in Zn diffusion only into the collector side.

3.5.5 Detrimental effects of Zn diffusion

There are two main concerns regarding the high diffusivity of Zn in the LET and TL devices. The first is that Zn may diffuse into the emitter region and block the minority carrier injection by creating a potential barrier in the conduction band, which leads to poor electrical

performance [73]. This problem can be alleviated to a certain degree by Zn diffusion engineering as reported in InP-based HBTs employing Zn dopant in the base [68,74]. Figure 3.25 (a) shows the BE junction *I-V* curves for LETs with and without Zn diffusion revealed by SIMS measurement. The turn-on voltages (defined as the voltage where the current reaches 1×10^{-8} A) are 0.64 and 0.52 V for the Zn-diffused LET and the diffusion-suppressed LET, respectively, indicating the presence of a potential spike at the junction due to Zn diffusion. This is more clear in Figure 3.25 (b), where the HBT with Zn diffusion definitely shows a higher turn-on voltage than HBT without Zn diffusion from the measured family curves. The displaced junction will lower the electron injection efficiency from the emitter and degrade the transistor performance.

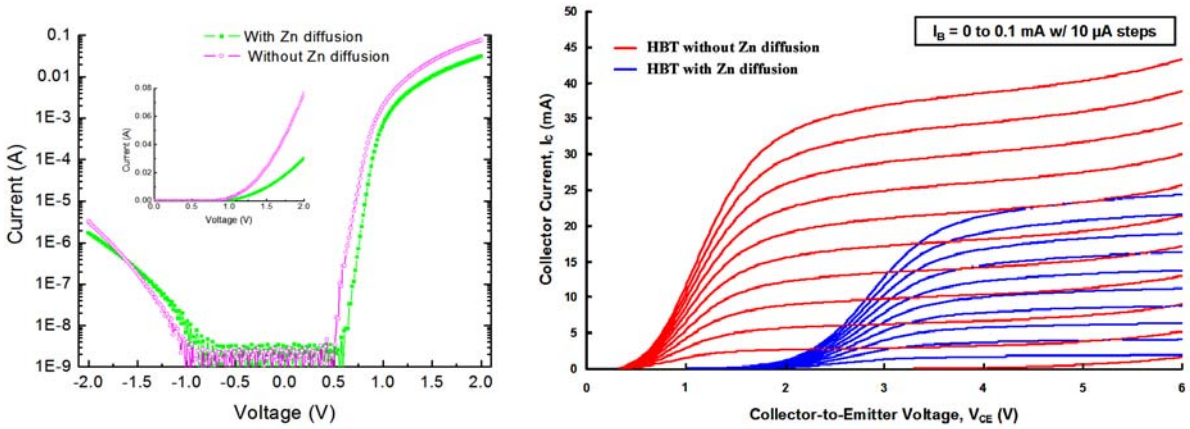

Figure 3.25: (a) BE junction *I-V* curves for the LETs with and without Zn diffusion. Inset is plotted in linear scale; (b) Family curves for HBTs with and without Zn diffusion.

The second concern about Zn-diffusion is that Zn may diffuse into the undoped QWs of the base/active region in the LETs or TLs and degrade the optical quality by creating non-radiative recombination centers [75]. This problem may be more serious in the LET and TL structure where Zn-doped layers are located very closely on both sides of the undoped QWs and not to be engineered easily by the method used in the InP-based HBTs having Zn-doped layer. To shed

light on this effect, we investigated the PL of the InGaAs/InAlGaAs:Zn SQW with different Zn doping level in the barrier layers, as shown in Figure 3.26. The doping levels in the barriers are undoped, 2×10^{18}, and 8×10^{18} cm^{-3} for (a), (b) and (c), respectively (as measured by Hall effect on similar samples), while the InGaAs SQW was undoped. The PL efficiency deteriorates drastically as the doping level increases. These results present direct evidence that the diffusion of Zn degrades the optical quality of the active layer, especially at high doping levels.

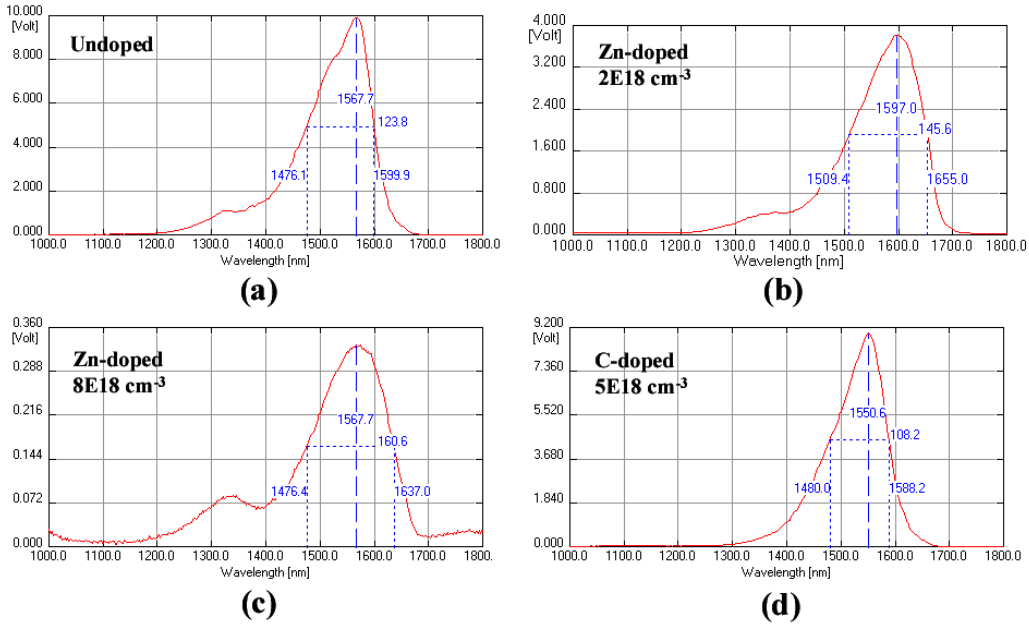

Figure 3.26: PL spectra for the InGaAs/InAlGaAs SQW structure with (a) undoped barriers, (b) InAlGaAs:Zn barriers, $p=2\times10^{18}$ cm^{-3}, (c) InAlGaAs:Zn barriers, $p=8\times10^{18}$ cm^{-3}, and (d) InAlGaAs:C barriers, $p=5\times10^{18}$ cm^{-3}.

To conclude here, although Zn can be contained only in the base region through proper engineering of growth conditions and doping, Zn will inevitably diffuse into active region and plague the QW due to the proximity of QW to the highly-doped layers, which certainly leads to compromised performances of LETs and TLs. To eliminate the dopant diffusion issue and improve the optical performance, another *p*-type dopant, carbon, was studied in detail in the next chapter.

CHAPTER 4

Growth and Performance of LETs and TLs with C-Doped Base

4.1 Doping Behaviors and Material Properties in InAlGaAs:C Alloys

C is known to have low thermal diffusivity and high solubility in GaAs, enabling sharp doping profile at high doping levels [76,77]. Growth of C-doped InGaAs was proved to be feasible and successful [78], and now it has been routinely adopted as the base dopant for high performance InP/InGaAs HBTs [7]. However, C doping for *p*-type conductivity in InGaAs and InAlGaAs materials with high In content is more challenging than one in GaAs and AlGaAs materials. One underlying reason is that the weak In-C bond causes the doping to be amphoteric, which means C may replace anions as well as cations. The atomic bonds of interest with strength going from weak to strong are in the following order: In-C < As-C < Ga-C < Al-C [79,80]. Note that In-C bond is even weaker than the As-C bond. To make a *p*-type doping, C has to occupy the As site, which is easily performed in GaAs due to a strong Ga-C bond. When C doping is performed in InGaAs, C tends to occupy In site to form an As-C bond instead of an In-C bond because of the bond strength difference. In this case, it acts as a donor and compensates the overall hole level. For low indium composition in $In_xGa_{1-x}As$ alloy, *p*-type doping was achieved including at x=0.53 [78]. For x>0.6, only *n*-type conductivity was obtained [80]. Another issue is the strong etching effect during growth due to the use of halides. Carbon halides such as CCl_4 and CBr_4 are the normally-used C dopants in MOCVD [81], while halides and halogens have been widely adopted as the etching gasses for compound semiconductors in devices fabrication. Indium halides, in particular, are highly volatile. This leads to significant reduction in growth rate and large variation in alloy composition as compared to the growth

without doping [82-84]. In addition, it was observed that Al precursors react strongly with CBr_4 in the gas phase due to strong Al-C bonds [85]. The reaction rates of In, Ga, and Al in the gas phase and the removal rates of In, Ga, and Al from the surface are so different that the growth of the C-doped alloys especially quaternary InAlGaAs suffers from a poor within-wafer uniformity and run-to-run reproducibility.

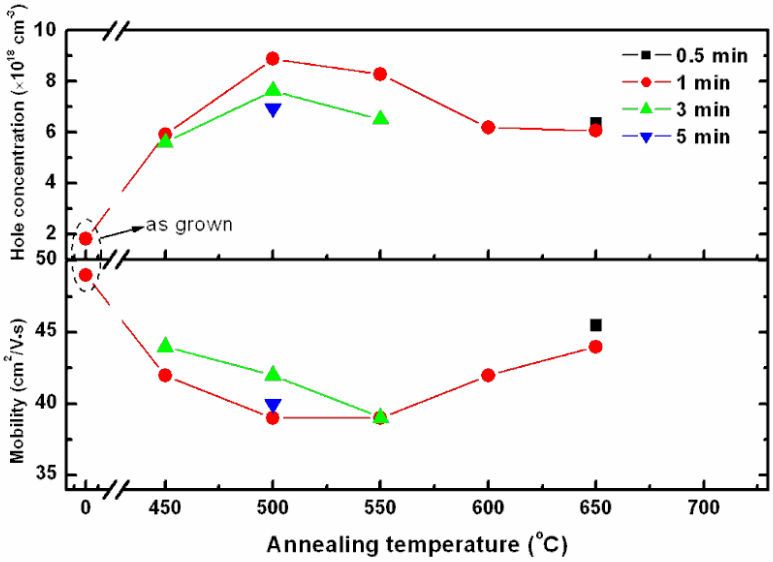

Figure 4.1: Hole concentration (upper) and mobility (lower) in $In(Al_{0.4}Ga_{0.6})As$ as a function of annealing temperature for different duration.

Despite all these challenges, optimization of C doping in $In(Al_xGa_{1-x})As$ layers using CBr_4 was carried out on InP substrates. A relatively low temperature (less than 600 ^oC) and low V/III ratio (~5) were used in order to permit the sticking of carbon atoms on the growing surface and to incorporate C onto As lattice sites. To dissociate the C-H bonds that form during growth and to reactivate the C acceptors [78], post annealing is necessary and an annealing test was first performed to identify the optimal annealing condition. Figure 4.1 displays the hole concentration (upper panel) and mobility (lower panel) in $In(Al_{0.4}Ga_{0.6})As$ as a function of annealing temperature for different duration in N_2 ambient. The 400-nm sample was grown at

570 °C with a V/III ratio of 5. The electrical properties were obtained by room-temperature Hall measurement. It is found that a short post-annealing leads to increased hole concentration and the highest value is obtained at 500 °C for 1 min. This annealing condition has been adopted for all the C-doped samples thereafter. The mobility is in the range of 38~50 $cm^2/V{\cdot}s$, which is smaller than those in Zn-doped InAlGaAs layers.

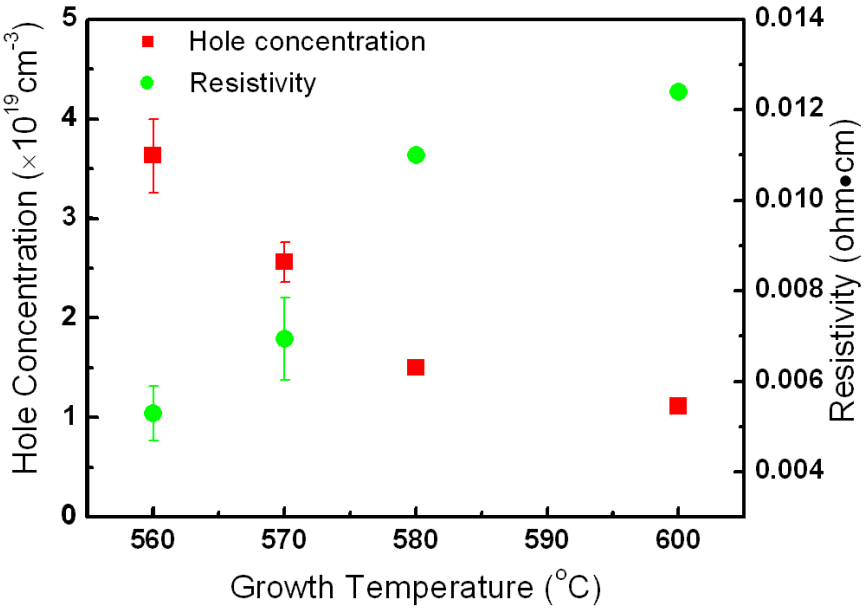

Figure 4.2: Hole concentration (□) and resistivity (○) as a function of growth temperature.

The growth rate was generally reduced by half for the same TMIn flows, from 0.2 nm/s to 0.1 nm/s, due to the etching effect of CBr_4. The surface of the InAlGaAs:C samples are specular and smooth under Nomarski optical microscope. The dependence of hole concentration and resistivity on the growth temperature in $In(Al_{0.4}Ga_{0.6})As$ is displayed in Figure 4.2 for the same V/III ratio (~5) and same CBr_4 flow rate (95 sccm). It is evident that a lower growth temperature allows for a higher hole level. Using the conditions at 570 °C, we are able to attain a free hole concentration as high as p~2.6×10^{19} cm^{-3} and a sheet resistance as low as 350 Ω/□ for a 200-nm-thick $In(Al_{0.4}Ga_{0.6})As$ layer. As indicated by AFM shown in Figure 4.3 (a), the root mean square

(RMS) roughness is 0.392 nm for 5×5 μm^2 scan area, which is considered quite acceptable for devices in view of the relatively large thickness, the low growth temperature, and the high doing. At lower growth temperatures, surface morphology deteriorates rapidly.

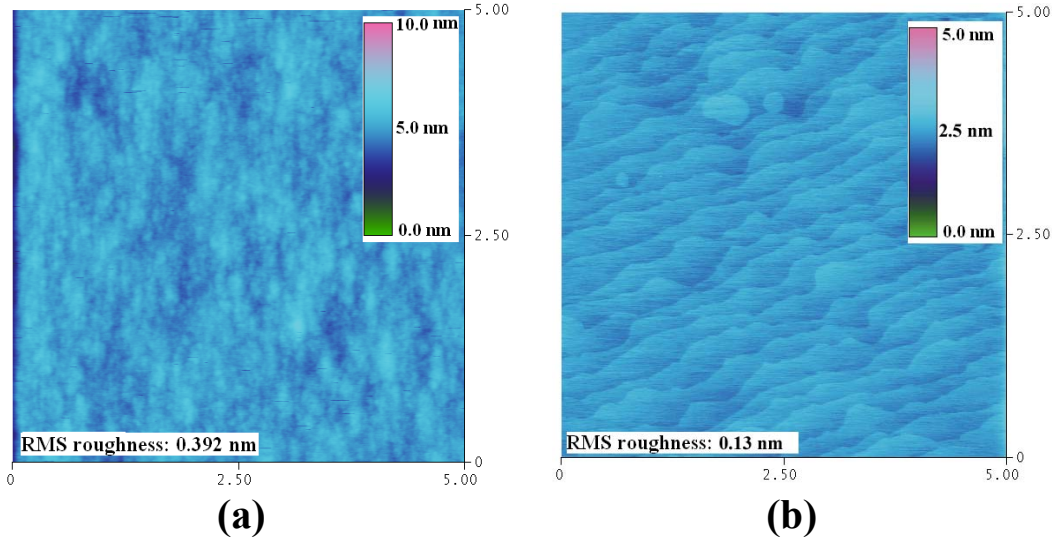

Figure 4.3: AFM images for (a) a C-doped InAlGaAs single layer and (b) a C-doped LET..

A SQW structure with C-doped barriers was grown for comparison to those with Zn-doped barriers. The barrier doping level is 5×10^{18} cm^{-3} and the PL spectrum is shown in Figure 3.26 (d). The PL peak intensity of the SQW structure with C-doped QW barriers is much higher than those with Zn-doped QW barriers and the peak linewidth is narrower, indicating significantly improved PL efficiency due to low diffusivity of dopants.

One of the drawbacks in C-doping is the degradation of material quality due to the use of low V/III ratio and low temperature as compared to the Zn-doped materials. Figure 4.4 (a) shows the PL spectra for the C- and Zn-doped $In(Al_{0.25}Ga_{0.75})As$ bulk materials doped to 2×10^{18} cm^{-3}. It is clear that the NBE PL intensity for the C-doped $In(Al_{0.25}Ga_{0.75})As$ is almost ten times weaker than for the Zn-doped one of the same doping concentration and thickness. For the same doping concentration, the PL efficiency is a measure of the effective minority carrier lifetime,

which is generally non-radiative in nature at room temperature [86]. Thus, the effective carrier lifetime is much shorter in C-doped InAlGaAs materials. This is directly confirmed by the time-resolved PL measurement as indicated in Figure 4.4 (b) for these samples. From the single exponential decay it is clear that the Zn-doped $In(Al_{0.25}Ga_{0.75})As$ has a longer minority electron lifetime, with a lifetime determined to be 206 ps in contrast to 110 ps in the C-doped material. In the $In(Al_{0.4}Ga_{0.6})As$:C layer doped to 8×10^{18} cm^{-3}, the lifetime is as short as 88 ps. This is possibly due to the low growth temperature and low V/III ratio required for C-doping, which introduces a substantial amount of defects in the layer. Similar results have been observed in Zn- and C-doped InGaAs as well as GaAs layers grown by MOCVD [87-90]. The amphoteric nature of C-doping and post annealing of the C-doped materials for *p*-type activation may also account for the defect production and lifetime diminishing [91-93]. As the bulk recombination current dominates the base current, the current gain of a transistor can be written as $\beta=\tau_B/\tau_t$, where τ_B is the minority recombination lifetime and τ_t is the transit time [73]. A shorter minority carrier lifetime leads to a smaller electrical gain accordingly.

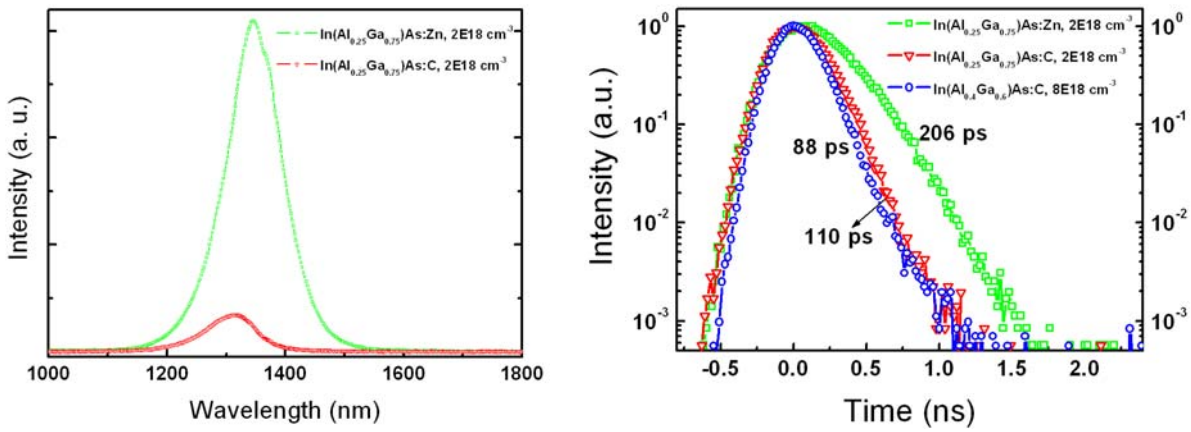

Figure 4.4: (a) PL spectra for the C-doped $In(Al_{0.25}Ga_{0.75})As$ and Zn-doped $In(Al_{0.25}Ga_{0.75})As$; (b) TRPL for the C-doped and Zn-doped InAlGaAs layers.

4.2 Performance of C-doped LETs

An LET structure with a C-doped base was grown after calibration of the C-doped layer. The structure is similar to that shown in Figure 3.6 except that the base contact layer was removed and a single doping level of 8×10^{18} cm^{-3} was employed in the base. AFM image on the epitaxial wafer is shown in Figure 4.3 (b). Smooth surface with step flows was observed in contrast to the InAlGaAs:C layer in Figure 4.3 (a), indicating a "healing effect" of InP growth on the morphology of the underlying layer. SIMS measurement on this structure indicates that C does not diffuse into either the emitter or the QW active region, as evidenced in Figure 4.5. The QW profile is clearly revealed by the traces of C and Al and the doping profile at the emitter/base interface is abrupt.

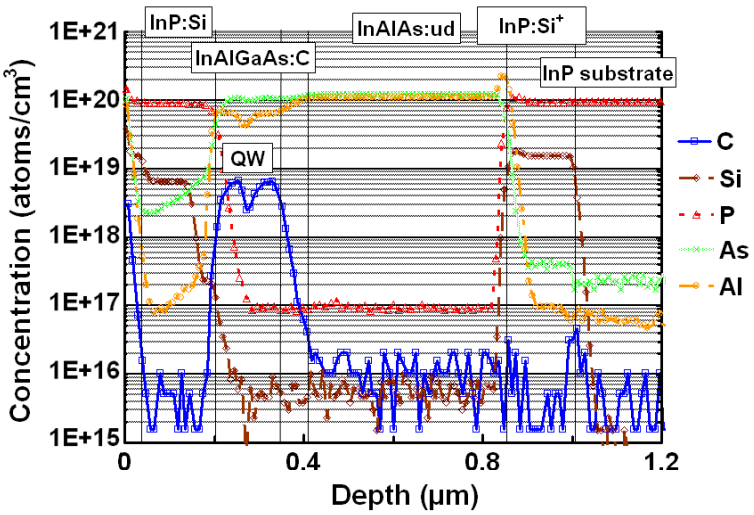

Figure 4.5: SIMS profile of the C-doped LET.

After fabrication of this wafer into LETs with an emitter area of 120×120 μm^2, the EL spectra of the LET taken at different I_B are displayed in Figure 4.6 (a). V_{CE} was fixed at 2 V during the measurement. The emission wavelength of the LET is centered at ~1610 nm and slightly blue-shifts with I_B (0.2 nm/mA) due to a band-filing effect. The origin of the rising shoulder at 1490 nm is unknown yet, possibly from the excited states of the QW or defect level

of the C-doped base. The L-I_B curve with V_{CB}=0 V was displayed in Figure 4.6 (b), showing significant improvement as compared to the LETs with Zn-doped bases. The C-doped SQW LET exhibits approximately a twofold increase of the output power in comparison with that of the Zn-doped MQW LET for the same bias conditions. The saturation of the output power is attributed to the device heating or Auger recombination.

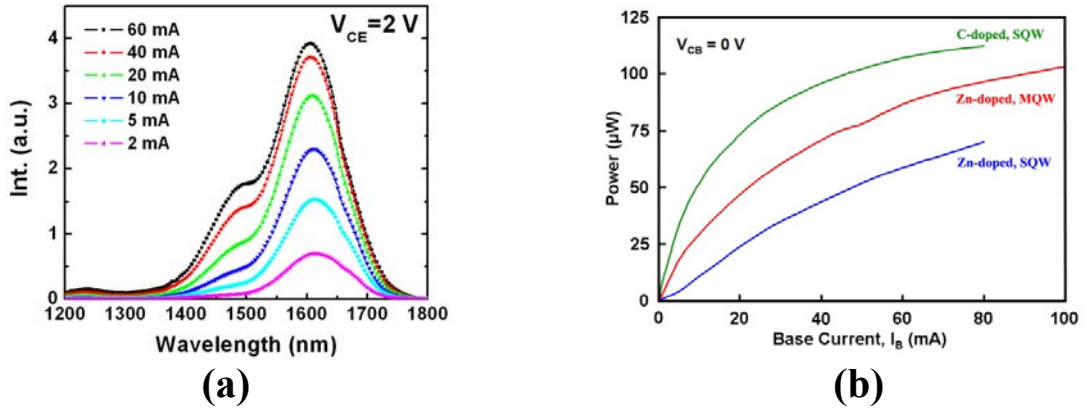

Figure 4.6: (a) EL output spectra taken at different I_B; (b) EL peak output power as a function of I_B for the C-doped and Zn-doped LETs.

The BE junction I-V curve was also measured and compared to those for Zn-doped LETs, as shown in Figure 4.7. The C-doped BE junction exhibits a similar turn-on characteristics as in the diffusion-suppressed Zn-doped BE junction and a lower leakage current. Both the high light output of the LET and the low turn-on voltage of BE junction verify the low diffusivity of C.

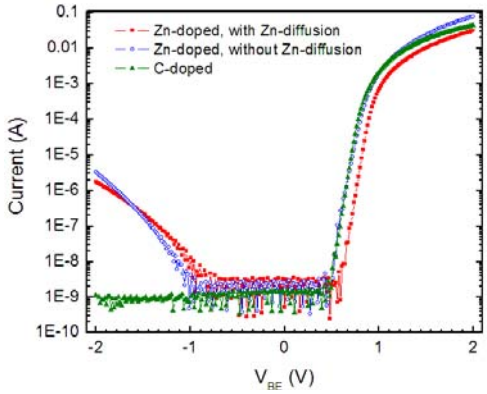

Figure 4.7: BE junction I-V curves for the C-doped LET and Zn-doped LETs with and without Zn diffusion.

Figure 4.8 shows the transistor family curves for the C-doped SQW LET in (a) and the diffusion-suppressed Zn-doped SQW LET (as shown in Figure 3.9 (a)) in (b). The C-doped LET has a low DC current gain of only 0.22 in sharp contrast to the current gain of 45 in the Zn-doped LET. Figure 4.9 illustrates the Gummel plot of the C-doped LET under V_{CB} of 0 V. The ideality factor n of I_B is 1.17 over a wide range of currents, indicating that the bulk recombination current dominates the base current even at low current levels. Shown in the inset is β as a function of I_C. β remains almost constant within the investigated current levels, in contrast to the gain increasing and subsequent flattening with I_C in conventional HBTs [6].

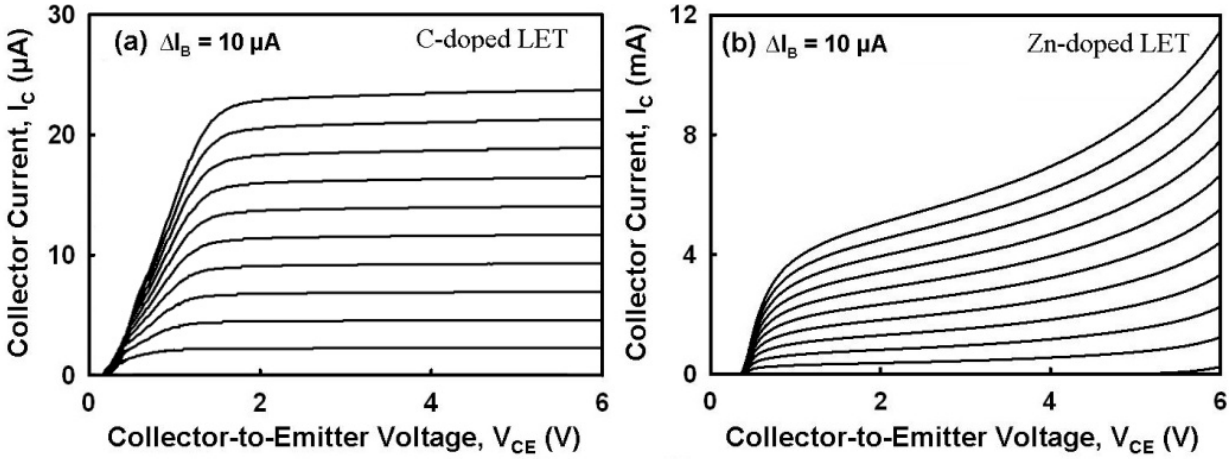

Figure 4.8: Family curves for (a) the C-doped LET and (b) the Zn-doped LET.

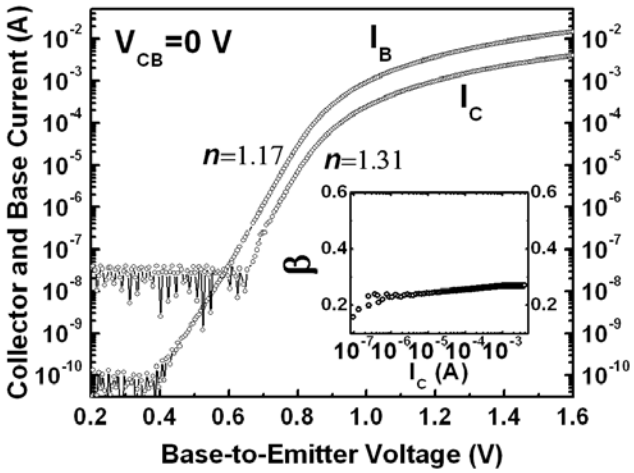

Figure 4.9: Gummel plot of the C-doped LET. The inset shows current gain vs. collector current.

The low current gain in the C-doped LET suggests a large number of carriers recombined in the QW. During the operation of an LET, when the electrons diffuse across the base, they are collected either at the QWs (as an optical collector) or at the BC junction (as an electrical collector) neglecting other current components. Thus, the two collectors are competing against each other and an LET could swing from being more HBT-like to more LED-like, depending on which collector consumes more electrons. To better understand the device physics, we introduce a couple of parameters other than β to describe the functionality of an LET. The common-base current gain (α), which accounts for the portion of electrons collected at the electrical collector, is expressed as:

$$\alpha = \frac{I_C}{I_E} = \frac{\beta}{1+\beta}. \tag{4.1}$$

On the other hand, the injection efficiency (η_{in}) or capture efficiency of the LET from the perspective an LED, which accounts for the portion of electrons collected at the optical collector, will be:

$$\eta_{in} = \frac{I_B}{I_E} = \frac{1}{1+\beta}. \tag{4.2}$$

The external quantum efficiency (η_e) is related to η_{in} through the expression of:

$$\eta_e = \eta_{in}\eta_i\eta_{ex}, \tag{4.3}$$

where η_i is the internal quantum efficiency and η_{ex} is the extraction efficiency. One can easily tell that in a normal HBT α is close to unity while in a normal LED η_{in} is close to unity. By plugging β, α is calculated to be 98% in the Zn-doped LET meaning most of the carriers being collected by the BC junction while η_{in} is calculated to be 82% in the C-doped LET meaning most

of the carriers being collected at the QW. Figure 4.10 is an illustrative representation of the carrier collection in the Zn-doped and C-doped LETs. It is clear that the Zn-doped LET is more like an HBT and the C-doped LET is more like an LED.

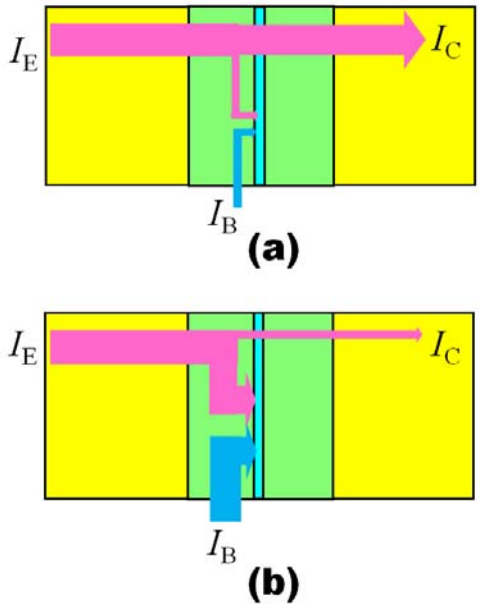

Figure 4.10: Carrier collection in (a) the Zn-doped LET and (b) the C-doped LET.

Compared to normal LEDs, LETs are unique devices that are capable of separating η_{in} from η_i thanks to its three-terminal operation. The EL output as a function of I_E for both LETs is plotted in Figure 4.11. The light output from the C-doped LET is significantly higher than that from the Zn-doped LET for a given injection current due to a high η_{in} of 82% in the C-doped LET as compared to that of only 2% in Zn-doped LET. In addition, as shown in Figure 4.6 (b), for the same I_B the C-doped LET converts more photons as well, which suggests a higher η_i than that in the Zn-doped LET due to the low diffusivity of C. Therefore, the high η_{in} and high η_i enable the C-doped LET to function like an LED, while the high α and high β enable the Zn-doped LET to function like an HBT. The distinctive difference in the current gain will be analyzed using a charge control model.

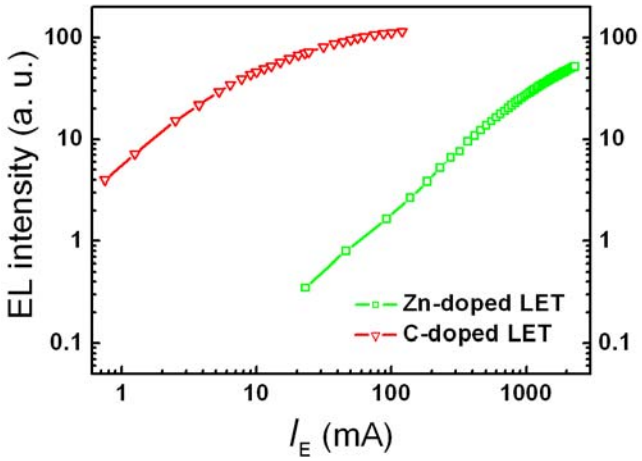

Figure 4.11: Light output as a function of the emitter current for the Zn- and C-doped LETs.

During the investigation of LETs, the collector consisting of grading InAlGaAs and InAlAs was replaced by an undoped InP layer to check its effect on the electrical performance. A 20 nm InAlAs:Si layer is inserted between the undoped 300-nm InP collector and the highly-doped InP subcollector as an etch stop. Figure 4.12 shows the family curves for the LETs with an InAlAs collector or an InP collector. The double heterostructure (DH) LET shows a better turn-on characteristics with low turn-on voltage and small on-resistance in contrast to the slow turn-on in LET with an InAlAs collector, indicating a possible potential barrier in the grading layer. The DH structure also offers the advantage of easier growth and will be adopted in the TL designs.

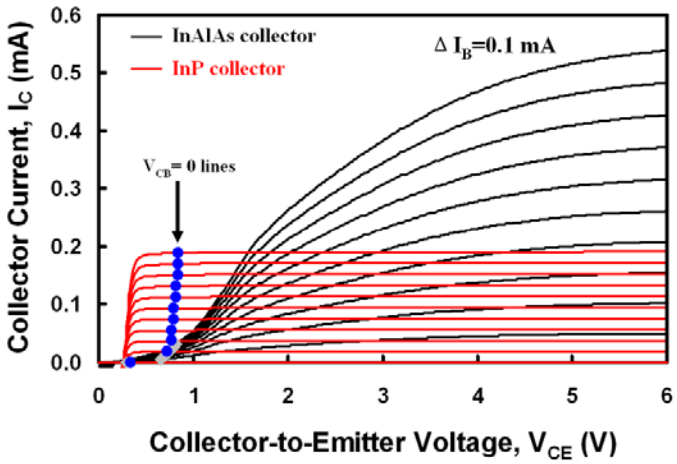

Figure 4.12: Family curves for the LETs with an InAlAs collector or an InP collector.

4.3 Charge Control Analysis in HBTs and LETs

We have also compared the electrical performance of a C-doped HBT to the Zn-doped HBT. The C-doped LET has a similar structure to the LET except for the insertion of the QW. The family curves for both devices are displayed in Figure 4.13. The current gain in the C-doped HBT is 12 in contrast to 220 in the Zn-doped HBT due to the shorter minority carrier lifetime in the base, as indicated in Figure 4.4 (b).

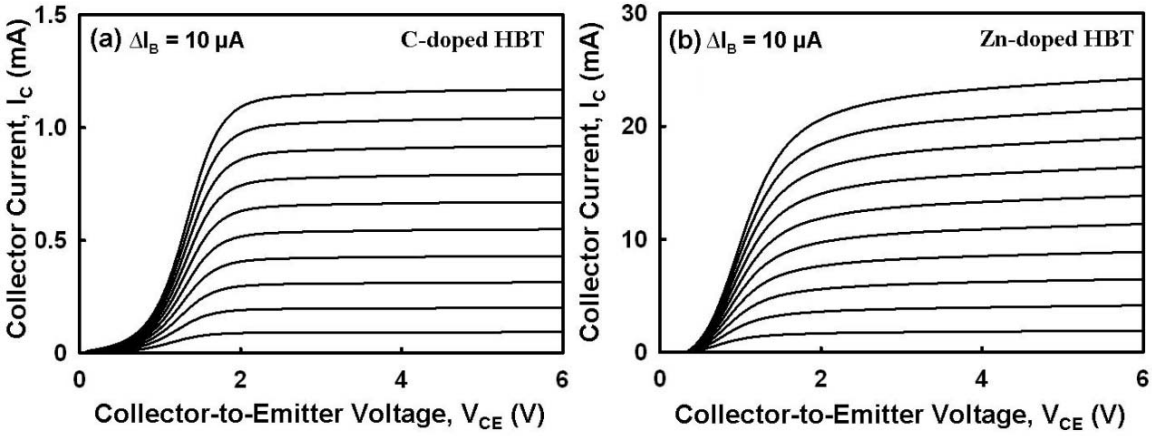

Figure 4.13: Family curves for (a) the C-doped LET and (b) the Zn-doped LET.

The DC and AC characteristics of a transistor are often analyzed by charge control model, in which charge is stored in the junctions and base region of the device and increased or decreased when the bias conditions are changed. In the DC analysis, assuming minority charge stored in the base region is Q, the collector current I_C can be expressed as [6,73]:

$$I_C = \frac{Q}{\tau_t} = \frac{2D_n Q}{W^2}, \tag{4.4}$$

where D_n is the diffusion constant and W is the base thickness. Assuming the base recombination current is the dominant current component, the base current is expressed as:

$$I_B = \frac{Q}{\tau_B}. \tag{4.5}$$

Then the current gain β is:

$$\beta = \frac{I_C}{I_B} = \frac{\tau_B}{\tau_t} = \frac{2D_n \tau_B}{W^2}. \quad (4.6)$$

Plugging all the parameters, β for the Zn-doped and C-doped HBTs is calculated to be 206 and 20, respectively, very close to the measured values. The parameters used in the calculation are summarized in Table 4.1.

Table 4.1: Parameters used in the calculation of current gains in HBTs.

Devices	Doping (cm^{-3})	W (nm)	D_n (cm^2/s)	τ_B (ps)	$\beta_{cal.}$	$\beta_{mea.}$
Zn-doped HBT	2×10^{18}	100	50	206	206	220
C-doped HBT	8×10^{18}	132	20	88	20	12

Figure 4.14 (a) shows the dependence of HBTs' and LETs' current gain on the I_C derived from the Gummel plot. Note the current gain from the Gummel plot is smaller than deduced from the family curves. It is evident that the Zn-doped devices have a current gain about one order of magnitude larger than that in the corresponding C-doped devices. In order to boost the current gain, HBTs with different base thickness have been grown and fabricated. Figure 4.14 (b) is a plot of current gain against base thickness. The C-doped HBTs show increased β with decreasing W following Equation 4.6, but it is hardly comparable to that in the Zn-doped HBTs.

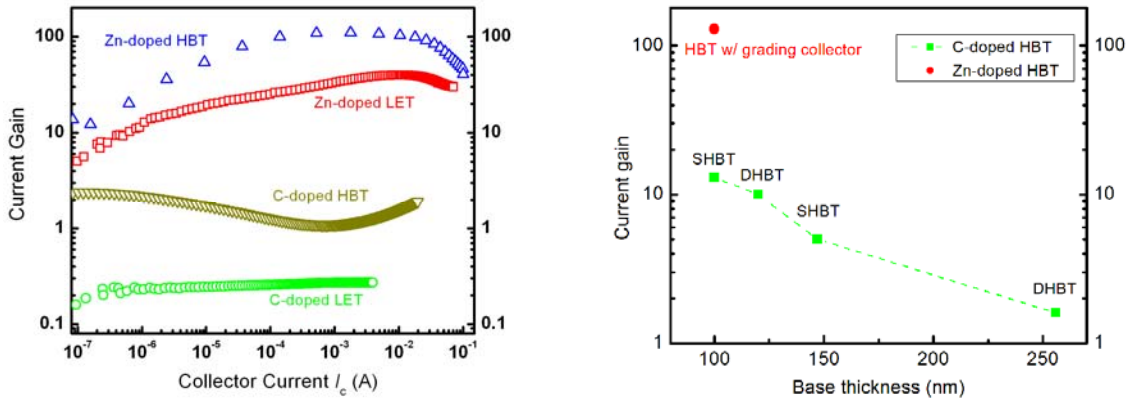

(a) **(b)**

Figure 4.14: (a) β vs. I_C in LETs and HBTs; (b) β vs. W in HBTs.

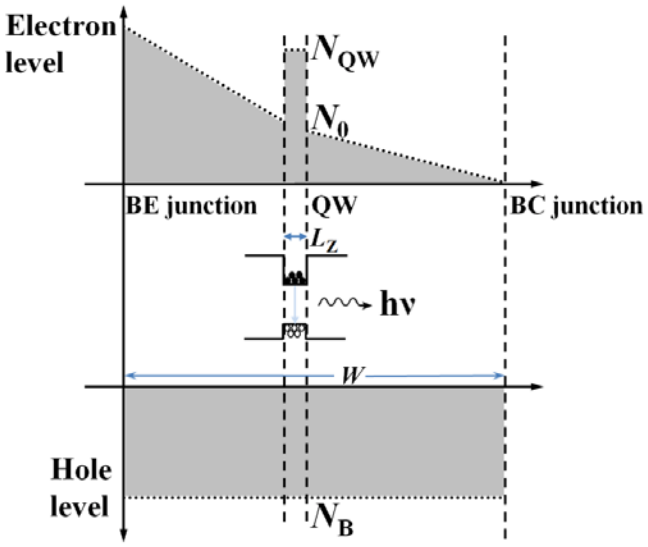

Figure 4.15: Schematic representation of the carrier distribution in the base region of an LET.

The current gain in the Zn- and C-doped LETs is more distinctive, which can't be simply attributed to the difference in the minority carrier lifetime. To get an insight into this issue, a charge control analysis was performed for a generic expression of the current gain in an LET. Figure 4.15 depicts schematically the carrier distribution profile in the base region of an LET in forward active mode. The hole level in the base is virtually fixed at the base doping level while electron density goes down at a linear gradient from BE junction to BC junction. When electrons injected from the BE junction diffuse across the QW, a fraction of them is captured into the two-dimensional (2D) bound states in the QW via local capture process, which forms a 2D carrier density of N_{QW}. The average unbounded (3D) carrier density around the QW is N_0. N_{QW} is related to N_0 through the expression of [94]:

$$\frac{dN_{\mathrm{QW}}}{dt} = \frac{N_0}{\tau_{\mathrm{cap}}} - \frac{N_{\mathrm{QW}}}{\tau_{\mathrm{r}}} - \frac{N_{\mathrm{QW}}}{\tau_{\mathrm{esc}}}, \tag{4.7}$$

where τ_{cap} is the QW capture lifetime, τ_{r} is the recombination lifetime in the QW, and τ_{esc} is the carrier thermionic escape time. As τ_{r} is much larger than τ_{esc} [33,94], at steady state we have:

$$N_{\mathrm{QW}} \cong \frac{\tau_{\mathrm{esc}}}{\tau_{\mathrm{cap}}} N_0. \tag{4.8}$$

And the recombination current at the QW (I_{QW}) that accounts for the net current flowing into the QW is:

$$I_{\mathrm{QW}} = \frac{A_{\mathrm{E}} q L_{\mathrm{Z}} N_{\mathrm{QW}}}{\tau_{\mathrm{r}}} = \frac{A_{\mathrm{E}} q L_{\mathrm{Z}}}{\tau_{\mathrm{r}}} \cdot \frac{\tau_{\mathrm{esc}}}{\tau_{\mathrm{cap}}} N_0, \tag{4.9}$$

where A_{E} is the emitter size, q is the electron charge, and L_{Z} is the QW width. Assuming the unbounded carrier concentration varies linearly with distance in the base and the QW is placed right in the middle, the collector current I_{C} is calculated to be [6]:

$$I_{\mathrm{C}} = A_{\mathrm{E}} q D_{\mathrm{n}} \frac{2N_0}{W}. \tag{4.10}$$

Since the recombination current dominates the base current I_{B}, neglecting other base current components, the current gain β of the LET is obtained as:

$$\beta = \frac{I_{\mathrm{C}}}{I_{\mathrm{B}}} = \frac{I_{\mathrm{C}}}{I_{\mathrm{QW}}} = \frac{2D_{\mathrm{n}}\tau_{\mathrm{r}}}{\frac{\tau_{\mathrm{esc}}}{\tau_{\mathrm{cap}}} L_{\mathrm{Z}} W}, \tag{4.11}$$

which is only dependent on the structural parameters. In this expression, the physical meaning of parameter $\frac{\tau_{\mathrm{esc}}}{\tau_{\mathrm{cap}}}$ is the quantum capture efficiency of the QW, which needs to be determined. τ_{r} can be estimated from the base doping level N_{B} [6]:

$$\frac{1}{\tau_{\mathrm{r}}} = A + BN_{\mathrm{B}} + CN_{\mathrm{B}}^2, \tag{4.12}$$

where A is the nonradiative recombination coefficient related to the local defects, which can be neglected in high-quality materials [95], B is the radiative recombination coefficient, and C is the

Auger recombination coefficient. B and C are assumed to be 1×10^{-10} cm^3/s and 5×10^{-29} cm^6/s, respectively in InAlGaAs alloys [9595,96].

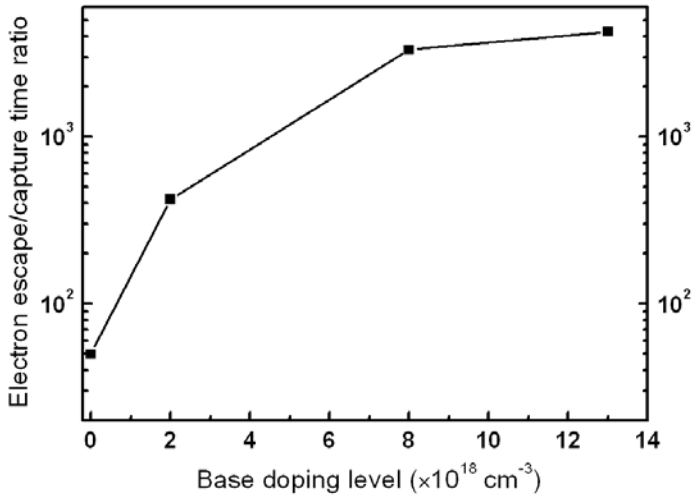

Figure 4.16: τ_{esc}/τ_{cap} as a function of base doping level.

By plugging all the parameters in Equation 4.11, it is found that $\frac{\tau_{esc}}{\tau_{cap}}$ is a strong function of doping level N_B, as indicated in Figure 4.16. The value in the undoped case is also added at N_B of zero for reference [94]. With the increase of N_B, $\frac{\tau_{esc}}{\tau_{cap}}$ increases so does the quantum capture efficiency of the QW. The parameters used in the calculation are summarized in Table 4.2 for the Zn- and C-doped LETs.

Table 4.2: Parameters used in the calculation of current gains in LETs.

Devices	N_B (cm^{-3})	W (nm)	L_Z (nm)	D_n (cm^2/s)	τ_r (ps)	β	τ_{esc}/τ_{cap}
Zn-doped LET	2×10^{18}	100	12	50	2500	45	421
C-doped LET	8×10^{18}	100	12	20	250	0.22	3330

The correlation between the quantum capture efficiency ($\frac{\tau_{esc}}{\tau_{cap}}$) and the doping level is considered to originate from the Coulomb field in the QW region, set up by the mutual attraction of electrons and holes. When electrons diffuse across the QW, a stronger Coulomb field in the

C-doped LET with heavier base doping enhances the relaxation of electrons and facilitates the local quantum capture process of unbound electrons to the bounded states in the QW, which leads to an increase of the bounded electron density as from Equation 4.8. In addition, these bounded electrons are subjected to faster recombination in the C-doped device because of the higher base level and shorter carrier lifetime as from Equation 4.9 and 4.12. The combined effects result in a significant enhanced base current and a small current gain in the C-doped LET, which renders it more like an LED.

4.4 Design and Performance of C-doped TLs

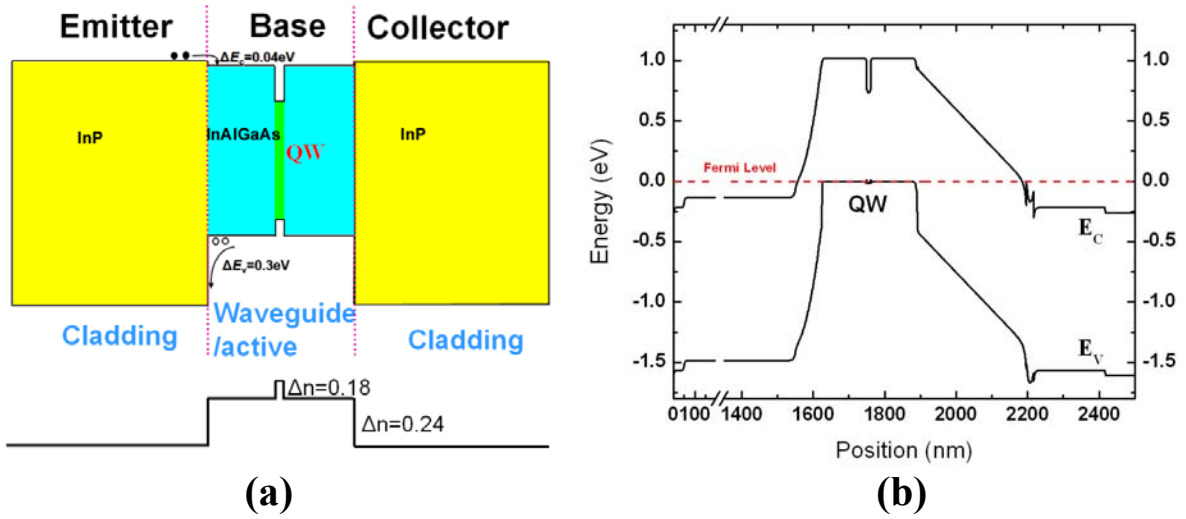

Figure 4.17: (a) Schematic representation of band structure and refractive index profile of the TL epitaxial structure; (b) Calculated equilibrium band diagram.

The C-doped LETs demonstrate significantly higher light output than the Zn-doped LETs, which implies a better candidate for TLs. A C-doped TL was designed based on an *N*-InP/*p*-$In_{0.52}(Al_{0.4}Ga_{0.6})_{0.48}As$/*N*-InP DH-LET. The schematic illustration of band diagram, refractive index profile, and calculated electronic band diagram of the TL are shown in Figure 4.17 (a) and (b), respectively. In the structure, relatively thick emitter and collector layers serve as the

cladding layers and the base as the waveguide and active region. An InP collector was adopted to form a symmetric DH structure due to an improved turn-on characteristics as compared to the InAlAs collector. A 12 nm SQW was employed instead of MQWs to avoid the non-uniform carrier distribution between QWs in the base. To design an optimal base thickness, a calculation on optical confinement factor Γ was performed. In Figure 4.18, Γ in the SQW is plotted against base thickness. The maximum optical confinement factor is 2.46% obtained at a base thickness of 325 nm. However, this thickness is practically too large for a transistor operation. Instead, a base thickness of 262 nm was used with a 125 nm waveguide on each side of the SQW, corresponding to a Γ of 2.38% as indicated by the arrow in Figure 4.18. The epitaxial structure of the TL consists of an InP:Si sub-collector (200 nm, n=1×10^{19} cm^{-3}), an InAlAs:Si etch stop (20 nm, n=8×10^{18} cm^{-3}), an undoped InP collector/cladding (300 nm), a delta doped InP:Si (5 nm, n=1×10^{18} cm^{-3}), an undoped $In_{0.52}(Al_{0.4}Ga_{0.6})_{0.48}As$ spacer (5 nm), an $In_{0.52}(Al_{0.4}Ga_{0.6})_{0.48}As$:C base/active region (262 nm, p=1×10^{19} cm^{-3}) with a 12 nm compressive-strained InGaAs SQW embedded in the middle, a lightly-doped InP:Si emitter spacer (75nm, n=2×10^{17} cm^{-3}), an InP:Si emitter/cladding (1500 nm, n=5×10^{18} cm^{-3}), and an InP:Si^{+} contact (50 nm, n=1×10^{19} cm^{-3}).

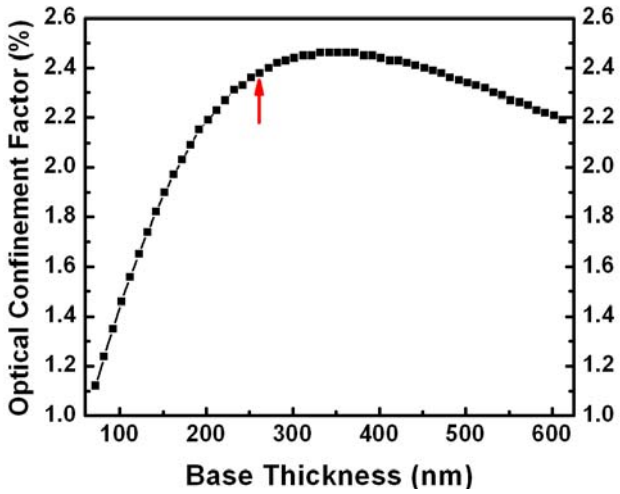

Figure 4.18: Transverse optical confinement factor as a function of base thickness. The arrow indicates the selected base thickness.

The wafer was fabricated in the same way as described in the Zn-doped TLs. Figure 4.19 (a) and (b) shows the side view and top view of the TL. The device is a ridge structure with a 4×400 μm^2 emitter mesa and no facet coating.

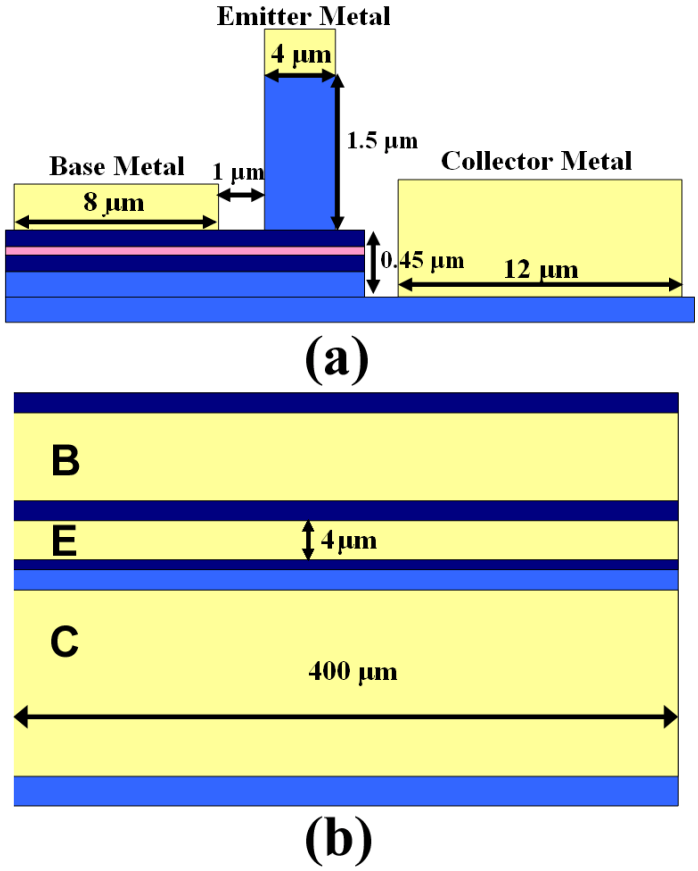

Figure 4.19: (a) Side view and (b) top view of the TL.

Figure 4.20 shows the common-emitter *I-V* characteristics of the TL operating at room temperature (23 °C) and liquid nitrogen temperature (-190 °C). I_B is increased in 8 mA intervals from 0 to 96 mA with V_{CE} swept from 0 to 4 V. At 23 °C the TL turns on sharply at ~0.3 V and β remains almost constant at 0.07 once the transistor is biased above the knee voltage at 0.5 V. The low current gain of the TL is owing to the thick base layer. At -190 °C, significant gain compression was observed and β decreases to 0.02, which is related to the enhanced radiative recombination at low temperatures.

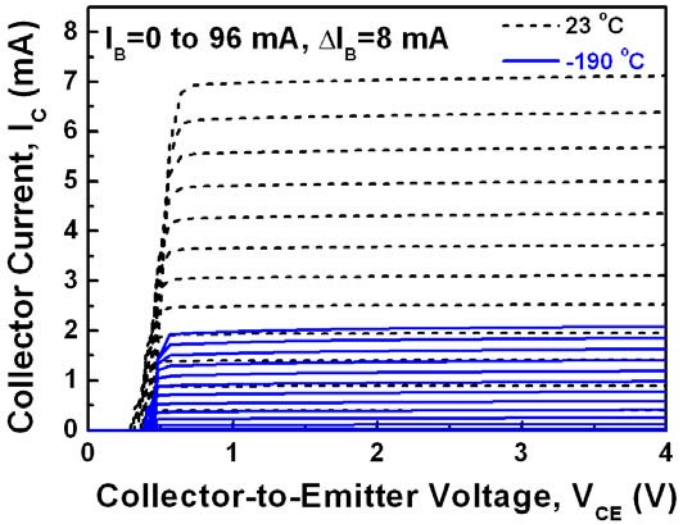

Figure 4.20: Common-emitter *I-V* characteristics of the TL taken at 23 °C and -190 °C.

The optical output as a function of base current (*L-I*) was also measured at 23 °C and -190 °C in CW operation. As shown in Figure 4.21, the light intensity saturates quickly at 23 °C, indicating a dominant spontaneous emission and device heating at this temperature. When the device was cooled down to -190 °C, a change from spontaneous to stimulated emission at I_B= I_{th}=35 mA was observed, as indicated by the arrow, corresponding to a J_{th} of 2.25 kA/cm^2. The stimulated emission spectra after lasing are similar to Figure 3.19 (b) with λ~1.55 μm.

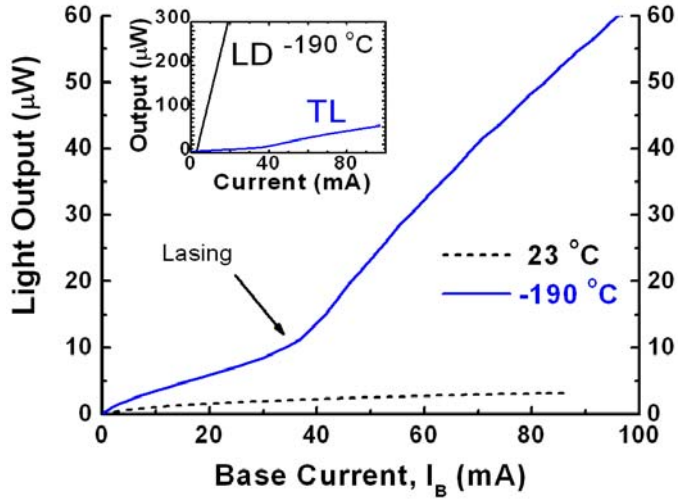

Figure 4.21: Optical output as a function a base current taken at 23 °C and -190 °C. The inset shows the output of the TL and the LD taken at -190 °C.

Despite the lasing performance, the TL shows a low differential quantum efficiency (η_d), which is characterized by the slope of the *L-I* curve. To compare the output characteristics, an InGaAs/In($Al_{0.4}Ga_{0.6}$)As *p-i-n* LD was also grown and fabricated, which consists of a similar SQW active region, In($Al_{0.4}Ga_{0.6}$)As waveguide, and InP cladding layers to the TL except that the waveguide and active region is undoped and top InP cladding is *p*-type. The LD also has the same cavity length and uncoated facets. Shown in the inset of Figure 4.21 is the *L-I* curves for the TL and the LD at -190 °C in CW mode. Obviously the LD has a significantly lower I_{th} of 2 mA and much larger η_d. Since the photodetector only captures a small fraction of the total light outputs of the TL and LD, η_d can only be compared relatively. Using the equation:

$$\eta_d = \eta_i \cdot \frac{\alpha_m}{\alpha_m + \alpha_i}, \tag{4.13}$$

where η_i is the internal quantum (or injection) efficiency of the LD, α_i is the intrinsic cavity loss, and α_m is the mirror loss, we have:

$$\frac{\eta_d(\mathrm{LD})}{\eta_d(\mathrm{TL})} = \frac{\eta_i(\mathrm{LD})}{\eta_i(\mathrm{TL})} \cdot \frac{\alpha_m(\mathrm{LD})}{\alpha_m(\mathrm{TL})} \cdot \frac{\alpha_m(\mathrm{TL}) + \alpha_i(\mathrm{TL})}{\alpha_m(\mathrm{LD}) + \alpha_i(\mathrm{LD})} \tag{4.14}$$

Using $\alpha_m = \frac{1}{L} \cdot \ln\left(\frac{1}{R}\right)$, where L is the cavity length and R is the facet reflectivity, α_m is calculated to be 30 cm^{-1} for both TL and LD with L =400 μm and R=0.3. η_i(LD) and η_i(TL) are assumed to the same given the low temperature condition. $\frac{\eta_d(\mathrm{LD})}{\eta_d(\mathrm{TL})}$ is determined to be ~15 experimentally. A normal α_i of 10 cm^{-1} is assumed in the SQW LD [97]. Thus α_i of the TL can be roughly estimated by Equation 4.14. α_i is calculated to be 570 cm^{-1}, which is remarkably large. This is attributed to the strong intervalence band absorption at long wavelengths in the highly-doped base/waveguide region. Indeed, the absorption coefficient could be as high as 450 cm^{-1} at the doping level of 1×10^{19} cm^{-3} in InGaAs [43], which agrees approximately with our calculated

value. The photon scattering in the defected C-doped InAlGaAs layers may also contribute to the total loss. Compared to the Zn-doped TL, the threshold current density is even higher in the C-doped TL (2.25 vs. 0.33 kA/cm^2 in Zn-doped TL) due to heavier doping level(1×10^{19} vs. 5.3×10^{18} cm^{-3} in Zn-doped TL) despite its higher internal quantum efficiency. The high intrinsic loss essentially prohibits the both Zn- and C-doped TLs from lasing at room temperature and allows only a small fraction of power to be delivered to the facets after lasing at low temperature. Optimization of the TL design is necessary in order to further improve the performances of this novel device, which will be the subject in Chapter 6.

CHAPTER 5

Novel Growth Methods for High P-type Doping

In the last two chapters, the doping behaviors of Zn and C and their impact on the device performance have been examined in detail. Zn is shown to be hard to control in semiconductor matrix while C doping in InAlGaAs alloys using CBr_4 suffers from inferior material quality and poor reproducibility and uniformity. In an attempt to achieve *p*-type doping with high structural, electrical and optical qualities, a couple of novel growth method and technique, including atomic layer epitaxy and modulation doping in superlattices, were investigated.

5.1 Atomic Layer Epitaxy

Atomic layer epitaxy (ALE) has been established as a growth technique in producing III-V compound semiconductor materials with uniform thickness and composition [98]. A fundamental advantage of ALE is the self-limiting mechanism due to saturated surface reactions that allows for accurate control of the thickness at the atomic level [99]. By separately exposing the substrate with individual constituent sources, homogeneous gas-phase reactions are suppressed and adatoms are expected to have enhanced surface mobility [100]. Since its first demonstration of GaAs ALE for III-V materials [101], the ALE method has been widely employed in the growth of nanostructures such as QWs [102 , 103], quantum dots (QDs) [104,105], and delta-doped layers [76,106], III-V compound binary semiconductor films such as GaAs, InAs, InP, GaN, and AlN, as well as the AlGaAs ternary alloy [99,107-113]. ALE growth of compound semiconductors using metalorganic and hydride sources can be readily implemented in a commercial MOCVD reactor by alternative pulse injection of the respective

sources. The benefit of ALE includes interface abruptness, thickness uniformity, enhanced surface migration, and elimination of gas phase reaction.

It is believed that in ALE the methyl-radical-terminated growing surface prohibits further heterogeneous decomposition of MO sources and self-limits the growth rate to one monolayer (ML) per cycle [114,115]. C incorporation will be encouraged by reducing the AsH_3 and H_2 exposure and thus suppressing the hydrogenation of $–CH_3$ [116,117]. This method, the so-called intrinsic doping, has been utilized for the *p*-type doping of GaAs and AlGaAs materials [76,114,118]. The intrinsic C doping by ALE avoids the use of any halide-based carbon precursors and thus the side-effects they bring about such as reduced growth rate, shifting of the alloy compositions, and poor growth reproducibility. It also allows C to be built into lattice only on anion sites thanks to the ALE growth mechanism. This doping method will be examined in the InGaAs ternary and InAlGaAs quaternary alloys, which has not been studied yet from the literature.

In the homoepitaxy of binary materials, growth rates of more than or less than 1 ML/cycle were obtained if the growth temperature is too high or too low, and ALE of exact 1 ML/cycle has been realized by tuning the growth conditions to the surface-reaction-controlled regime [119]. However, for ternary alloy epitaxy on foreign substrates, the growth kinetics on the surface would be much more complicated [120]. Taking InGaAs growth on InP as an example, due to different reactivity of MO sources, surface reaction kinetics could be totally different for In and Ga species and self-limiting of overall growth would be easily broken. In addition, strain energy induced by lattice mismatch may also play an important role in epitaxial growth mode [121].

The InGaAs/InP material system has been important in the development of optoelectronic devices such as photodetectors and lasers and high speed electronic devices such as HBTs and

high-electron-mobility transistors (HEMTs). However, the growth behavior of $In_xGa_{1-x}As$ (x_{In}~0.53) lattice-matched to InP by ALE have not been fully explored as compared to the well-documented GaAs-based materials [98,121,122]. A systematic study is first presented on the dependence of the growth rate and alloy composition of InGaAs on the source exposure and growth temperature in ALE with metalorganic and hydride precursors. By dividing the growth rate into InAs and GaAs components, we elucidate the critical factors that determine the cation incorporation and propose a growth model to explain the different incorporation kinetics of In and Ga during InGaAs ALE.

5.1.1 Surface Reaction Kinetics in InGaAs

InGaAs ALE was performed at 100 Torr on (001) InP substrates by alternatively injecting TMIn and TMGa mixture and AsH_3, separated by 2 s H_2 purge if not specified. The growth cycle was repeated 500 times. Growth temperature from 400 to 550 ^oC was investigated.

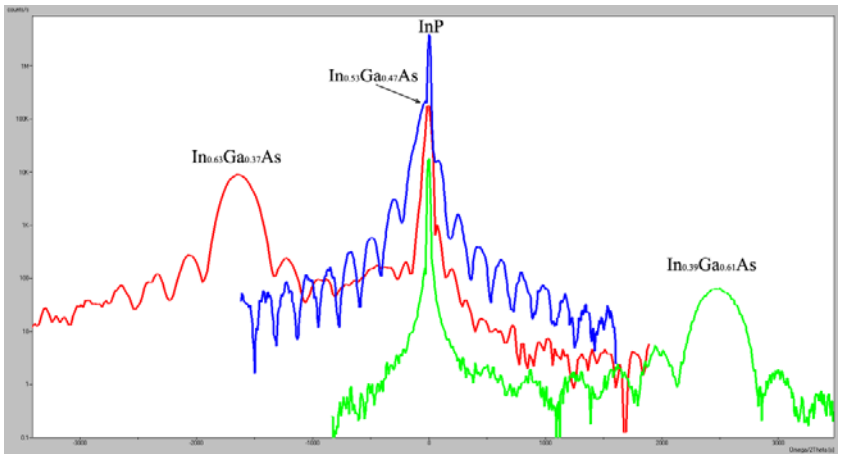

Figure 5.1: XRD *ω*-2*θ* scans near (004) reflection for InGaAs layers with different x_{In}

The as-grown InGaAs films by ALE are specular under optical microscope and the RMS surface roughness is below 0.1 nm as measured by AFM in 5×5 μm^2 scan areas. Due to the thin layer and nearly-lattice-matching condition, InGaAs epitaxial layers with various compositions

in this study were assumed to be fully strained (pseudomorphic) on the substrates, satisfying the condition that the layers within the critical thickness for the formation of misfit dislocation [123]. Figure 5.1 shows the XRD ω-2θ scans for InGaAs with different In compositions. Clear thickness interference fringes are observed, indicating the smoothness of the surface. Simulation on the XRD curves gives the information on the composition as well as thickness of InGaAs layers. In the following section, we discuss how the growth parameters in the ALE influence the In and Ga incorporation into $In_xGa_{1-x}As$ alloys.

5.1.1.1. Effect of AsH_3 and MO precursor exposure

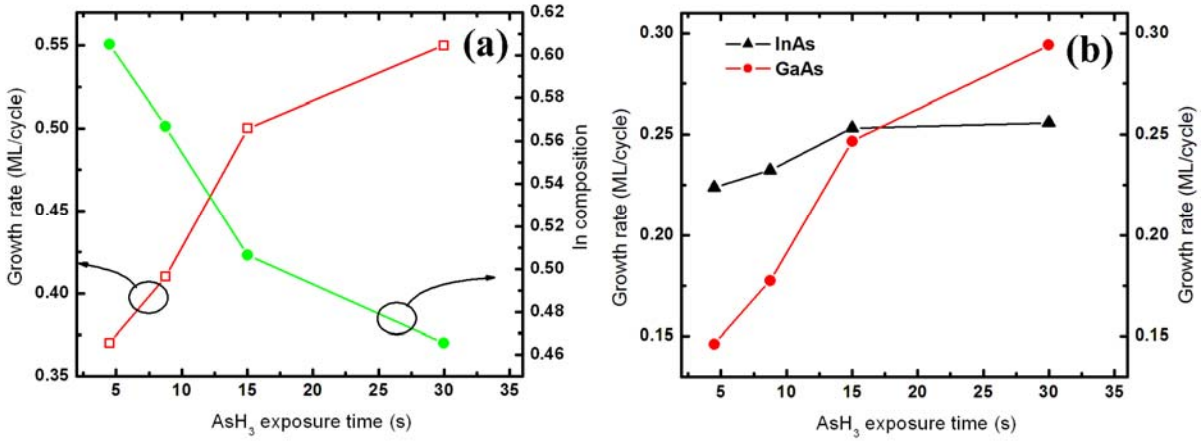

Figure 5.2: Dependence of (a) the total growth rate and In composition of InGaAs and (b) the InAs and GaAs growth rates on AsH_3 exposure time at 500 °C.

First, we studied the effect of AsH_3 exposure time on the growth rate and composition of InGaAs. The growth temperature is set at 500 °C. The flow rates for TMIn and TMGa are fixed at 100 and 6 sccm (corresponding to 7.6 and 16.7 μmol/min), respectively. The pulse duration for the MO precursor is 3 seconds (s). The AsH_3 flow rate is fixed at 60 sccm. Figure 5.2 (a) shows the growth rates and In compositions of InGaAs at different AsH_3 exposure durations from 4 to 30 s. Clearly both the growth rate and the composition are a strong function of the AsH_3 exposure. The growth rate increases from 0.37 to 0.55 ML/cycle while the In composition

decreases from 0.61 to 0.47 with the AsH_3 exposure time. To indentify the underlying mechanism, the individual growth rate of InAs and GaAs is calculated by multiplying the total growth rate by the In or Ga solid composition and this data is plotted in Figure 5.2 (b). It is revealed that with increasing AsH_3 exposure duration, the InAs growth rate does not change significantly and remains around 0.25 ML/cycle whereas the GaAs growth rate increases from 0.15 to 0.29 ML/cycle and contributes to the increase of the overall growth rate of $In_xGa_{1-x}As$.

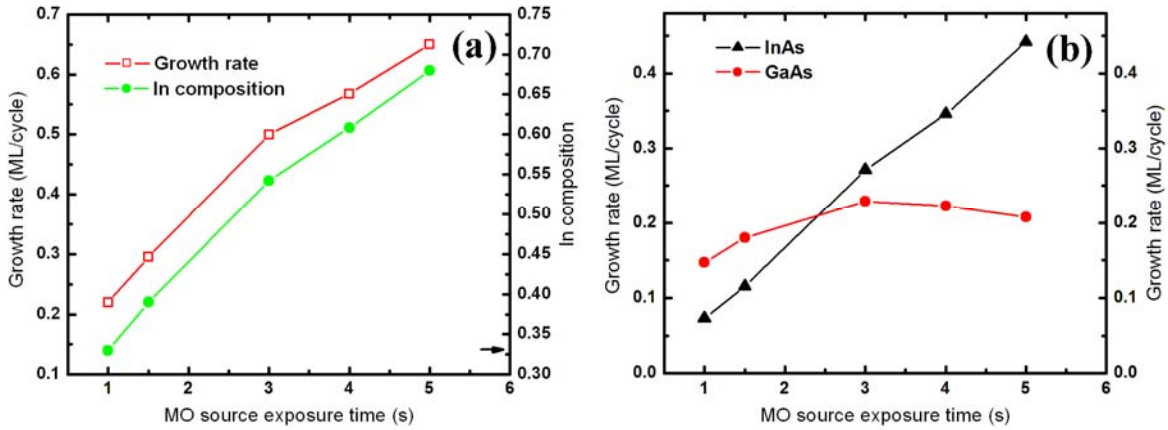

Figure 5.3: Dependence of (a) the total growth rate and In composition of InGaAs and (b) the InAs and GaAs growth rates on MO precursor exposure time at 500 °C. Arrow indicates the In composition in the gas phase.

Secondly, the growth rate and composition of $In_xGa_{1-x}As$ were investigated by varying the MO precursor exposure duration, with the results displayed in Figure 5.3. In this case, the flow rates for TMIn and TMGa are fixed at 100 and 5.6 sccm, respectively, and the pulse duration is varied from 1 to 5 s. The AsH_3 flow is fixed at 60 sccm and the exposure time was 15 s. As shown in Figure 5.3 (a), both the growth rate and the In composition increase significantly with MO precursor exposure time. Saturation of the growth rate or composition latching is not observed, which is different from the results reported by other groups [121,122]. Further increase in the MO precursor exposure time leads to a hazy material surface, which is attributed to the In segregation or large lattice mismatch. The individual growth rate of InAs and GaAs is

also presented in Figure 5.3 (b). The growth rate of InAs increases linearly from 0.07 ML/cycle at 1 s MO precursor exposure to 0.44 ML/cycle at 5 s MO precursor exposure, whereas the GaAs growth rate stays almost constant at 0.2 ML/cycle. Increase of the total growth rate is thus from the contribution of InAs component.

Based on the results shown in Figure 5.2 and 5.3, it can be suggested that during ALE growth of InGaAs at 500 °C for given input flow rates, the incorporation of In in a growth cycle is mainly dependent on the TMIn supply duration and the incorporation of Ga is mainly dependent on the AsH_3 exposure duration. Growth kinetics of GaAs and InAs in ALE has been studied in detail in the literature, and there is no fundamental difference in the growth mechanisms of these two materials [98,99,108,114,122]. In principle, ALE is a completely thermally-driven process. Homogeneous and heterogeneous reactions dominate the growth in different temperature regimes. At low temperatures, the surface reactions govern the ALE process. A slow surface reaction rate causes the growth rate to be smaller than 1 ML/cycle, which is attributed to the steric hindrance effect of group III adsorbates [108,119] or incomplete hydride pyrolysis [115]. At high temperature, on the other hand, significant homogeneous decomposition of MO sources occurs in the gas phase, which precludes an ideal saturated growth process by forming metal multilayers. The ALE growth window is achieved only in the intermediate temperature regime, where surface-exchange reactions are fast enough while gas phase decomposition is still minimal. Consequently, the ALE window strongly depends on the chemical stability of MO precursors. Due to a much lower decomposition temperature of TMIn than TMGa, ALE growth of InAs is performed typically at a temperature 100 °C lower than that of GaAs [98, 124]. At a certain temperature, the surface kinetics could be totally different for the individual growth of InAs and GaAs. In the present study, the different growth kinetics of InAs

and GaAs suggests that the surface chemical states of In and Ga adsorbates could be different. We speculate that at 500 ^{o}C the dominant adsorbate of In species on the growing surface is metal In atoms while the dominant adsorbate of Ga species is $GaCH_3$. It was reported that heterogeneous decomposition of hydrides is not strongly catalyzed on CH_3-terminated surface while they decompose readily on metal surfaces [115]. Thus, when AsH_3 reaches the growing surface during InGaAs ALE, the surface reactions of AsH_3 on the In sites readily occur and the growth rate of InAs is dominated by the In atoms available on the surface. On the other hand, the exchange reaction of AsH_3 on the CH_3-terminated Ga sites is so slow that the decomposition of AsH_3 is incomplete for Ga species, which kinetically limits the incorporation of Ga into InGaAs. With extending the TMGa exposure duration, quasi-saturation is observed and the growth rate of GaAs is only determined by AsH_3 supply. For the growth of InGaAs by ALE, therefore, a self-limiting process could not be realized at this temperature due to the unsaturated growth rate of InAs.

From Figure 5.2 and 5.3, it should also be pointed out that tuning the composition of InGaAs alloys by ALE is very challenging and relies on precise control of both MO precursor and AsH_3 exposure time as well as the input TMIn/TMGa ratio in the gas phase. In conventional MOCVD growth of alloys containing In and Ga, the distribution coefficient of In (defined as the ratio of the concentration of In to Ga in the solid divided by that in the vapor) is close to but less than unity, which holds true for InGaAs, InGaP, and InGaN materials using TMIn and TMGa [125]. However, the In distribution coefficient in the ALE growth of InGaAs is much larger than unity and is dependent on precursor exposure duration, as indicated in Figure 5.2 and 5.3. A distribution coefficient of 4.4 is calculated at MO exposure of 5 s in Figure 5.3 (a), where the In composition in the gas phase is indicated by arrow. Only when the MO precursor exposure

duration is 1 s, the In composition in the epitaxial layer equals to that in the gas phase, which means the In distribution coefficient is exactly unity. It is possible that for 1 s TMGa exposure, a 15 s AsH_3 exposure is long enough to release the methyl radicals from $GaCH_3$ adsorbates and deplete Ga species within a growth cycle. Since the In species is depleted completely in a cycle, the solid-phase composition would be essentially the same as the gas-phase composition.

5.1.1.2. Effect of H_2 purge

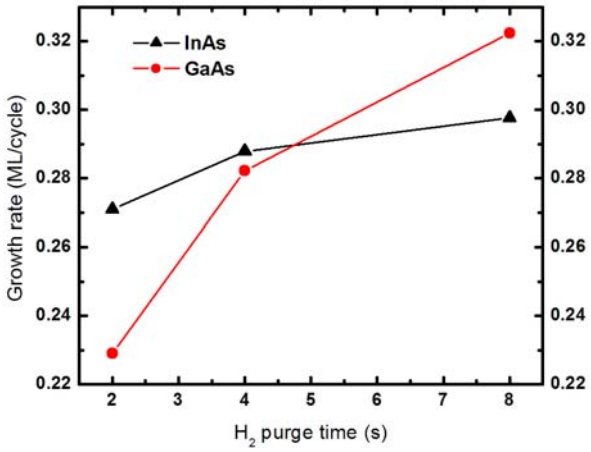

Figure 5.4: Dependence of the InAs and GaAs growth rates on H_2 purge time.

If the InGaAs ALE growth is *partially* dominated by incomplete AsH_3 decomposition, carbon incorporation is expected to increase due to ineffective removal of methyl radicals [116,117]. Besides increasing AsH_3 exposure time, carbon incorporation can be reduced by increasing the H_2 purge time after TMGa exposure. Figure 5.4 shows the growth rates of InAs and GaAs in InGaAs ALE growth with different H_2 purge times. The flow rates for TMIn and TMGa are fixed at 100 and 5.6 sccm, respectively, and the MO-source pulse duration is 3 s. The following H_2 purge is varied from 2 to 8 s. The AsH_3 flow is fixed at 60 sccm and is on for 15 s. Apparently, Ga incorporation is encouraged by the H_2 purge. This can be explained by the enhanced removal of methyl radicals during H_2 purge, resulting in more metal-terminated Ga

sites and thus more ready decomposition of AsH_3. As a comparison, growth rate of InAs is not significantly influenced by H_2 purge.

5.1.1.3. Effect of growth temperature

Since ALE is a thermally-activated process, InGaAs ALE growth at different temperatures has also been investigated. Figure 5.5 (a) shows the total growth rate of InGaAs and individual growth rate of InAs and GaAs as a function of MO precursor exposure time at a growth temperature of 550 °C. During this study, the TMIn flow is fixed at 100 sccm while TMGa is varied from 1.5 to 6 sccm. The AsH_3 flow is fixed at 90 sccm and is on for 3 s. Both InAs and GaAs growth rates increase with MO exposure, and no saturation is observed for the GaAs component. This result suggests that the surface reaction rate on Ga sites is enhanced significantly by elevating the temperature by 50 °C, possibly due to the enhanced methyl radical removal during heterogeneous decomposition of TMGa, and the incorporation of Ga is determined by the TMGa supply. By doubling the flow rate or exposure time of AsH_3, no noticeable change in In composition or growth rate is observed.

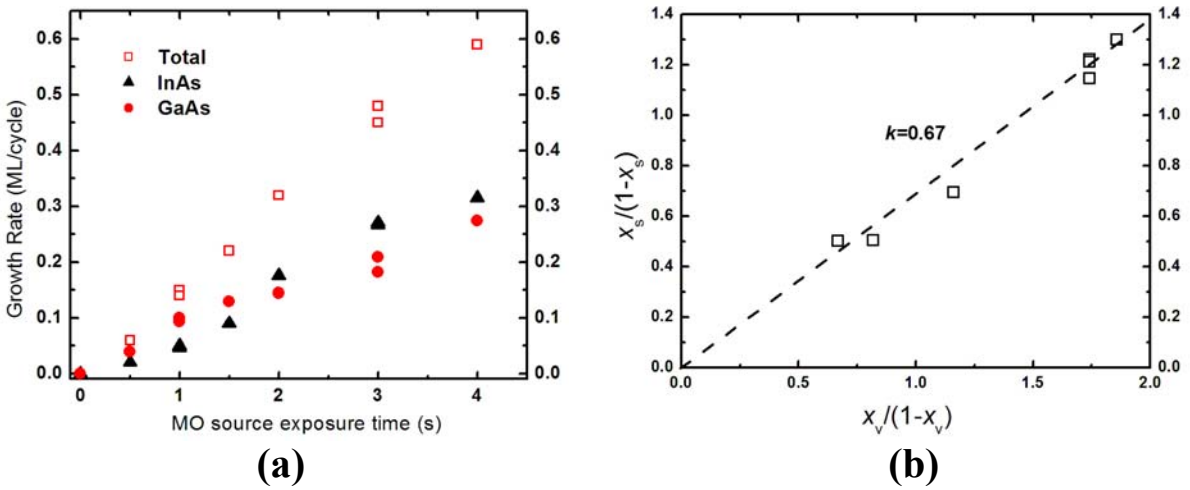

Figure 5.5: (a) Dependence of the total growth rate, InAs and GaAs growth rates on MO exposure time at 550 °C; (b) $x_s/(1-x_s)$ as a function of $x_v/(1-x_v)$ for InGaAs ALE at 550 °C.

The relationship between the In solid composition (x_s) and vapor composition (x_v) is also studied. In Figure 5.5 (b), $x_s/(1-x_s)$ is plotted against $x_v/(1-x_v)$ for different input MO precursor flow rates, with the slope corresponding to the In distribution coefficient. The In distribution coefficient is calculated to be 0.67 through a linear fit, which is close to those in conventional MOCVD growth using TMIn and TMGa [125]. The similar incorporation kinetics of In and Ga implies that at 550 °C surface reaction is fast enough and the growth process is close to the mass-transport-limited regime.

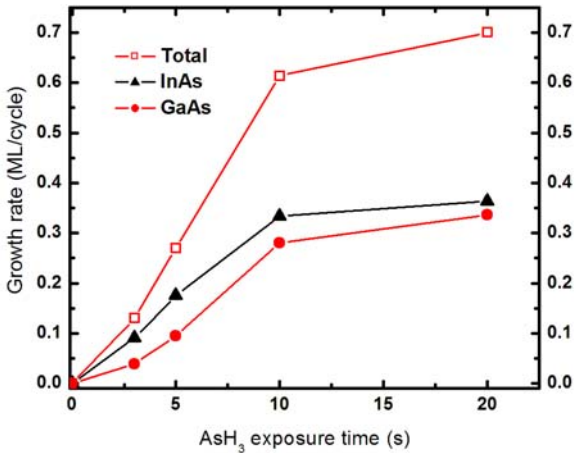

Figure 5.6: Dependence of the total growth rate, InAs and GaAs growth rates on AsH_3 exposure time at 400 °C.

On the other hand, at significantly lower temperature, the surface reactions may govern both InAs and GaAs growth. ALE growth of InGaAs was performed at 400 ^oC. In this case, the growth rates of both InAs and GaAs are limited by the AsH_3 supply, as indicated in Figure 5.6, where TMIn and TMGa are fixed at 100 and 8 sccm, respectively, for 4 s, and AsH_3 flow rate is 150 sccm. A total growth rate of 0.7 ML/cycle is obtained at an AsH_3 exposure time of 20 s. The growth rate is still lower than 1 ML/cycle, which is attributed to the steric hindrance effect [108,119]. The In distribution coefficient is calculated to be around 3, which indicates a lower kinetical barrier for the incorporation of In into InGaAs than that of Ga.

In the present study, the growth rate of InGaAs is less than 1 ML/cycle in all circumstances. Saturated growth occurs when MO sources do not stick to the CH_3-terminated surface, which is only possible at low temperatures. Achieving a true self-limiting growth depends not only on sufficient MO exposure to reach a unity surface coverage but also on enough H_2 purge and AsH_3 exposure. In addition, the steric hindrance effect may complicate the overall process.

5.1.2 Material Quality of InGaAs and InAlGaAs Layers

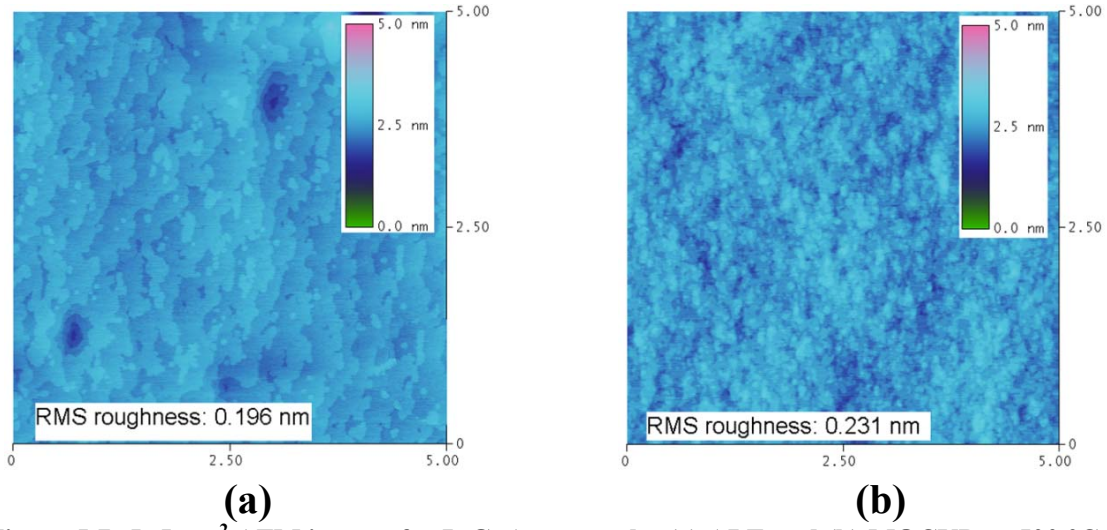

Figure 5.7: 5×5 µm^2 AFM images for InGaAs grown by (a) ALE and (b) MOCVD at 500 °C.

A 200 nm InGaAs layer was grown by ALE with 3 s MO exposure, 4 s H_2 purge, 15 s AsH_3 exposure, and 2 s H_2 purge. For comparison, another InGaAs layer of the same thickness was grown using conventional MOCVD at the same temperature of 500 ^{o}C and a V/III ratio of 120. The lattice-matching condition was obtained by tuning the MO source flow rates. AFM indicates a better surface morphology by ALE growth, characterized by well-defined atomic steps and low RMS roughness as shown in Figure 5.7 (a) in contrast to the InGaAs grown by conventional MOCVD in Figure 5.7 (b). In addition, PL measurement shows a stronger emission from ALE InGaAs, as evidenced in Figure 5.8.

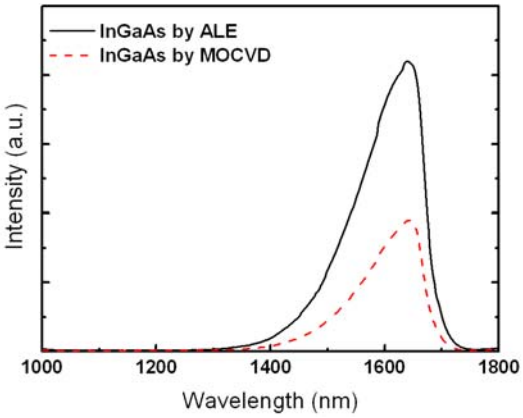

Figure 5.8: PL spectra for the InGaAs layers grown by ALE and MOCVD.

Since lattice-matched InGaAs and InAlAs can be grown on InP substrates, by adjusting the ratio of Al to Ga flows, lattice-matched InAlGaAs quaternary layers can be obtained. Figure 5.9 (a) shows the PL spectra of $In(Al_xGa_{1-x})As$ alloy with different x_{Al}, indicating the bandgap tunability of this material system by ALE. As the Al mole fraction increases, the peak wavelength shifts to higher energies with reduced peak intensities, as expected. In addition, due to the nature of ALE growth, the adatom mobility is greatly improved at low temperature leading to a smooth surface. Figure 5.9 (b) is the XRD ω-2θ scan for a 10-period $In_{0.58}Ga_{0.42}As/In(Al_{0.4}Ga_{0.6})As$ (5.5/15 nm) MQW structure by ALE at 500 ^{o}C, which shows clear and intense satellite peaks indicating excellent interfacial and structural quality.

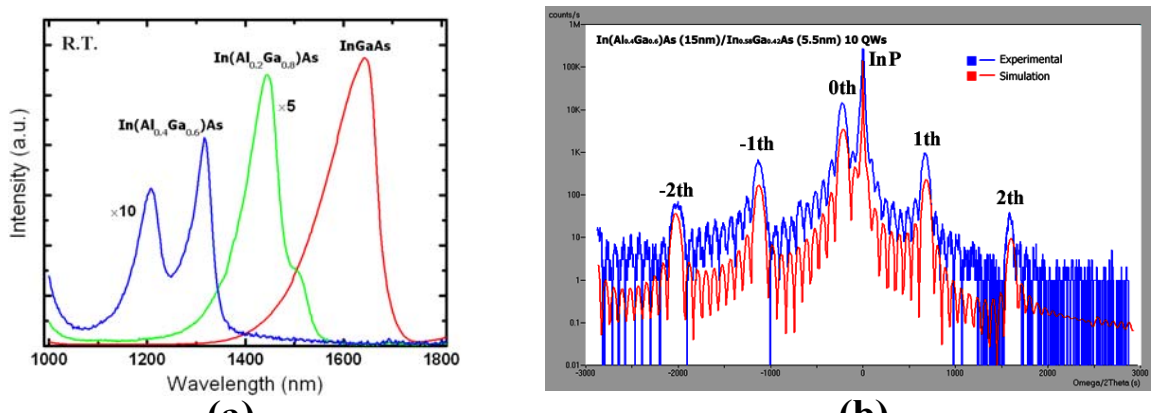

(a) **(b)**

Figure 5.9: (a) PL spectra for InAlGaAs alloys with different x_{Al}; (b) XRD ω-2θ scan for $In_{0.58}Ga_{0.42}As/In(Al_{0.4}Ga_{0.6})As$ MQW structure.

5.1.3 Attempt for P-type Doping

In GaAs ALE, C incorporation and *p*-type doping have been achieved by reducing the AsH_3 and H_2 exposure [116,117]. Similar approach has been taken in InGaAs ALE for C intrinsic doping. AsH_3 exposure time was reduced from 15 s to 2.5 s and H_2 exposure time was reduced from 2 s to 0 s. However, no *p*-type conductivity was achieved in these materials, as indicated in Table 5.1. The lowest *n*-type level is 5.0×10^{15} cm^{-3} attained with 2.5 s AsH_3 purge and no H_2 purge. When Al was added, the material becomes too resistive to measure.

Table 5.1: Purging time and free carrier concentration in In(Al)GaAs layers.

Material	H_2 purge time (s)	AsH_3 purge time (s)	Carrier concentration (cm^{-3})	Mobility ($cm^2/V\cdot s$)
InGaAs	2	15	-1.2×10^{17}	6358
InGaAs	0.5	5	-2.2×10^{16}	9108
InGaAs	0	2.5	-5.0×10^{15}	2220
$In(Al_{0.2}Ga_{0.8})As$	0	2.5	too resistive	--

The high resistivity of the In(Al)GaAs layers is attributed to the use of TMIn as the In source and the low Ga-C_{As} bond concentration in ALE. As mentioned early in C doping using CBr_4, the contribution of *p*-type conductivity in $In_{0.53}Ga_{0.47}As$:C layers is mainly from the Ga-C_{As} bonds. For the InAs components in $In_{0.53}Ga_{0.47}As$ alloys, the In-C bond is weaker than As-C bond [79,80], which means if the decomposition product of TMIn is $InCH_3$, C from $InCH_3$ still tends to occupy the In sites to form As-C_{In} bonds and acts as donors. It is considered that the Ga-C_{As} bond concentration in In(Al)GaAs by ALE can't be made high enough to overcome the As-C_{In} bonds and to compensate the background electron level, and thus the overall conductivity is still *n*-type in our materials. It is possible to make $In_xGa_{1-x}As$ layers *p*-type using intrinsic doping at low x_{In} [126,127], where the concentration of As-C_{In} bonds is lower than that of Ga-C_{As} bonds, or using external dopant such as CBr_4 [78], where the concentration of Ga-C_{As} bonds can be made extremely high. Another approach for *p*-type doping is to avoid the use of TMIn as In

source. Indeed, a very high *p*-type level of 1×10^{19} cm^{-3} has been achieved in metalorganic molecular beam epitaxy (MOMBE) using solid In, TMGa, and solid As as the sources [128,129], where the formation of As-C_{In} bonds is suppressed and only Ga-C_{As} bonds prevail.

5.2 Modulation Doping in InAs/(Al)GaAs Superlattices

Due to the bond strength difference, C is a good *p*-type dopant in GaAs and AlGaAs while it acts as an *n*-type dopant in InAs, which inherently limits its doping capability in In(Al)GaAs alloys. The InAs/(Al)GaAs strain-balanced (SB) superlattice (SL) was thus proposed to deal with this dilemma [130-132]. In this case, C incorporation can be made by intrinsic doping in (Al)GaAs layers while InAs layers are kept undoped to realize the modulation-doped InAs ud/(Al)GaAs:C SLs. The overall material is still *p*-type since (Al)GaAs layers can be doped as high as $\sim1\times10^{20}$ cm^{-3} [133,134]. The average composition in InAs/GaAs SLs can be tuned by changing the thickness of InAs and GaAs layers. Compared to the In(Al)GaAs random alloy the horizontal transport of electrons in the SLs is enhanced by eliminating the alloy scattering while in the vertical direction the materials behave like ternary alloy with averaged physical properties [135]. More importantly, C occupation on In site is completely eliminated, which could lead to a higher vertical mobility and higher carrier lifetime. InAs/GaAs SLs have shown linear optical properties [136] and been employed as the channel material in the FET due to their superior electrical properties [137].

Growth of undoped InAs/GaAs SLs has been investigated on GaAs as well as InP substrates [135,138,139]. Cares must be taken during the growth of the highly-strained InAs and GaAs layers on InP. To avoid the strain-induced three-dimensional (3D) growth [138,139], the thickness of InAs or GaAs layer has to be chosen below critical values.

5.2.1 Intrinsic Doping in (Al)GaAs Layers

The intrinsic doping in (Al)GaAs layers has been carried out at first to identify its optimal growth window. The growth was performed on semi-insulating GaAs substrates between 500 and 600 ^{o}C. TMGa, TMAl, and AsH_3 were used as the precursors. No external dopant was employed. The 300-nm samples were annealed at 500 ^{o}C for 1 min in N_2 ambient. C incorporation is encouraged by reducing the growth temperature and V/III ratio. Figure 5.10 (a) displays the free hole concentration as a function of growth temperature at different V/III ratio. The hole concentration increases with decreasing the temperature and V/III ratio and hole levels as high as 8.2×10^{19} cm^{-3} and 1.0×10^{21} cm^{-3} have been achieved in GaAs and $Al_{0.25}Ga_{0.75}As$, respectively. However, a low V/III ratio also leads to degradation of surface morphology, as indicated by AFM. Combined with the morphology and hole concentration, the optimal V/III ratio for GaAs was found to be 3.2 at 600 ^{o}C, 2.4 at 550 ^{o}C, and 1.6 at 500 ^{o}C. Figure 5.10 (b) shows the 5×5 μm^2 AFM image for GaAs grown at 550 ^{o}C with a V/III of 2.4. A low RMS roughness value of only 0.098 nm was obtained in this layer.

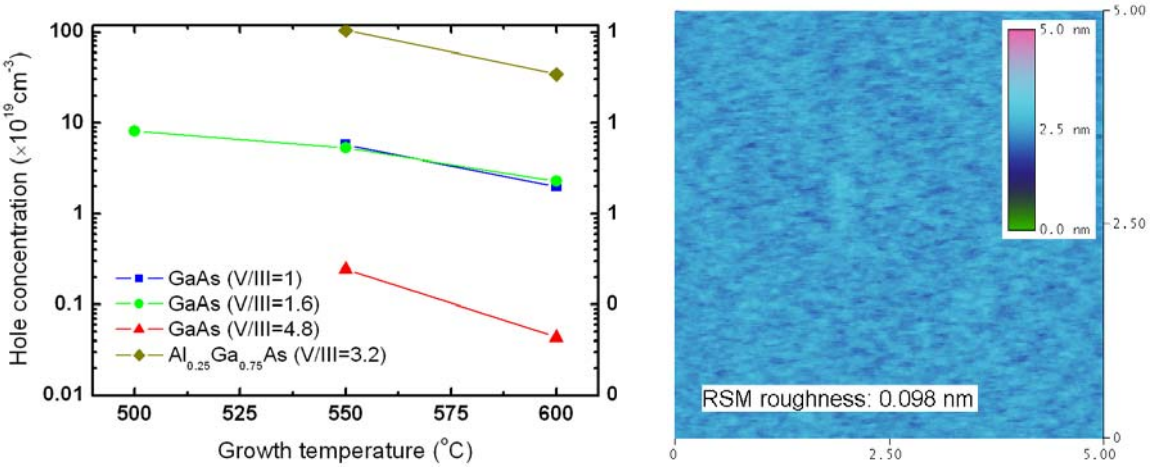

Figure 5.10: (a) Hole concentration as a function of temperature at different V/III ratio in GaAs and AlGaAs; (b) AFM image for GaAs grown at 550 ^{o}C with a V/III of 2.4.

5.2.2 Modulation Doping in InAs/(Al)GaAs SLs

Due to the large lattice mismatch of GaAs and InAs with InP (GaAs: -4.2%; InAs: 3.2%), growth of GaAs and InAs on InP is subjected to defect generation and surface deterioration. In particular, the tensile-strained GaAs on InP suffers from strain relaxation after a critical layer thickness [123] whereas the compressive-strained InAs on InP suffers from the island formation (3D growth) after forming a wetting layer [138-141]. It is, therefore, essential to control the thickness of both GaAs and InAs below critical values and maintain a 2D growth mode to ensure the high quality of the SLs.

To identify the individual critical thickness, we grew a serial of GaAs/$In_{0.53}Ga_{0.47}As$ and InAs/$In_{0.53}Ga_{0.47}As$ SLs on InP with fixed InGaAs thickness and various GaAs or InAs thickness. The SL structures were examined by the optical microscope and XRD. Figure 5.11 shows the XRD ω-2θ scans for 30-period of GaAs/InGaAs (0.92/9.5 nm) and InAs/InGaAs (0.31/9.5 nm) SL structures. Clear and strong satellite peaks are visible, indicating abrupt interfaces. Further increasing the thickness of GaAs or InAs results in weak XRD peaks and poor surface morphology, suggesting the manifestation of strain relaxation or island formation. It was found that the critical thickness is ~1 ML (0.3 nm) for InAs and ~3 ML (0.9 nm) for GaAs.

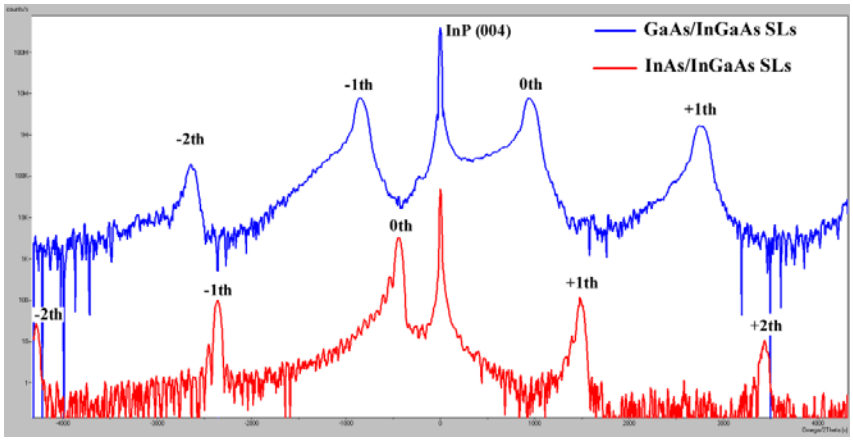

Figure 5.11: XRD ω-2θ scans for 30-period of GaAs/InGaAs (0.92/9.5 nm) and InAs/InGaAs (0.31/9.5 nm) SLs.

As the thickness of InAs and GaAs has to be nearly equal to maintain the lattice matching condition on InP, the thickness of InAs and GaAs was chosen to be ~1 ML in a SL period. The growth temperature was fixed at 550 ^{o}C to utilize the high *p*-type doping in GaAs at this temperature. The V/III ratio was 120 and 2.4 in InAs and GaAs, respectively. After the growth of a 200-period InAs/GaAs SL structure, the surface was specular under optical microscope. Figure 5.12 (a) shows the XRD ω-2θ scans for the 200-period InAs/GaAs (0.30/0.30 nm) and InAs/$Al_{0.15}Ga_{0.85}As$ (0.30/0.33 nm) SL structures. Only the zeroth order peak is observed. Nearly lattice-matched condition is obtained with average x_{In} of 0.514 and 0.47 in the InAs/GaAs SLs and InAs/AlGaAs SLs, respectively. Figure 5.12 (b) displays the 5×5 μm^2 AFM image for the InAs/GaAs SLs. The surface of the SL structure is characterized by 3D islands with a high RMS value of 3.91 nm, possibly resulting from the large strain within the layer. In addition, no PL emission was detected from these samples at room temperature.

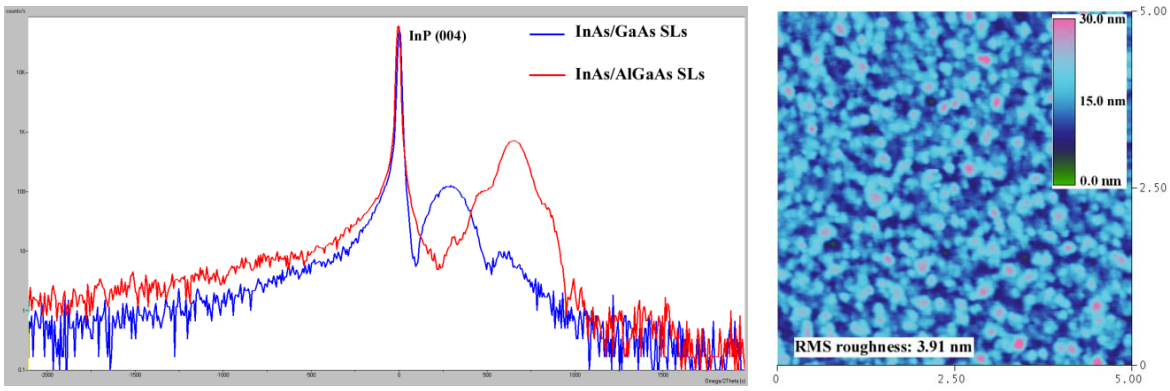

(a) **(b)**

Figure 5.12: (a) XRD ω-2θ scans for the 200-period of InAs/GaAs (0.30/0.30 nm) and InAs/$Al_{0.15}Ga_{0.85}As$ (0.30/0.33 nm) SLs; (b) AFM image for the InAs/GaAs SLs.

The electrical properties for different InAs/(Al)GaAs SLs are summarized in Table 5.2. Again, no *p*-type conductivity has been achieved in these samples. The lowest *n*-type background level is 1.4×10^{17} cm^{-3} in InAs/GaAs SLs, which is even higher than that in InGaAs

random alloy grown by conventional method. The mobility in the SLs is also much lower than that in InGaAs random alloy due to the scattering of the rough surface.

Table 5.2: Free carrier concentration in InAs/(Al)GaAs SL structures.

Material	Carrier concentration (cm^{-3})	Mobility ($cm^2/V{\cdot}s$)
InAs/GaAs SLs	-1.37×10^{17}	2100
InAs/$Al_{0.15}Ga_{0.85}$As SLs	-1.44×10^{17}	1629
InAs/$Al_{0.25}Ga_{0.75}$As SLs	-1.65×10^{17}	1670
InAs/$Al_{0.4}Ga_{0.6}$As SLs	-1.75×10^{17}	1465
InGaAs random alloy	-9.26×10^{16}	6358

The *n*-type conductivity in the InAs/(Al)GaAs SLs is attributed to the thin GaAs layer thickness (1 ML). To satisfy the lattice matching condition, the thickness of GaAs is limited by the critical thickness of InAs on InP, which is normally 1-2 ML determined by the wetting layer thickness [139,141,142]. Within such a thin thickness, AsH_3 carry-over from InAs to GaAs or As-C_{Ga} exchange at GaAs to InAs interfaces may occur, which makes it difficult to preserve the high *p*-type level and unable to compensate the *n*-type background.

In conclusion, ALE and SL structures are proved to be inadequate for *p*-type doping in In(Al)GaAs. In ALE, although excellent structural and optical quality achieved in In(Al)GaAs layers, the concentration of Ga-C_{As} bonds is not high enough to overcome the As-C_{In} bonds. In InAs/(Al)GaAs SLs, separate doping in InAs and GaAs is possible; however, the thin thickness of GaAs layer limited by the wetting layer thickness of InAs on InP can't compensate the *n*-type background level.

CHAPTER 6

Epitaxial Design of a Long Wavelength TL

Unlike a conventional *p-i-n* LD, where the light emission relies on simultaneous injection of both electrons and holes into the active region, TLs utilize the minority carrier recombination in the QW with the majority carrier level staying almost constant in the base. Take an *NpN* TL as an example. Figure 4.15 depicts schematically the carrier distribution profile in the TL in forward active mode. While the electron quasi-Fermi level in the QW is controlled by the base-emitter voltage, the hole level is essentially pinned by the base doping level and its quasi-Fermi level cannot be changed during device operation. In order to achieve population inversion and subsequent stimulated emission, the base doping must be high enough to "preset" the hole quasi-Fermi level in the QW and boost the optical gain. One the other hand, a too high *p*-type doping level inevitably leads to strong intervalence band absorption (IVBA) and a high optical loss, which eventually prohibits the device from lasing as we have observed from the C-doped TL. Therefore, optimization of the base doping level could be of critical importance in realizing a low-threshold long-wavelength TL.

In view of the limited device performance of the TLs, we present theoretical analysis and numerical calculation on the threshold condition of an InAlGaAs/InP TL using a rather simple yet effective approach. Based on the steady state condition that gain is balanced by loss, the base doping level and thickness are numerically investigated through evaluating the threshold carrier and current densities. We show how facet coating, structure engineering, and QW design affect the threshold and output characteristics, which provides insightful guidance in designing a high-performance long-wavelength TL.

6.1 Gain and Loss in a Transistor Laser

As illustrated in Figure 4.15 and derived from Equation 4.7 and 4.8, in a TL below threshold the 2D bound carrier density in the QW N_{QW} is related to the unbounded carrier density N_0 around QW through the expression of :

$$N_{\mathrm{QW}} \cong \frac{\tau_{\mathrm{esc}}}{\tau_{\mathrm{cap}}} N_0. \tag{6.1}$$

In a TL, the profile of N_0 is tilted, set by the boundary condition at the reverse-biased BC junction. As a result, if more than one QW is employed in the active region, the 2D bound carrier density in the second QW will be lower than that in the first one close to the BE junction given the same τ_{cap} and τ_{esc}, and may not contribute to the optical gain. Therefore, the tilted charge distribution in the TL necessitates the use of a SQW.

In an HBT or a TL, the base current I_{B} is to resupply holes and to maintain the charge neutrality in the base region. As the base is usually highly doped, the hole level is insensitive to any hole injection and fixed at the doping level of N_{B} [143]. The confined hole density in the undoped QW region can be obtained based on self-consistent solutions of both Poisson's and Schrödinger's equations. For simplicity, we assume that the hole level in the QW is also N_{B} considering its small volume relative to the base region. As we will see, this approximation gives a direct and critical link between the optical gain and loss while introducing minimal error. The dominant base current component of a TL is the radiative recombination current [19].

Now the active region of a TL can be regarded as a SQW sandwiched by two highly-doped *p*-type layers with a variable electron density of N_{QW} and a fixed hole density of N_{B} in the well. The *p*-type region also serves as the waveguide of the TL. Based on this simple scenario, we carry out calculations on the optical gain and loss in steady state close to the threshold

condition. Assuming that in the SQW all subbands are parabolic and that optical transitions obey rigorous *k*-selection rules, the peak gain g_{p} occurs at the band edge transition, i.e., when:

$$\hbar\omega = E_{\mathrm{g}} + E_{\mathrm{e1}} + E_{\mathrm{h1}}, \tag{6.2}$$

where $\hbar\omega$ is the photon energy, E_{g} is the bandgap energy, and E_{e1} and E_{h1} are the first quantized energy levels of electrons and holes, respectively [144]. Neglecting transition broadening, g_{p} can be expressed as:

$$g_{\mathrm{p}} = g_0(f_{\mathrm{c}}(n) - f_{\mathrm{v}}(p)). \tag{6.3}$$

$f_{\mathrm{c}}(n)$ and $f_{\mathrm{v}}(p)$ are the Fermi electron occupation factors at the conduction and valence band edges, respectively.

$$f_{\mathrm{c}}(n) = \frac{1}{1+e^{(E_{\mathrm{e1}}-F_{\mathrm{c}})/k_{\mathrm{B}}T}}, \tag{6.4}$$

$$f_{\mathrm{v}}(p) = \frac{1}{1+e^{(F_{\mathrm{v}}-E_{\mathrm{h1}})/k_{\mathrm{B}}T}}, \tag{6.5}$$

where F_{c} and F_{v} are the electron and hole quasi-Fermi levels, respectively. g_0 is a material constant given by:

$$g_0 = \omega\sqrt{\frac{\mu}{\epsilon}}\left(\frac{m_{\mathrm{r}}}{\hbar^2 L_{\mathrm{Z}}}\right)\langle R_{\mathrm{cv}}^2\rangle, \tag{6.6}$$

where ω is the angular frequency of light, μ is the permeability, ε is the dielectric constant, m_{r} is the reduced effective mass given by $\frac{m_{\mathrm{e}}^* \cdot m_{\mathrm{h}}^*}{m_{\mathrm{e}}^* + m_{\mathrm{h}}^*}$, m_{e}^* and m_{h}^* are the effective mass of electrons and holes, respectively, L_{Z} is the QW width, and $\langle R_{\mathrm{cv}}^2\rangle$ is the matrix element of the dipole moment [42,145].

To get a more clear relationship of g_{p} on the carrier density, Equation 6.3 can be rewritten as [144-146]:

$$g_{\mathrm{p}} = g_0\left(1 - e^{-n/N_{\mathrm{C}}} - e^{-p/N_{\mathrm{V}}}\right), \tag{6.7}$$

where

$$N_{\mathrm{C}} = \frac{m_{\mathrm{e}}^* k_{\mathrm{B}} T}{\pi \hbar^2 L_{\mathrm{Z}}} \sum_{n=1}^{\infty} e^{(E_{\mathrm{e}1} - E_{\mathrm{e}n})/k_{\mathrm{B}}T},$$

and

$$N_{\mathrm{V}} = \frac{m_{\mathrm{h}}^* k_{\mathrm{B}} T}{\pi \hbar^2 L_{\mathrm{Z}}} \sum_{n=1}^{\infty} e^{(E_{\mathrm{h}1} - E_{\mathrm{h}n})/k_{\mathrm{B}}T}.$$

$E_{\mathrm{e}n}$ and $E_{\mathrm{h}n}$ are the nth quantized energies in conduction band and valence band, respectively. Equation 6.7 is the exact expression of g_{p} if only one conduction and one valence subband are occupied. Only heavy hole band and TE mode are considered in the derivation. With independent control over electron and hole densities, in a TL we have:

$$g_{\mathrm{p}} = g_0\left(1 - e^{-N_{\mathrm{QW}}/N_{\mathrm{C}}} - e^{-N_{\mathrm{B}}/N_{\mathrm{V}}}\right). \tag{6.8}$$

As the highly *p*-doped region serves as the waveguide in a TL, IVBA is considered as the main intrinsic loss mechanism. Assuming that other losses such as free carrier absorption in the cladding layers or photon scattering at the interfaces are negligible, the total optical loss (α_{T}) of a TL is:

$$\alpha_{\mathrm{T}} = \alpha_{\mathrm{i}} + \alpha_{\mathrm{m}}, \tag{6.9}$$

where

$$\alpha_{\mathrm{i}} = (\Gamma_{\mathrm{WG}} + \Gamma_{\mathrm{QW}})k_{\mathrm{p}}N_{\mathrm{B}}, \tag{6.10}$$

and

$$\alpha_{\mathrm{m}} = \frac{1}{2L}\ln\left(\frac{1}{R_1R_2}\right). \tag{6.11}$$

α_{i} is the intrinsic loss and α_{m} accounts for mirror loss (optical output). In Equation 6.10 and 6.11, Γ_{WG} and Γ_{QW} are the optical confinement factors of the waveguide and QW, respectively, k_{p} is the IVBA coefficient, L is the cavity length, and R_1 and R_2 are the facet reflectivity. Then the threshold condition

$$\Gamma_{\mathrm{QW}}g_{\mathrm{p}} = \alpha_{\mathrm{i}} + \alpha_{\mathrm{m}}$$

becomes:

$$\Gamma_{\mathrm{QW}}g_0\left(1 - e^{-N_{\mathrm{QW}}/N_{\mathrm{C}}} - e^{-N_{\mathrm{B}}/N_{\mathrm{V}}}\right) = (\Gamma_{\mathrm{WG}} + \Gamma_{\mathrm{QW}})k_{\mathrm{p}}N_{\mathrm{B}} + \frac{1}{2L}\ln\left(\frac{1}{R_1R_2}\right). \tag{6.12}$$

The recombination lifetime τ_r in Equation 4.7 at high injection level is given by [6]:

$$\frac{1}{\tau_{\mathrm{r}}} = A + BN_{\mathrm{B}} + CN_{\mathrm{B}}(N_{\mathrm{B}} + N_{\mathrm{QW}}). \tag{6.13}$$

Neglecting A in high-quality materials [95], at threshold when N_{QW}=N_{th} we obtain the threshold current density as:

$$J_{\mathrm{th}} = \frac{qL_{\mathrm{Z}}N_{\mathrm{th}}}{\tau_{\mathrm{r}}} = qL_{\mathrm{Z}}N_{\mathrm{th}}(BN_{\mathrm{B}} + CN_{\mathrm{B}}(N_{\mathrm{B}} + N_{\mathrm{th}})). \tag{6.14}$$

where q is the electron charge. It should be pointed out that J_{th} accounts for the net current that flows into the QW, which is exactly the difference between the emitter current I_{E} and collect

current I_C if the recombination current in base bulk region is neglected. In this case, the base current is:

$$I_B = I_E - I_C = A_E J_{th}, \tag{6.15}$$

where A_E is the emitter size.

Starting from these equations, we study the threshold condition in TLs. Two structures have been examined, i.e. a double heterostructure (DH) TL and a separate confinement heterostructure (SCH) TL.

6.2 Double Heterostructure Transistor Laser

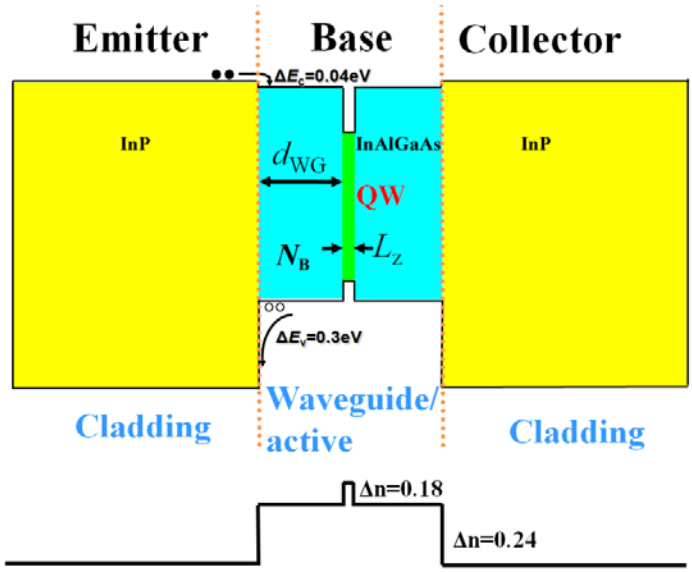

Figure 6.1: Schematic band diagram and refractive index profile for an *N*-InP/*p*-In($Al_{0.4}Ga_{0.6}$)As/*N*-InP DH TL.

Figure 6.1 shows the schematic band diagram and refractive index profile for an *N*-InP/*p*-In($Al_{0.4}Ga_{0.6}$)As/*N*-InP DH TL (similar to Figure 4.17 (a)). In the structure, the InP emitter and collector serve as the cladding layers and In($Al_{0.4}Ga_{0.6}$)As base serves as the waveguide layer.

An 8 nm undoped compressive-strained $In_{0.58}Ga_{0.42}As$ QW is placed in the middle of the base. In practice, Si can be used as the *n*-type dopant while C as the *p*-type dopant. The collector region includes (towards the growth direction) an InP:Si subcollector (300 nm, $n=1\times10^{19}$ cm^{-3}), an InAlAs:Si etch stop (20 nm, $n=1\times10^{19}$ cm^{-3}) and an undoped InP collector/cladding (300 nm) and the emitter region includes a lightly-doped InP:Si emitter spacer (75nm, $n=2\times10^{17}$ cm^{-3}), an InP:Si emitter/cladding (1500 nm, $n=5\times10^{18}$ cm^{-3}) and an InP:Si^{+} contact (50 nm, $n=1\times10^{19}$ cm^{-3}). The $In(Al_{0.4}Ga_{0.6})As$ waveguide thickness d_{WG} and base doping level N_B are variables to be determined. The whole structure is symmetric. Experimentally we have demonstrated a TL based on this structure operating at 77 K in continuous wave mode with N_B of 1×10^{19} cm^{-3} and d_{WG} of 125 nm.

The optical confinement factors are a single function of d_{WG}. Figure 6.2 is a plot of Γ_{QW} and Γ_{WG} against d_{WG} for the DH TL. Note Γ_{WG} takes into account the confinement in the whole waveguide region. It is clear that Γ_{QW} increases with d_{WG} and then saturates at 1.6% while Γ_{WG} is much larger than Γ_{QW}.

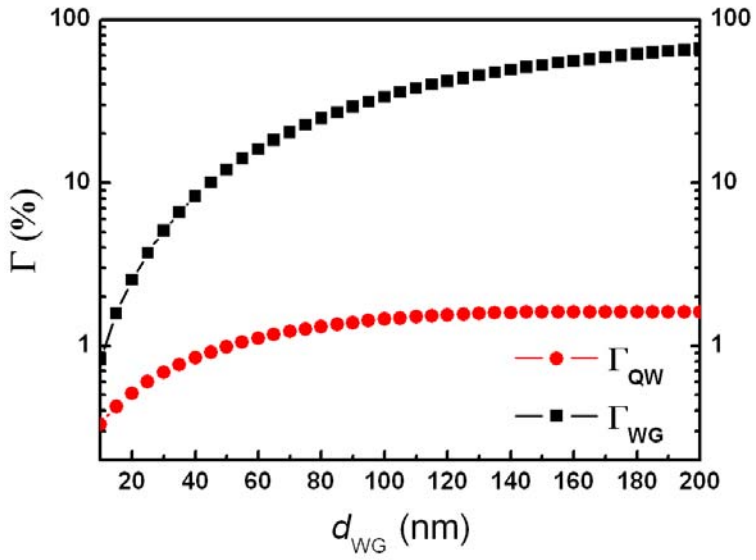

Figure 6.2: Γ_{QW} and Γ_{WG} as a function of d_{WG} in the DH TL.

From Equation 6.12 one can tell that the solution of N_{QW} is strongly dependent on the choice of N_{B} and d_{WG}. In certain circumstances, there is no solution for N_{QW}, which means that the total loss is larger than the maximum gain even when N_{QW} approaches infinity. Therefore, we define maximum available gain G_{m} as:

$$G_{\mathrm{m}} = \Gamma_{\mathrm{QW}} g_0 \left(1 - e^{-N_{\mathrm{B}}/N_{\mathrm{V}}}\right) \tag{6.16}$$

to account for the modal gain when the pumping level is very high and the term $e^{-N_{\mathrm{QW}}/N_{\mathrm{C}}}$ is negligible. And the total loss again is:

$$\alpha_{\mathrm{T}} = (\Gamma_{\mathrm{WG}} + \Gamma_{\mathrm{QW}}) k_p N_{\mathrm{B}} + \frac{1}{2L} \ln\left(\frac{1}{R_1 R_2}\right). \tag{6.17}$$

If $G_{\mathrm{m}} > \alpha_{\mathrm{T}}$, then there will be a solution for N_{QW}:

$$N_{\mathrm{QW}} = N_{\mathrm{th}} = N_{\mathrm{C}} \ln\left(\frac{\Gamma_{\mathrm{QW}} g_0}{\Delta}\right), \tag{6.18}$$

and

$$\Delta = G_{\mathrm{m}} - \alpha_{\mathrm{T}}. \tag{6.19}$$

If Δ is negative, there will be no solution for N_{th}. To reduce N_{th}, it is necessary to maximize Δ by optimizing N_{B} and d_{WG}.

We inspect a TL with a cavity length L of 800 μm and as-cleaved mirrors of $R_1 = R_2 = 0.3$, which gives a mirror loss of 15 cm^{-1}. k_p is chosen to be 4×10^{-17} cm^{-2} [42,43] and g_0 is 4847 cm^{-1} for an 8 nm SQW [145]. m_{e}^* and m_{h}^* are $0.051m_0$ and $0.217m_0$, respectively [147], where m_0 is the electron rest mass. N_{C} and N_{V} are computed to be 7×10^{17} cm^{-3} and 3×10^{18} cm^{-3}, respectively using a finite barrier model assuming $\Delta E_{\mathrm{c}} = 0.72\Delta E_{\mathrm{g}}$. The emission wavelength is

1.56 μm from the band edge transition. By plugging in Γ_{QW} and Γ_{WG} from Figure 6.2 for a certain d_{WG}, we are positioned to evaluate G_m and α_T at different N_B.

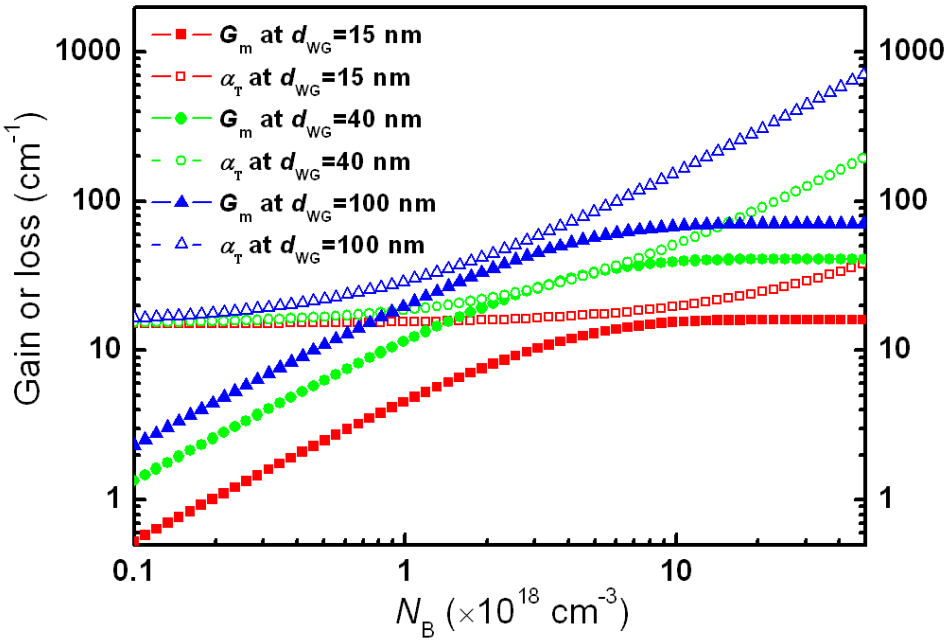

Figure 6.3: G_m and α_T as a function of N_B at d_{WG} of 15, 40, and 100 nm.

Figure 6.3 shows G_m and α_T as a function of N_B at d_{WG} of 15, 40, and 100 nm, respectively. N_B spans from 1×10^{17} to 5×10^{19} cm^{-3}. At low N_B α_T approaches α_m while at high N_B G_m saturates at $\Gamma_{QW}g_0$. It is evident that α_T is larger than G_m in most cases. At d_{WG} of 15 nm, G_m is too low to overcome α_T resulting from a small Γ_{QW}. On the other hand, at d_{WG} of 100 nm, α_T is too high for G_m due to a large Γ_{WG}. Only at d_{WG} of 40 nm, G_m and α_T have intersections in a certain range of N_B, which indicates that Δ is positive and N_{th} exists only at this narrow range.

To get a full picture of the "living zone" for the DH TL, a 2D contour plot (map) of Δ on d_{WG} and N_B is generated, as displayed in Figure 6.4 (a). d_{WG} is from 10 to 160 nm and N_B is from 1×10^{17} to 2×10^{19} cm^{-3}. Clearly only a narrow zone with positive Δ will support lasing, with

the maximum Δ of 0.6 cm^{-1} obtained at $d_{WG} = 35$ nm and $N_B = 4 \times 10^{18}$ cm^{-3}. Thus, to achieve a long wavelength DH TL at room temperature, the base doping and thickness should be stringently and precisely controlled. Our original design with N_B of 1×10^{19} cm^{-3} and d_{WG} of 125 nm is way out of this range, which prohibits the DH TL from lasing at room temperature and also limits its output power after lasing 77 K.

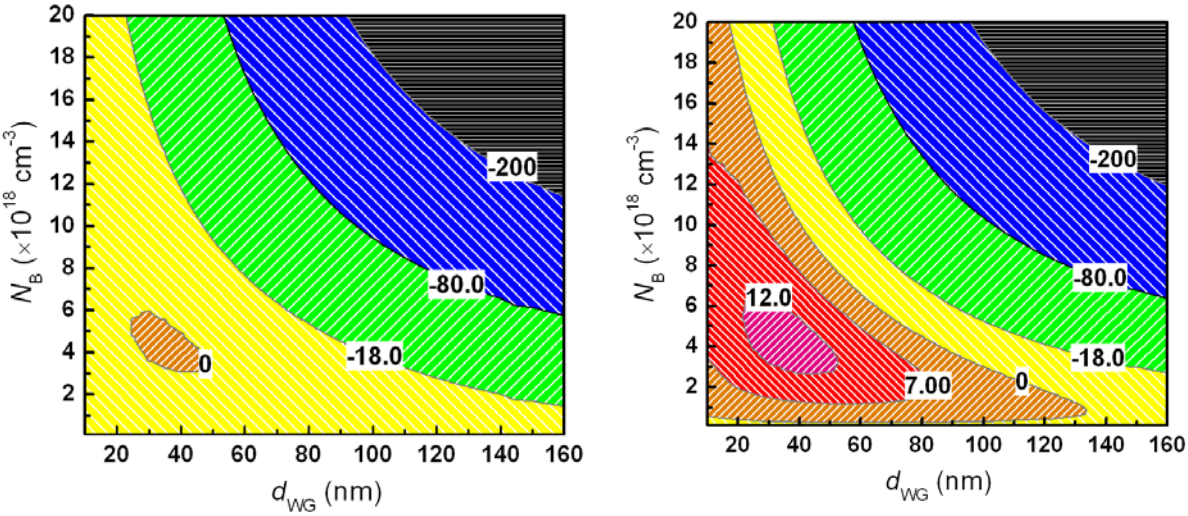

Figure 6.4: 2D contour plot of Δ for the DH TL with (a) as-cleaved mirrors and (b) coated mirrors.

As implied from Figure 6.3, one way to ease the lasing condition and expand the selectable range is to lower the mirror loss α_m. For example, if coated mirrors are employed with $R_1 = 0.95$ and $R_2 = 0.7$, the mirror loss will be reduced to 2.5 cm^{-1}. Figure 6.4 (b) shows the 2D contour plot of Δ for a DH TL at this condition. The region with positive Δ is tremendously extended and the maximum Δ is 13.1 cm^{-1}, much larger than in the uncoated case. Consequently, the threshold current density will be remarkably reduced. However, the highly-reflective mirrors also bring about reduced optical output. The threshold current density and optical output of these devices will be discussed later.

6.3 Separate Confinement Heterostructure Transistor

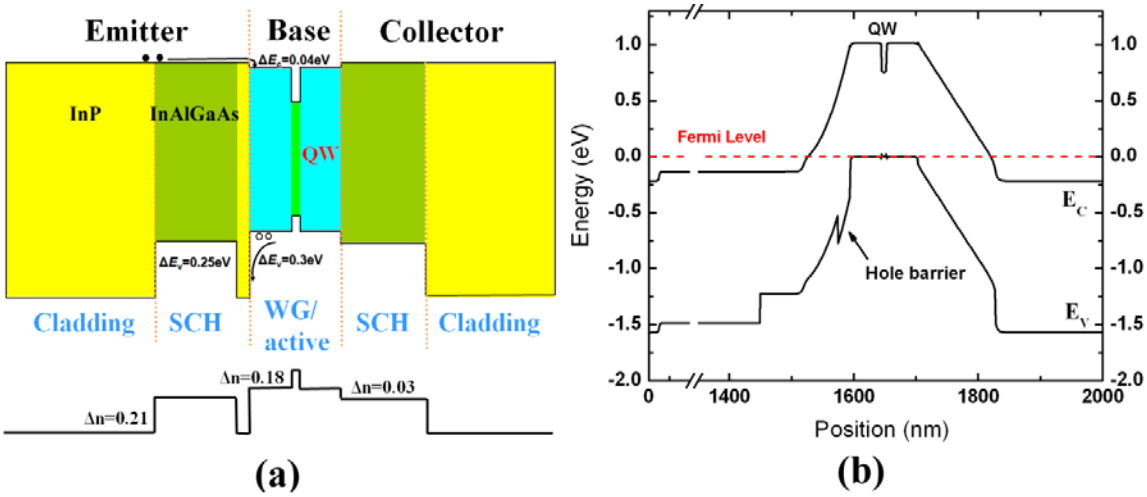

Figure 6.5: (a) Schematic representation of band structure and refractive index profile of a SCH TL; (b) Calculated equilibrium band diagram.

In the DH TL structure, the confinement factors in the QW and waveguide are dependent on the waveguide thickness as revealed in Figure 6.2. Whereas increasing d_{WG} leads to enhanced Γ_{QW} and G_{m}, it also results in a large Γ_{WG} and thus a large α_{T}. This apparent trade-off can be eliminated by moving part of the waveguide layers into the emitter and collector regions to form a SCH TL. In this case, the SCH layer thickness can be chosen to maximize Γ_{QW} while not affecting Γ_{WG}. Shown in Figure 6.5 (a) is the schematic band diagram and refractive index profile for a SCH TL. In the structure, $In(Al_{0.47}Ga_{0.53})As$ alloy is chosen as the SCH material. When the Al composition in $In_{0.53}(Al_xGa_{1-x})_{0.47}As$ alloys increases, the band offset between InAlGaAs and InP changes from the straddling lineup for InGaAs to the staggered lineup for InAlAs, and a nearly continuous conduction band heterostructure is formed at a relative Al composition of 47% [47], as implied from Equation 1.2. As a result, no electron blocking is expected if part of the InP cladding is replaced by $In(Al_{0.47}Ga_{0.53})As$ alloy. The SCH layer is either *n*-type doped in emitter or undoped in collector and the optical loss in these layers is

neglected since the free carrier absorption in *n*-type V-III materials are much smaller than IVBA in *p*-type materials [148]. Thus Γ_{WG} still refers to the optical confinement in the highly-doped base/waveguide layers. The structure enjoys a short base/active region and an extended cladding, similar to a SCH LD. The continuous conduction band in the emitter facilitates electron transport while holes are blocked by a thin (20 nm) InP layer. With both $In(Al_{0.47}Ga_{0.53})As$ and InP being the emitter, the structure exemplifies a composite emitter concept [149]. The thin InP layer severs as an emitter, an etch stop, and a base passivation layer. The base/active region is similar to that in the DH TL with N_B and d_{WG} to be determined. Figure 6.5 (b) illustrates the calculated band diagram for a SCH TL with $d_{WG} = 50$ nm and $N_B = 1 \times 10^{19}$ cm^{-3}. The whole structure is nearly symmetric.

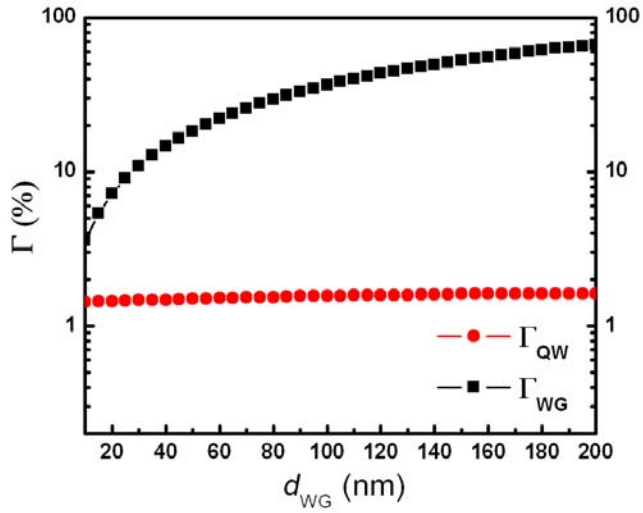

Figure 6.6: Γ_{QW} and Γ_{WG} as a function of d_{WG} in the SCH TL.

Figure 6.6 shows the dependence of Γ_{QW} and Γ_{WG} on d_{WG} in the SCH TL. The SCH layer thickness is chosen in the way that a maximum Γ_{QW} is obtained. Not surprisingly Γ_{QW} remains almost constant at maximum value of 1.6%. The 2D contour of Δ for the SCH TL with the same cavity length and as-cleaved mirrors is generated, with the results displayed in Figure 6.7. Area with positive Δ is conspicuous in this map. Δ increases significantly as d_{WG} decreases,

which is a result from reduced Γ_{WG}. The SCH TL promises improved threshold characteristics than the DH TL.

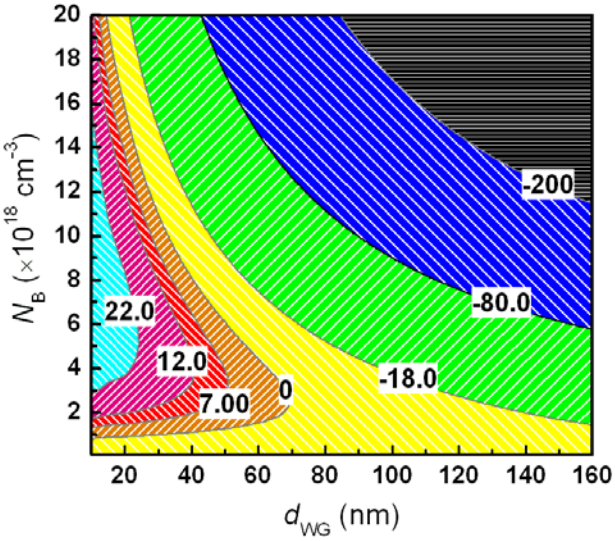

Figure 6.7: 2D contour plot of Δ for the SCH TL with as-cleaved mirrors.

With Δ being known, N_{th} can be calculated using Equation 6.18, and subsequently J_{th} can be obtained using Equation 6.14. B and C are assumed to be 1×10^{-10} cm^3/s and 5×10^{-29} cm^6/s, respectively [95,96]. To compare the threshold characteristics of the DH TL and SCH TL, we calculate N_{th} and J_{th} as a function of N_B at a fixed d_{WG} of 40 nm. Figure 6.8 summarizes the results for the DH TLs with as-cleaved and coated mirrors and the SCH TL with as-cleaved mirrors, with N_{th} in (a) and J_{th} in (b). The DH TL with as-cleaved mirrors shows the highest N_{th} and narrowest N_B range. The lowest N_{th} attainable with the as-cleaved DH TL is 3.0×10^{18} cm^{-3}. By using coated mirrors or a SCH structure, the selectable N_B range is significantly expanded and lowest N_{th} attainable is around 1.0×10^{18} cm^{-3}. J_{th} exhibits a similar trend for the DH and SCH TLs. The lowest J_{th} attainable with the DH TLs with as-cleaved and coated mirrors and the SCH TL with as-cleaved mirrors are 642.8, 31.4, and 111.6 A/cm^2, respectively. In all the devices J_{th} increases significantly with N_B owing to a reduced carrier lifetime.

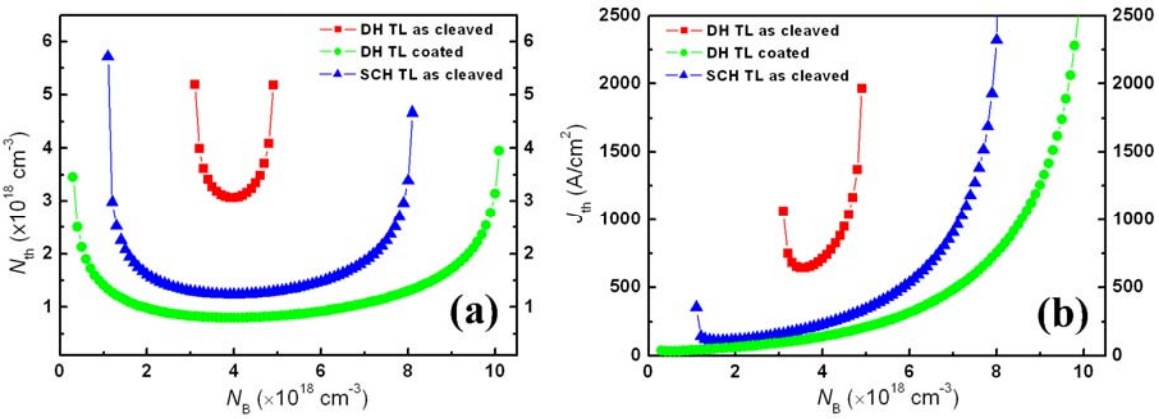

Figure 6.8: Dependence of (a) N_{th} and (b) J_{th} on N_{B} for the DH and SCH TLs.

Reducing the mirror loss by using either facet coating or longer cavity helps to reduce the threshold current density, but it also limits the optical output power. For a given current injection level above threshold, the optical output of a LD or a TL is proportional to $\alpha_{\mathrm{m}}/(\alpha_{\mathrm{i}}+\alpha_{\mathrm{m}})$, as from Equation 4.13. Figure 6.9 shows the dependence of $\alpha_{\mathrm{m}}/(\alpha_{\mathrm{i}}+\alpha_{\mathrm{m}})$ on N_{B} for the DH and SCH TLs. d_{WG} is still kept at 40 nm. The value of $\alpha_{\mathrm{m}}/(\alpha_{\mathrm{i}}+\alpha_{\mathrm{m}})$ drops rapidly with N_{B}, with the coated DH TL being minimal. Considering both threshold and output characteristics, the SCH TL design represents an optimal balance between the threshold current density and optical output power.

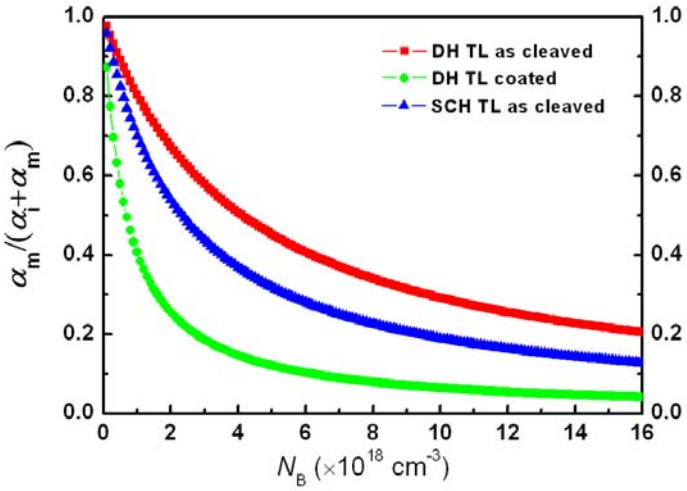

Figure 6.9: Dependence of $\alpha_{\mathrm{m}}/(\alpha_{\mathrm{i}}+\alpha_{\mathrm{m}})$ on N_{B} for the DH and SCH TLs.

6.4 Quantum Well Design

For a conventional LD with lossy waveguide, one way to boost the optical gain is to use MQWs. However, the nonuniform distribution of electrons in the base restricts us to a SQW. Another universal way to reduce the threshold current density is to incorporate some strain in the active region, which modifies the hole effective mass and thus lowers the value of N_V in Equation (8) [144,147]. We calculate the N_{th} and J_{th} as a function of N_B for SCH TLs at a fixed d_{WG} of 40 nm with 8 nm strained $In_xGa_{1-x}As$ QW. The In composition x varies from 58%, 60%, 63%, to 68%, corresponding to a compressive strain of 0.32%, 0.47%, 0.68%, and 1%, respectively. The results are summarized in Figure 6.10. As expected, both N_{th} and J_{th} decrease steadily with increasing In composition. A lowest J_{th} of 73.5 A/cm^2 is obtained for the TL with an $In_{0.68}Ga_{0.32}As$ SQW.

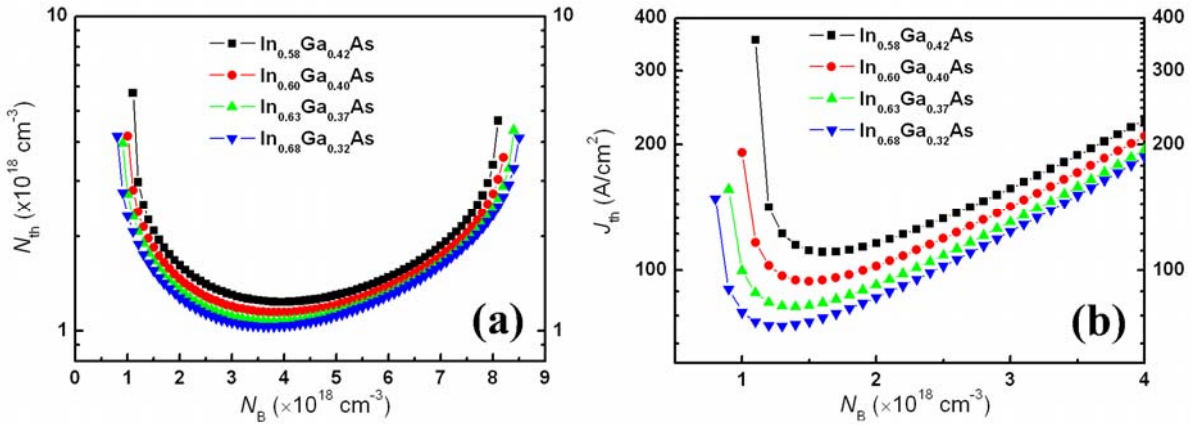

Figure 6.10: Dependence of (a) N_{th} and (b) J_{th} on N_B for SCH TLs with different strain in the QW.

QW thickness L_Z is also an important parameter to deal with. The dependence of N_{th} and J_{th} on L_Z in QW LDs is rather complicated [150]. On the one hand, although an enhanced Γ_{QW} resulting from increasing L_Z is completely offset by the $\frac{1}{L_Z}$ factor in g_0, leading to a little variation of $\Gamma_{QW}g_0$ product, increasing L_Z does increase the modal gain by reducing N_C and N_V

and thus filling band more effectively. On the other hand, J_{th} may rise as it is proportional to L_{Z} from Equation 6.14. Figure 6.11 shows the calculated N_{th} and J_{th} as a function of N_{B} for the same SCH TL structure with L_{Z} of 8, 12, and 16 nm. The QW material is $In_{0.58}Ga_{0.42}As$. While N_{th} is clearly shown to decrease with L_{Z}, J_{th} is minimal at $L_{\mathrm{Z}} = 12\,\mathrm{nm}$. The lowest J_{th} attainable is 72.9 A/cm^2 for the TL with a 12 nm SQW. It should be pointed out that the calculation does not consider the variation of emission wavelength caused by the change of strain or QW thickness.

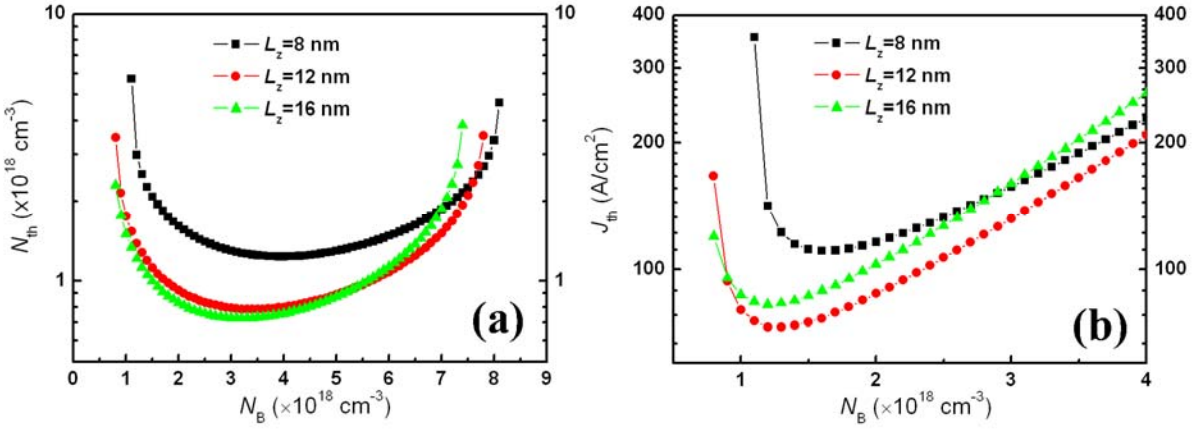

Figure 6.11: Dependence of (a) N_{th} and (b) J_{th} on N_{B} for SCH TLs with different L_{Z} of the QW.

With improved performance achieved through the active region design, comparison is made between the TLs and a conventional LD. We consider a *p-i-n* SCH SQW LD with a similar structure to Figure 6.5 (a) except the doping profile, i.e., the waveguide is undoped and top cladding is *p*-doped. Again, d_{WG} is fixed at 40 nm and an 8 nm strained $In_{0.58}Ga_{0.42}As$ QW is employed. The intrinsic loss in the LD is assumed to be 5 cm^{-1} [97]. Table 6.1 summarizes the performances of the LD and SCH TLs with different QW designs. As-cleaved mirrors are adopted for all the devices. N_{B} is chosen such that the minimal J_{th} is achieved in each TL. The transparent carrier density N_{tr} is solved by setting g_{p} to zero in Equation 4.8. As compared to the LD, N_{tr} is reduced in SCH TLs due to the base doping. J_{th} is higher in the TL with the same

SQW because of higher α_i. However, by putting more strain or increasing the QW thickness, J_{th} can be made as low as ~73 A/cm^2, which is almost the same as that in the LD. If a 12 nm $In_{0.68}Ga_{0.32}As$ SQW is employed, J_{th} is as low as 42.3 A/cm^2 and $\alpha_m/(\alpha_i + \alpha_m)$ factor is also close to that in the LD. These results indicate that the long wavelength TLs are able to achieve similar DC performances to the LDs by means of structure engineering, proper selection of base doping, and improved design of the QW.

Table 6.1: Summary of the TL and LD performances with different QW designs.

	SCH LD	SCH TL	SCH TL	SCH TL	SCH TL
QW material	8 nm $In_{0.58}Ga_{0.42}As$	8 nm $In_{0.58}Ga_{0.42}As$	8 nm $In_{0.68}Ga_{0.32}As$	12 nm $In_{0.58}Ga_{0.42}As$	12 nm $In_{0.68}Ga_{0.32}As$
N_B ($\times 10^{18}$ cm^{-3})	---	1.5	1.3	1.3	0.9
α_i (cm^{-1})	5	9.6	8.3	8.8	6.1
$\alpha_m/(\alpha_i + \alpha_m)$	75%	61%	64%	63%	71%
N_{tr} ($\times 10^{18}$ cm^{-3})	0.93	0.65	0.64	0.43	0.49
N_{th} ($\times 10^{18}$ cm^{-3})	1.51	2.08	1.75	1.28	1.19
J_{th} (A/cm^2)	73.3	111.6	73.5	72.9	42.3

During the calculation, we have taken a simplified approach to the gain-loss relationship to avoid time-consuming calculations as well as to provide a direct analytical expression about the effects of structural parameters on the lasing condition. In the gain spectrum, the transition broadening due to the interband relaxation process is neglected, which both lowers the peak gain and shifts it to higher energy [145]. The actual hole level in the QW is verified to be lower than N_B (within an error less than 20%), which also leads to an overestimate of the optical gain especially in TLs with thin base or thick QW. In addition, the TL structure needs to be examined and validated from the perspective of an HBT, where metal contact will be made on the base.

Consequently, a thin highly-doped base contact layer is required in the structure and the product of base doping and base thickness has to be large enough to ensure a low sheet resistance. Nevertheless, this is the first theoretical attempt to tackle the TLs that combine both LD and HBT physics. With the improvement in the performances of long wavelength TLs, more complicated and accurate models will be necessary to account for the detailed structural parameters of these novel devices.

To summarize, this chapter presents theoretical investigation and numerical evaluation of InP/InAlGaAs TL structures in terms of the threshold and output characteristics from the perspective of a pure light emitter. The *NpN* TL can be regarded as a SQW inserted into a highly-doped *p*-type layer with an electron density pumping by emitter injection and a hole density fixed at the base doping level. The optical gain is calculated using a simplified *k*-selection model while IVBA is assumed to the main intrinsic optical loss. It is revealed that room-temperature lasing of an *N*-InP/*p*-In($Al_{0.4}Ga_{0.6}$)As/*N*-InP DH TL can be achieved only if the waveguide thickness and base doping level of the TL are within a specific narrow range centered around $d_{\mathrm{WG}} = 35\ \mathrm{nm}$ and $N_{\mathrm{B}} = 4 \times 10^{18}\ \mathrm{cm}^{-3}$. The selectable working range is tremendous expanded by using facet coating or a SCH design, where part of the waveguide is moved into the emitter and collector regions. The SCH TL is shown to have an optimal balance between the threshold current density and optical output characteristics. In addition, the performances of SCH TLs can be improved by employing more compressively-strained or thicker QW as the active region, and the threshold current density can be lowered to sub-100 A/cm^2 level similar to that in a SCH LD.

CHAPTER 7

Research Summary and Future Work

III-V compound semiconductor materials and devices remain as an active and vital research area for system integration and technological innovation for the past 50 years. The band gap engineering, enabled by the advanced growth method such as MBE and MOCVD, brings about improved device performance and novel device functionalities. The invention of light emitting transistor (LET) and transistor laser (TL), for example, bridges the areas of electronic and optoelectronic devices and takes the advantages of both types of devices, which opens up many immediate and potential applications in optoelectronic integrations.

The GaAs-based LETs and TLs have demonstrated high-speed operation and dual functionalities at 980 nm. To extend the wavelength to 1330 and 1550 nm and fit this novel concept into the optical-fiber communication system, InP-based LETs and TLs need to be developed. However, to successfully transfer the TL technology from GaAs to InP, the following issues need to be properly addressed. First is to identify the doping behaviors and material properties of *p*-type InAlGaAs materials that make up of the base layers. In particular, Zn is known to diffuse around in semiconductor matrix while C is not an efficient dopant. Second is to establish a relationship between the device performance and material properties based on the understanding of the device physics. Therefore, it is necessary to bring the knowledge from heterojunction bipolar transistors (HBTs) and light emitting diodes (LEDs) or laser diodes (LDs) together to comprehensively understand the operational principles of these novel devices. In addition, the high intervalence band absorption at long wavelengths gives rise to high optical loss and complicates the TL design compared to the GaAs-based material system.

The development of InAlGaAs/InP LETs and TLs with Zn- and C-doped base layers has been described in this work. By incorporating InGaAs quantum wells (QWs) in the Zn-doped base region of the *N*-InP/*p*-InAlGaAs/*N*-InAlAs HBTs, LET structures were achieved with a current gain of 45 and light emission at a wavelength of 1650 nm. The light output was found to be dependent on the base current. The larger the number of QWs incorporated in the base of the LETs, the larger was the light output, with correspondingly reduced current gain. A MQW gain-guided LD was also grown and fabricated, with a threshold current density of 1.8 kA/cm^2 and emission wavelength of 1545 nm at room temperature. Based on the MQW LET and LD structures, a long wavelength TL was demonstrated for the first time, which operates at 77 K in CW mode with emission wavelength at 1542 nm. Secondary ion mass spectroscopy (SIMS) shows that the *p*-type dopant, Zn, which is commonly used in the growth of InAlGaAs, could diffuse into the emitter and the base active QW region, leading to compromised electrical performance and light output intensity. A detailed study on the effect of growth condition and device structure on Zn diffusion was performed. It was found that three mechanisms that are related to the growth conditions and doping levels of the subcollector, base, and emitter could lead to Zn diffusion. Growth interruption after InP subcollector growth or a relatively low Si doping level during the growth of subcollector, a low growth temperature for the Zn doping of the InAlGaAs base region, and a relatively high Si-doping in the InP emitter layer are regarded as the favorable conditions for the suppression of Zn diffusion. Any deviation from these steps leads to Zn diffusion in certain directions. However, even in the diffusion-suppressed LETs and TLs, Zn will inevitably diffuse into the active region and plague the QW due to the proximity of QW to the highly-doped layers, which certainly results in compromised performances of LETs and TLs.

The LETs and TLs with C-doped base were then investigated due to the low dopant diffusivity. By lowering the growth temperature and V/III ratio during C doping, hole concentration as high as 3×10^{19} cm^{-3} has been achieved. However, the *N*-InP/*p*-$In_{0.52}(Al_{0.4}Ga_{0.6})_{0.48}As$/*N*-$In_{0.52}Al_{0.48}As$ HBT and LET show current gains of only 12 and 0.22, respective, which are much lower than those in the corresponding Zn-doped devices. As a dual-functional device, Zn-doped LET works like an HBT with a current gain of 45 and C-doped LET functions like an LED with a carrier capture efficiency of 82%. A charge control model was developed for LETs taking into account the quantum capture of the unbounded minority carries into the bounded QW states. The distinctive device performance of Zn- and C-doped LETs was found to originate from the different quantum capture efficiency and carrier lifetime in the quantum well due to different base doping levels.

A C-doped *N*-InP/*p*-$In_{0.52}(Al_{0.4}Ga_{0.6})_{0.48}As$/*N*-InP double heterostructure SQW TL was fabricated and it demonstrates CW operation at 77 K with a threshold current of I_B=35 mA. By comparing the optical output characteristics of the TL and a laser diode with similar structure, it is concluded that the low differential quantum efficiency and the high threshold current density in the TL is related the strong intervalence band absorption in the highly-doped base layer. For a better TL design, we present theoretical analysis and numerical calculation on the threshold condition of an InAlGaAs/InP TL using a rather simple yet effective approach. Based on the steady state condition that gain is balanced by loss, the base doping level and thickness are numerically investigated through evaluating the threshold carrier and current densities, which reveals only a narrow working range of supporting lasing. We show that by using a more compressively-strained or thicker quantum well as the active region in a separate confinement heterostructure TL, it is possible to obtain a threshold current density as low as sub-100 A/cm^2 at

room temperature. These structures need to be examined in practice to verify the validity of the analysis and calculation.

Due to the use of CBr_4, the C doping in quaternary InAlGaAs suffers from a poor within-wafer uniformity and run-to-run reproducibility. In view of these drawbacks, novel growth method and technique such as atomic layer epitaxy (ALE) and strain-balanced InAs/(Al)GaAs superlattices (SLs) have been proposed for *p*-type doping. However, no *p*-type conductivity in In(Al)GaAs layers has been achieved. In ALE by intrinsic doping, although excellent structural and optical quality achieved in In(Al)GaAs layers, the concentration of Ga-C_{As} bonds is not high enough to counteract the As-C_{In} bonds. In InAs/(Al)GaAs SLs, separate doping in InAs and GaAs is possible; however, the thin thickness of GaAs layer limited by the wetting layer thickness of InAs on InP can't compensate the *n*-type background level. Future work for *p*-type doping could still include CBr_4 as the external dopant, but in a more controllable way. For instance, using InGaAs:C/InAlAs:C SLs could possibly solve the reproducibility and uniformity issue by avoiding the quaternary alloys. Using Al-free InGaAs:C/InP SLs could improve the structural quality and surface morphology and lead to longer carrier lifetime. In addition, tensile-strained $In_xGa_{1-x}As$:C such as $In_{0.4}Ga_{0.6}As$:C could be a better base layer material [89], which enjoys a larger bandgap (0.89 eV) than $In_{0.58}Ga_{0.42}As$ QW (0.7 eV) as well as a higher hole concentration due to higher Ga mole fraction. In this case, Al-free base/active region can be made by simply tuning the In compositions, which greatly reduces the complexities associated with the base growth. Optimization of the TL structure and base doping level using $In_{0.4}Ga_{0.6}As$ base is necessary.

REFERENCES

[1] S. Wu, *Compound Semiconductor Materials: Technology, Development and Market Trends,* (BBC Research, 2005).

[2] M. Feng, N. Holonyak, Jr., and W. Hafez, Appl. Phys. Lett. 84, 151 (2004).

[3] J. Bardeen and W. H. Brattain, Phys. Rev. 74, 230 (1948).

[4] N. Holonyak, Jr. and S. F. Bevacqua, Appl. Phys. Lett. 1, 82 (1962).

[5] P. Bhattacharya, *Semiconductor optoelectronic devices*, 2nd Ed. (Prentice Hall, New Jersey, 1997).

[6] W. Liu, *Fundamentals of III-V devices: HBTs, MESFETs, and HEMTs* (Wiley, New York, 1999).

[7] W. Hafez, W. Snodgrass, and M. Feng, Appl. Phys. Lett. 87, 252109 (2005).

[8] M. Feng, N. Holonyak, Jr., H. W. Then, and G. Walter, Appl. Phys. Lett. 91, 053501 (2007).

[9] J. Genoe, C. Van Hoof, K. Fobelets, R. Mertens, and G. Borghs, Appl. Phys. Lett. 61, 1051 (1992).

[10] M, Mastrapasqua, S. Luryi, F. Capasso, A. L. Hutchinson, D. L. Sivco, and A. Y. Cho, IEEE Trans. Electron Devices 40, 250 (1993).

[11] V. L. Tolstikhin, and M. Mastrapasqua, Appl. Phys. Lett. 67, 3868 (1995).

[12] C.-X. Du, F. Duteil, G. V. Hansson, and W.-X. Ni, Appl. Phys. Lett. 78, 1697 (2001).

[13] B. Park and H. Takezoe, Appl. Phys. Lett. 85, 1280 (2004).

[14] K. Nakamura, T. Hata, A. Yoshizawa, K. Obata, H. Endo, and K. Kudo, Appl. Phys. Lett. 89, 103525 (2006).

[15] E. B. Namdas, P. Ledochowitsch, J. D. Yuen, D. Moses, and A. J. Heeger, Appl. Phys. Lett. 92, 183304 (2008).

[16] M. Feng, N. Holonyak, Jr., and R. Chan, Appl. Phys. Lett. 84, 1952 (2004).

[17] G. Walter, N. Holonyak, Jr., M. Feng, and R. Chan, Appl. Phys. Lett. 85, 4768 (2004).

[18] R. Chan, M. Feng, N. Holonyak, Jr., and G. Walter, Appl. Phys. Lett. 86, 131114 (2005).

[19] M. Feng, N. Holonyak, Jr., G. Walter, and R. Chan, Appl. Phys. Lett. 87, 131103 (2005).

[20] F. Dixon, M. Feng, and N. Holonyak, Jr., Appl. Phys. Lett. 96, 241103 (2010).

[21] M. Feng, N. Holonyak, Jr., A. James, K. Cimino, G. Walter, and R. Chan, Appl. Phys. Lett. 89, 113504 (2006).

[22] H. W. Then, G. Walter, M. Feng, and N. Holonyak, Jr., Appl. Phys. Lett. 93, 163504 (2008).

[23] F. Dixon, R. Chan, G. Walter, N. Holonyak, Jr., M. Feng, X. B. Zhang, J. H. Ryou, and R. D. Dupuis, Appl. Phys. Lett. 88, 012108 (2006).

[24] B. F. Chu-Kung, M. Feng, G. Walter, N. Holonyak, Jr., T. Chung, J.-H. Ryou, J. Limb, D. Yoo, S.-C. Shen, R. D. Dupuis, D. Keogh, and P. M. Asbeck, Appl. Phys. Lett. 89, 082108 (2006).

[25] Y. Huang, X. B. Zhang, J.-H. Ryou, R. D. Dupuis, F. Dixon, N. Holonyak, Jr., and M. Feng, J. Appl. Phys. 103, 114505 (2008).

[26] H. W. Then, M. Feng, and N. Holonyak, Jr., Appl. Phys. Lett. 94, 013509 (2009).

[27] R. Chan, M. Feng, N. Holonyak, Jr., A. James, and G. Walter, Appl. Phys. Lett. 88, 143508 (2006).

[28] G. Walter, A. James, N. Holonyak, Jr., M. Feng, and R. Chan, Appl. Phys. Lett. 88, 232105 (2006).

[29] A. James, G. Walter, M. Feng, and N. Holonyak, Jr., Appl. Phys. Lett. 90, 152109 (2007).

[30] M. Feng, N. Holonyak, Jr., H. W. Then, C. H. Wu, and G. Walter, Appl. Phys. Lett. 94, 041118 (2009).

[31] H. W. Then, C. H. Wu, G. Walter, M. Feng, and N. Holonyak, Jr., Appl. Phys. Lett. 94, 101114 (2009).

[32] H. W. Then, M. Feng, and N. Holonyak, Jr., Appl. Phys. Lett. 91, 183505 (2007).

[33] B. Faraji, D. L. Pulfrey, and L. Chrostowski, Appl. Phys. Lett. 93, 103509 (2008).

[34] B. Faraji, W. Shi, D. L. Pulfrey, and L. Chrostowski, Appl. Phys. Lett. 93, 143503 (2008).

[35] C. H. Wu, G. Walter, H. W. Then, M. Feng, and N. Holonyak, Jr., Appl. Phys. Lett. 94, 171101 (2009).

[36] G. Walter, C. H. Wu, H. W. Then, M. Feng, and N. Holonyak, Jr., Appl. Phys. Lett. 94, 241101 (2009).

[37] C. H. Chen, M. Hargis, J. M. Woodall, M. R. Melloch, J. S. Reynolds, E. Yablonovitch, and W. Wang, Appl. Phys. Lett. 74, 3140 (1999).

[38] L. Zhang and J. P. Leburton, IEEE J. Quantum Electron. 45, 359 (2009).

[39] M. Feng, H. W. Then, N. Holonyak, Jr., G. Walter, and A. James, Appl. Phys. Lett. 95, 033509 (2009).

[40] M. Feng, N. Holonyak, Jr., R. Chan, A. James, and G. Walter, Appl. Phys. Lett. 88, 063509 (2006).

[41] S. Chandrasekhar, Solid State Electron. 41, 1413 (1997).

[42] M. Asada, A. Kameyama, and Y. Suematsu, IEEE J. Quantum Electron. QE-20, 745 (1984).

[43] J. Taylor and V. Tolstikhin, J. Appl. Phys., 87, 1054 (2000).

[44] Y. Huang, J.-H. Ryou, and R. D. Dupuis, J. Cryst. Growth 310, 4345 (2008).

[45] Y. Huang, J.-H. Ryou, R. D. Dupuis, F. Dixon, N. Holonyak, Jr., and M. Feng, "InP/InAlGaAs light-emitting transistors and transistor lasers with a carbon-doped base layer," submitted to J. Appl. Phys.

[46] I. Vurgaftman and J. R. Meyer, J. Appl. Phys. 89, 5815 (2001).

[47] W. C. Liu, H. J. Pan, S. Y. Cheng, W. C. Wang, J. Y, Chen, S. C. Feng, and K. H. Yu, Appl. Phys. Lett. 75, 572 (1999).

[48] Y. F. Chen, Y. T. Dai, J. C. Fan, T. L. Lee, and H. H. Lin, Appl. Phys. Lett. 67, 1256 (1995).

[49] M. J. Mondry, D. I. Babic, J. E. Bowers, and L. A. Coldren, IEEE Photon. Technol. Lett. 4, 627 (1992).

[50] H. M. Manasevit, Appl. Phys. Lett. 12, 156 (1968).

[51] R. D. Dupuis and P. D. Dapkus, Appl. Phys. Lett. 31, 466 (1977).

[52] Dongwon Yoo, "*Growth and Characterization of III-Nitride Material System for Photonic and Electronic Devices by Metalorganic Chemical Vapor Deposition*," Doctoral Dissertation, Georgia Institute of Technology (2007).

[53] B. D. Cullity and S. R. Stock, *Elements of X-Ray Diffraction,* 3rd Ed., (Prentice Hall, New Jersey, 2001).

[54] S. Pereira, M. R. Correia, E. Pereira, K. P. O'Donnell, E. Alves, A. D. Sequeira, N. Franco, I. M. Watson and C. J. Deatcher, Appl. Phys. Lett. 80, 3913 (2002).

[55] Precursors are provide by SAFC Hitech (formerly Epichem), Haverhill, MA.

[56] M. Shinohara, and N. Inoue, Appl. Phys. Lett. 66 (1995) 1936.

[57] H. Dumont, Y. Monteil, and J. Bouix, Appl. Surf. Sci. 161 (2000) 286.

[58] R. J. Young, L. O. Mereni, N. Petkov, G. R. Knight, V. Dimastrodonato, P. K. Hurley, G. Hughes, and E. Pelucchi, J. Cryst. Growth 312 (2010) 1546.

[59] Transverse optical confinement factor is calculated by "WaveGuide", designed by Photodigm Inc. The refractive indices are from Ref. 49.

[60] The band diagram is calculated by the free program "1D-Poisson".

[61] F. Dixon, M. Feng, N. Holonyak, Jr., Yong Huang, X. B. Zhang, J. H. Ryou, and R. D. Dupuis, Appl. Phys. Lett. 93, 021111 (2008).

[62] N. Otsuka, M. Ishino, and Y. Matsui, J. Appl. Phys. 80, 1405 (1996).

[63] N. Otsuka, M. Kito, M. Ishino, Y. Matsui, and F. Toujou, J. Appl. Phys. 84, 4239 (1998).

[64] K. Kadoiwa, K. Ono, and Y. Ohkura, J. Crystal Growth 297, 44 (2006).

[65] D. G. Deppe, Appl. Phys. Lett. 56, 370 (1990).

[66] A. J. Howard, B. Pathangey, Y. Hayakawa, T. J. Anderson, C. Blaauw, and A. J. SpringThorpe, Semicond. Sci. Technol. 18, 723 (2003).

[67] D. Wittorf, A. Rucki, W. Jager, R. H. Dixon, K. Urban, H. -G. Hettwer, N. A. Stolwijk, and H. Mehrer, J. Appl. Phys. 77, 2843 (1995).

[68] K. Kurishima, T. Kobayashi, H. Ito, and U. Gosele, J. Appl. Phys. 79, 4017 (1996).

[69] V. Swaminathan, N. Chand, M. Geva, P. J. Anthony, and A. S. Jordan, J. Appl. Phys. 72, 4648 (1992).

[70] V. Swaminathan, C. L. Reynolds Jr., and M. Geva, Appl. Phys. Lett. 66, 2685 (1995).

[71] T. Kobayashi, K. Kurishima, and U. Gosele, Appl. Phys. Lett. 62, 284 (1993).

[72] K. Kurishima, H. Nakajima, S. Yamahata, T. Kobayashi, and Y. Matsuoka, Appl. Phys. Lett. 64, 1111 (1994).

[73] S. M. Sze, *Modern semiconductor device physics* (Wiley, New York, 1998).

[74] R. Bhat, M. A. Koza, J.-I. Song, S. A. Schwarz, C. Caneau, and W.-P. Hong, Appl. Phys. Lett. 65, 338 (1994).

[75] T. Sasaki, H. Yamada, S. Takano, M. Kitamura, I. Mito, T. Suzuki, and H. Hoshino, J. Crystal Growth 93, 838 (1988).

[76] N. Kobayashi, T. Makimoto, and Y. Horikoshi, Appl. Phys. Lett. 50, 1435 (1987).

[77] S. A. Stockman, G. E. Höfler, J. N. Baillargeon, K. C. Hsieh, K. Y. Cheng, and G. E. Stillman, J. Appl. Phys. 72, 981 (1992).

[78] S. A. Stockman, A. W, Hanson, and G. E. Stillman, App. Phys. Lett. 60, 2903 (1992).

[79] T. F. Kuech and J. M. Redwing, J. Crystal Growth 145, 382 (1994).

[80] H. Ito and T. Ishibashi, Jpn. J. Appl. Phys. 30, L944 (1991).

[81] N. I. Buchan, T. F. Kuech, G. Scilla, and F. Cardone, J. Crystal Growth 110, 405 (1991).

[82] T. B. Joyce, T. J. Bullough, and T. Farrell, Appl. Phys. Lett. 65, 2193 (1994).

[83] K. Tateno, Y. Kohama, and C. Amono, J. Crystal Growth 172, 5 (1997).

[84] H. Ito, K. Kurishima, and N. Watanabe, J. Crystal Growth 158, 430 (1996).

[85] J. Décobert, N. Lagay, and B. Thevenard, J. Crystal Growth 310, 4813 (2008).

[86] L. Calderon, Y. Lu, H. Shen, J. Pamulapati, M. Dutta, W. H. Chang, L. W. Yang, and P. D. Wright, Appl. Phys. Lett. 60, 1597 (1992).

[87] D. Keiper, B. Sermage, and J-L, Benchimol, Jpn. J. Appl. Phys. 40, L137 (2001).

[88] D. Cui, S. Hubbard, D. Pavlidis, A. Eisenbach, and C. Chelli, Semicond. Sci. Technol. 17, 503 (2002).

[89] J. L. Benchimol, J. Mba, B. Sermage, M. Riet, S. Blayac, P. Berdaguer, A. M. Duchenois, P. André, J. Thuret, C. Gonzalez, A. Konczykowska, J. Crystal Growth 209, 476 (2000).

[90] F. Brunner, T. Bergunde, E. Richter, P. Kurpas, M. Achouche, A. Maaβdorf, J. Würfl, and M. Weyers, J. Crystal Growth 221, 53 (2000).

[91] W. Y. Hwang, and D. L. Miller, J. Vac. Sci. Technol. B. 13, 667 (1995).

[92] Q. Yang, D. S. Scott, T. Chung, and G. E. Stillman, Appl. Phys. Lett. 77, 271 (2000).

[93] H. C. Kuo, D. Ahmari, B. G. Moser, J. Mu, M. Hattendorf, D. Scott, R. Meyer, M. Feng, and G. E. Stillman, J. Vac. Sci. Technol. B. 17, 1185 (1999).

[94] N. Tessler and G. Eisenstein, IEEE J. Quantum Electron. 29, 1586 (1993).

[95] R. Olshansky, C. B. Su, J. Manning, and W. Powazinik, IEEE J. Quantum Electron. QE-20, 838 (1984).

[96] J. Piprek, J. K. White, and A. J. SpringThorpe, IEEE J. Quantum Electron. 38, 1253 (2002).

[97] A. Kasukawa, R. Bhat, C. E. Zah, M. A. Koza, and T. P. Lee, Appl. Phys. Lett. 59, 2486 (1991).

[98] M. Ozeki, Mater. Sci. Rep. 8, 97 (1992).

[99] M. A. Tischler and S. M. Bedair, Appl. Phys. Lett. 48, 1681 (1986).

[100] Y. Horikoshi, M. Kawashima, and H. Yamaguchi, Jpn. J. Appl. Phys. 27, 169 (1988).

[101] J.-I. Nishizawa, H. Abe, and T. Kurabayashi, J. Electrochem. Soc. 132, 1197 (1985).

[102] M. A. Tischler, N. G. Anderson, and S. M. Bedair, Appl. Phys. Lett. 49 (1986) 1199.

[103] M. Sato and Y. Horikoshi, Appl. Phys. Lett. 52, 123 (1988).

[104] K. Mukai, N. Ohtsuka, and M. Sugawara, Appl. Phys. Lett. 70, 2416 (1997).

[105] Y. M. Park, Y. J. Park, K. M. Kim, J. C. Shin, J. D. Song, J. I. Lee, and K. H. Yoo, J. Appl. Phys. 95, 123 (2004).

[106] H, Tian, K. W. Kim, M. A. Littlejohn, S. M. Bedair, and L. C. Witkowski, IEEE Trans. Electron Device. 39, 1998 (1992).

[107] J. R. Gong, D. Jung, N. A. El-Masry, and S. M. Bedair, Appl. Phys. Lett. 57, 400 (1990).

[108] W. G. Jeong, E. P. Menu, and P. D. Dapkus, Appl. Phys. Lett. 55, 244 (1989).

[109] W. K. Chen, J. C. Chen, L. Anthony, and P. L. Liu, Appl. Phys. Lett. 55, 987 (1989).

[110] M. A. Khan, R. A. Skogman, D. T. Olson, J. M. van Hove, and J. N. Kuznia, Appl. Phys. Lett. 60, 1366 (1992).

[111] N. H. Karam, T. Parodos, P. Colter, D. McNulty, W. Rowland, J. Schetzina, N. El-Masry, and S. M. Bedair, Appl. Phys. Lett. 67, 94 (1995).

[112] M. Takeuchi, H. Shimizu, R. Kajitani, K. Kawasaki, T. Kinoshita, K. Takada, H. Murakami, Y. Kumagai, A. Koukitu, T. Koyama, S. F. Chichibu, Y. Aoyagi, J. Crystal Growth 305, 360 (2007).

[113] H. J. Kim, S. Choi, D. Yoo, J.-H. Ryou, and R. D. Dupuis, Appl. Phys. Lett. 93, 022103 (2008).

[114] S. P. DenBaars and P. D. Dapkus, J. Crystal Growth 98, 195 (1989).

[115] N. Kobayashi, Y. Kobayashi, Y. Yamauchi, and Y. Horikoshi, Appl. Surf. Sci. 60/61, 544 (1992).

[116] K. Mochizuki, M. Ozeki, K. Kodama, and N. Ohtsuka, J. Crystal Growth 93, 557 (1988).

[117] N. Kobayashi and T. Makimoto, Appl. Surf. Sci. 82/83, 284 (1994).

[118] K. G. Beid, H. M. Urdianyk, and S. M. Bedair, Appl. Phys. Lett. 59, 2397 (1991).

[119] P. D. Dapkus, B. Y. Maa, Q. Chen, W. G. Jeong, and S. P. DenBaars, J. Crystal Growth 107, 73 (1991).

[120] H. J. Kim, S. Choi, D. Yoo, J.-H. Ryou, and R. D. Dupuis, J. Crystal Growth 310, 4880 (2008).

[121] Y. Sakuma, M. Ozeki, K. Kodama, and N. Ohtsuka, J. Crystal Growth 114, 31 (1991).

[122] M. Ozeki, T. Haraguchi, T. Takeuchi, K. Maeda, J. Crystal Growth 276, 374 (2005).

[123] Matthews and Blakeslee, J. Crystal Growth 27, 118 (1974).

[124] H. Ohno, S. Ohtsuka, A. Ohuchi, T. Matsubara, and H. Hasegawa, J. Crystal Growth 93, 342 (1988).

[125] G. B. Stringfellow, *Organometallic Vapor-Phase Epitaxy: Theory and Practice*, 2nd Ed., (Academic Press, New York, 1999).

[126] K. G. Reid, A. F. Myers, J. Ramdani, N. A. El-Masry, and S. M. Bedair, SPIE, 1676, 139 (1992).

[127] J.-R. Ro, S.-J. Park, S.-B., Kim, and E.-H. Lee, J. Crystal Growth 164, 377 (1996).

[128] C. R. Abernathy, S. J. Pearton, F. Ren, W. S. Hobson, T. R. Fullowan, A. Katz, A .S. Jordan, and J. Kovalchick, J. Crystal Growth 105, 375 (1990).

[129] E. Tokumitsu, J. Shirakashi, M. Qi, T. Yamada, S. Nozaki, M. Konagai, and K. Takahashi, J. Crystal Growth 120, 301 (1992).

[130] C. R. Abernathy, P. W. Wisk, S. J. Pearton, W. S. Hobson, P. H. Fuoss, F. J. Lamelas, S. N. G. Chu, and F. Ren, Appl. Phys. Lett. 60, 1339 (1992).

[131] E. F. Schubert and R. F. Kopf, J. Crystal Growth 127, 1037 (1993).

[132] N. Pan, J. Elliott, H. Hendriks, D. Lee, and M. Welch, J. Appl. Phys. 79, 504 (1996).

[133] M. Pristovsek, B. Han, J.-T. Zettler, W. Richter, J. Crystal Growth 221, 149 (2000).

[134] J. V. Deelen, G. J. Bauhuis, J. J. Schermer, P. K. Larsen, J. Crystal Growth 271, 367 (2004).

[135] M. C. Tamargo, R. Hull, L. H. Greene, J. R. Hayes, and A. Y. Cho, Appl. Phys. Lett. 46, 569 (1985).

[136] T. C. Hasenberg, D. S. McCallum, X. R. Huang, M. D. Dawson, T. F. Boggess, and A. L. Smirl, Appl. Phys. Lett. 58, 937 (1991).

[137] N. S. Kumar, J. I. Chyi, C. K. Peng, and H. Morkoc, Appl. Phys. Lett. 55, 775 (1989).

[138] L. Goldstein, F. Glas, J. Y. Marzin, M. N. Charasse, and G. Le Roux, Appl. Phys. Lett. 47, 1099 (1985).

[139] A. Lindner, Q. Liu, F. Scheffer, M. Haase, W. Prost, F. J. Tegude, J. Crystal Growth 145, 771 (1994).

[140] C. W. Snyder, B. G. Orr, D. Kessler, and L. M. Sander, Phys. Rev. Lett. 66, 3032 (19991).

[141] J. F. Carlin, R. Houdré, A. Rudra, and M. Ilegems, Appl. Phys. Lett. 59, 3018 (1991).

[142] W. Seifert, K. Deppert, J. O. Fornell, X. Liu, S. Nilsson, M. E. Pistol, and L. Samuelson, J. Crystal Growth 124, 531 (1992).

[143] M. Friedrich and H.-M. Rein, IEEE Trans. Electron Devices 46, 1384 (1999).

[144] S. L. Chuang, *Physics of Optoelectronic Devices*. (Wiley, New York, 1995).

[145] T. Makino, IEEE J. Quantum Electron. 32, 493 (1996).

[146] K. J. Vahala and C. E. Zah, Appl. Phys. Lett. 52, 1945 (1988).

[147] T. Ishikawa and J. E. Bowers, IEEE J. Quantum Electron 30, 562 (1994).

[148] R. J. Deri and E. Kapon, IEEE J. Quantum Electron. 27, 626 (1991).

[149] R. Driad, W. R. McKinnon, S. P. McAlister, T. Garanzotis, and A. J. SpringThorpe, Semicond. Sci. Technol. 16, 171 (2001).

[150] B. Saint-Cricq, F. Lozes-Dupuy, and G. Vassilieff, IEEE J. Quantum Electron. QE-22, 625 (1986).